The Effect of a Fisk-Parker Hybrid Magnetic Field on Cosmic Rays in the Heliosphere

Tjaart P. J. Krüger, B.Sc.

Dissertation accepted for the degree Master of Science in Physics
at the North-West University

Supervisor: Prof. R. A. Burger
Assistant supervisor: Dr. M. Hitge

December 2005
Potchefstroom Campus

Abstract

The existence of a Fisk-type heliospheric magnetic field (HMF) is one of the most debated questions in cosmic-ray modulation. Recently, *Burger and Hitge* [2004] developed a divergence-free Fisk-Parker hybrid magnetic field model to demonstrate the behaviour of cosmic rays in the heliosphere due to such a field. This approach has been refined and the properties of the consequent field are investigated. It is found that randomly directed magnetic field diffusion in and above the photosphere significantly influences the solar magnetic field both at the solar poles and near the polar coronal hole boundary. The solar cycle dependence of this field is investigated, a study which is of particular importance for studies of the long-term behaviour of cosmic rays, such as those undertaken at the SANAE base in Antarctica. The amplitudes of the 26-day recurrent cosmic-ray variations are modelled as function of both latitudinal gradient and heliolatitude and are found to agree qualitatively and in some cases quantitatively with the observational results reported by *Zhang* [1997] and *Paizis et al.* [1999]. Although magnetic field data do not clearly indicate the existence of the Fisk field [see, e.g., *Forsyth et al.*, 2002], this study supports the existence of a Fisk-type HMF.

Keywords: `Fisk-type heliospheric magnetic field, cosmic rays,`
`modulation, recurrent cosmic-ray variations`

Opsomming

Die Effek van 'n Fisk-Parker-Hibriedmagneetveld op Kosmiese Strale in die Heliosfeer

Die bestaan van 'n Fisk-tipe heliosferiese magneetveld (HMV) is een van die mees debatteerbare onderwerpe in modulasiestudies van kosmiese strale. 'n Divergensievrye Fisk-Parker-hibriedmagneetveld is onlangs deur *Burger en Hitge* [2004] ontwikkel om die gedrag van kosmiese strale in die heliosfeer te demonstreer. Hierdie benadering is nou verfyn en die eienskappe van die gevolglike veld word ondersoek. Dit word bevind dat die son se magneetveld beduidend deur willekeuriggerigte magneetvelddiffusie in en bo die fotosfeer by die son se pole en naby poolkoronagatgrense beïnvloed word. 'n Studie van hierdie veld se sonsiklusafhanklikheid, soos dit in hierdie werk ondersoek word, is van besondere belang om die langtermyngedrag van kosmiese strale te bestudeer, 'n studie wat by die SANAE-basis in Antarktika onderneem word. Die amplitudes van die 26-dag variasies in die intensiteit van kosmiese strale word as funksie van beide die breedtegraadsgradiënt en heliobreedtegraad gemodelleer, en toon kwalitatiewe en in sommige gevalle kwantitatiewe ooreenstemming met die waargenome resultate van *Zhang* [1997] en *Paizis et al.* [1999]. Alhoewel magneetvelddata die bestaan van die Fisk-veld nie duidelik identifiseer nie [sien bv. *Forsyth et al.*, 2002], ondersteun hierdie studie wel die bestaan van 'n Fisk-tipe HMV.

Sleutelwoorde: `Fisk-tipe heliosferiese magneetveld, kosmiese strale, modulasie, terugkerende kosmiesestraalvariasies`

Nomenclature

Listed are the acronyms used in the text. For the purpose of clarity, the acronym is written out in full when it appears for the first time in the text or wherever relevant.

AU	astronomical unit
CR	cosmic ray
CIR	co-rotating interaction region
CH	coronal hole
CME	coronal mass ejection
CMF	coronal magnetic field
FLS	fast latitude scan
HCS	heliospheric current sheet
HMF	heliospheric magnetic field
MHD	magnetohydrodynamic
NS	neutral sheet
PCH	polar coronal hole
PFSS	potential-free source surface
SS	source surface
TPE	transport equation

Contents

Chapter 1

Introduction

Life on earth depends completely on the presence and properties of its sole source of light and energy, the sun. On the terrestrial surface, the solar conditions are observed to be fairly steady. However, outside the protection of the earth's atmosphere and magnetosphere, man is exposed to the strong interaction between the dynamic solar magnetic field, solar plasma and other highly energetic particles. In this introductory chapter, some properties of this magnetic field and the influence region of the sun are described, and an outline of the dissertation is given.

The convecting ionised particles inside the sun generate the solar magnetic field. The interaction between the plasma and magnetic field in the solar interior results in a field which oscillates with a period of about 22 years, probably by means of the plasma dynamo effect. Strands of field lines continually pierce through the solar surface, resulting in a dynamic network of open and closed field lines, leading to many interesting phenomena on and above the solar surface. A large fraction of the solar field lines extends to large radial distances above the solar surface and are captured by the continually radially outflowing plasmatic atmosphere, known as the solar wind, to become open field lines. These open lines fill the whole heliosphere, i.e. the influence region of the sun, and the consequent magnetic field is called the heliospheric magnetic field (HMF).

The first successful model of the HMF was proposed by *Parker* [1958]. This field structure is described by an Archimedian spiral, where the field lines remain on cones of constant heliographic latitudes. Energetic particles that enter the heliosphere, known as cosmic rays (CRs), as well as solar particles, propagate relatively easily along the magnetic field lines. The low-latitude particles that are accelerated at shocks near the sun are therefore expected to remain mostly near the same latitudes. Such particles are known to exhibit characteristic 26-day periodic intensity variations. However, observational results surprisingly indicate that a significant number of such recurrent variations occur up to the highest latitudes [see, e.g. *Roelof et al.*, 1997]. One viewpoint advocates that particles may propagate easier latitudinally across field lines than what the standard Parker field suggests [*Kóta and Jokipii*, 1995]. Another solution is to deduce a new HMF model from the magnetic field properties on and above the solar surface, leading to a field structure with lines that exhibit large latitudinal variations along which the energetic particles can propagate [*Fisk*, 1996]. Such a field originates at high latitudes on the solar surface, inside large, quasi-steady, open magnetic structures, called polar coronal holes (PCHs).

Burger and Hitge [2004] modified the HMF model of *Fisk* [1996] into a Fisk-Parker hybrid field model in order to implement it in the three-dimensional numerical modulation code of *Hattingh* [1998]. The purpose of the dissertation is to test for the existence of such a Fisk-type field. This is attained by examining the properties and attributes of Fisk-type fields, refining the Fisk-Parker hybrid field model and by investigating its global and local effect on CRs in the heliosphere. Since not everybody believes in the existence of Fisk-type fields, this study should give a clearer answer to one of the most debated questions in cosmic-ray modulation.

In Chapter 2, the relevant background about the physical processes that result in and influence Fisk-type fields is given. The chapter first describes the inner regions of the sun, then progresses to the magnetic field properties on the solar surface and eventually discusses its relevant behaviour in the solar atmosphere in connection with the solar wind.

The structure and properties of the HMF, the field above the solar atmosphere, are discussed in Chapter 3. The significance of diffusion in the coronal magnetic field (CMF), which largely determines the presence of Fisk-type fields, is introduced and different HMF models are discussed.

An extensive study of the HMF model of *Fisk* [1996] is presented in Chapter 4. The footpoint motions on the solar wind source surface are described and the resulting footpoint velocities, which lead to the expression for the Fisk field, are discussed and illustrated. The basic assumptions in the Fisk model are discussed in detail, as well as the significance of the proposed boundary conditions. The Fisk-Parker hybrid model of *Burger and Hitge* [2004] is also introduced.

Chapter 5 refines the hybrid model by adding physical significance to its assumptions and extending the solar activity period over which the hybrid field remains valid. The simulated behaviour of CRs in the heliosphere, due to this refined hybrid model, is investigated in Chapter 6 in order to test for the existence of such a field in an indirect way. The numerical modulation model of *Hattingh* [1998], which is used to attain this purpose, is first described. This model uses the steady-state, three-dimensional version of Parker's transport equation to describe the behaviour of CRs due to all magnetic field and solar wind processes in the heliosphere. In Chapter 8, a summary and conclusions of the main results are given.

The research from this dissertation has been presented at two national conferences: the Conference of the South African Institute for Physics (SAIP) in July 2005 in Pretoria, and the Afrikaans student symposium presented by the South African Academy for Natural Sciences in October 2005 in Pretoria. The work will also be presented at the AGU Fall Meeting in December 2005 in San Francisco, USA (Abstract SH23B-0341).

Chapter 2

The Sun: Structure and Properties

2.1 Introduction

This chapter introduces some basic concepts in the field of solar physics that are essential background for the following chapters. Information given in this chapter will either be used as constraints or physical necessities for the hybrid heliospheric magnetic field discussed in Chapter 5.

Firstly, the motion of the inner regions of the sun is described. Such motion is responsible for generating the solar magnetic field by means of the plasma dynamo effect. The structure and properties of this field, that give rise to many dynamical processes on and above the solar surface, are briefly described. Solar plasma follows the field lines and eventually accelerates to form the solar wind. Finally, the origin and properties of this phenomenon are described.

2.2 Basic Structure of the Sun

At the centre of our solar system is a large sphere of active plasma with a mass of $\sim 2 \times 10^{30}$ kg, consisting of about 74% hydrogen, 25% helium and traces of heavier elements. The sun is classified as a G2V main sequence star and has a radius $r_\odot$ of approximately 6.96×10^5 km.

The interior structure of the sun is illustrated in Figure 2.1. Thermonuclear energy is generated in the core and transported through the radiative region by means of gamma-ray diffusion.

In the convection zone, parcels of plasma, known as granules or convection cells, rise from the hotter inner regions to the solar surface by means of convection and buoyancy, similar to the gas bubbles in a boiling fluid. This process is called granulation. The solar surface, called the photosphere, represents the top layer of granules, having characteristic sizes of 500 – 1000 km. These granules release energy into the solar atmosphere, which causes the granules to become cooler and denser, and sink again after a few minutes. The granules are continuously pushed aside by newly emerging ones and move around due to convection streams. These effects result in a highly dynamic photosphere on relatively small scales. The photosphere

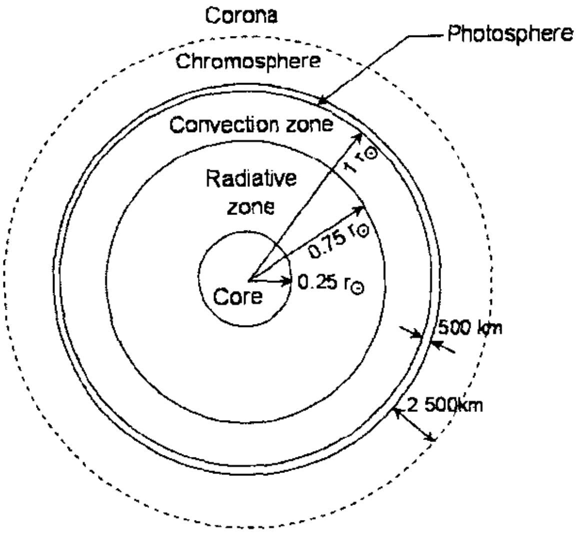

Figure 2.1: A two-dimensional schematic of the solar interior and atmosphere (not drawn to scale).

also consists of much larger and steadier granules, called supergranules, with typical sizes of $\sim$ 30 000 km and lifetimes of $\sim$ 1 - 2 days. These supergranules seem to rotate faster than the underlying photosphere, an illusion generated by waves on the photosphere that propagate in the direction of solar rotation [*Gizon et al.*, 2003]. The origin of this feature as well as that of supergranules is still unclear.

The layer in the solar atmosphere directly above the photosphere is known as the chromosphere. Its name is derived from the Greek word $\chi\rho o\mu o\varsigma$ (chromos), meaning colour, originating from the strong, red Hα (656.3 nm) emission in this region. Large amounts of solar plasma escape periodically and ubiquitously from the photosphere in the form of dynamic jets, called spicules. At any instant $\sim 10^5$ spicules are present in the chromosphere [*De Pontieu et al.*, 2004].

The halo of tenuous gas surrounding the chromosphere denotes the outer atmosphere and is called the corona. Due to the large negative pressure gradient between the solar corona and interplanetary space at larger radial distances, the particles in the corona must constantly be accelerated radially outward, reaching a supersonic flow speed in order to maintain dynamic equilibrium [*Parker*, 1958]. This outflow is known as the solar wind. The solar wind pressure decreases with radial distance from the sun until it corresponds to the pressure of the interstellar medium. The outer boundary where the solar wind merges with the interstellar matter is called the heliopause. The volume filled by the solar wind plasma from the sun to this outer boundary is known as the heliosphere. This region of space denotes the influence region of the sun. A schematic illustration of the expected structure of the heliosphere is shown in Figure 2.2 [*Jokipii*, 1989]. When the solar wind pressure is low enough with respect to the pressure of the interstellar medium, the wind makes a sudden transition from a supersonic to a subsonic flow speed, creating a shock known as the termination shock. On 16 December 2004, Voyager 1 became the first spacecraft to cross the termination shock at a radial distance of 94.01 AU from

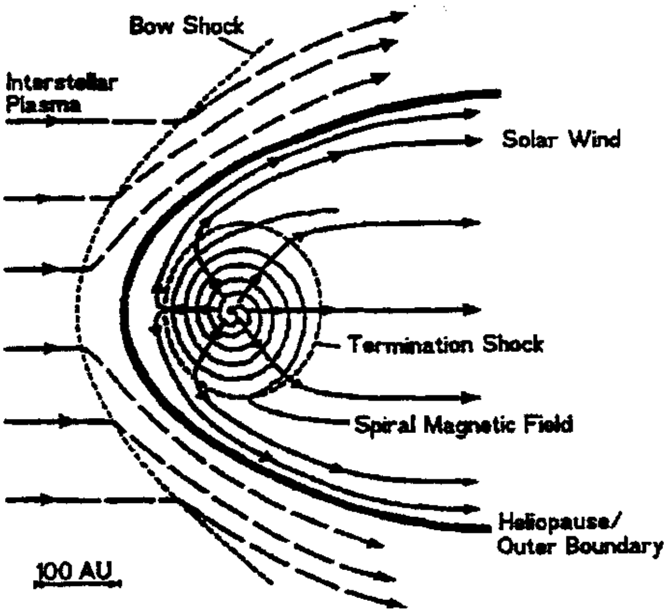

Figure 2.2: A schematic representation of the expected structure of the heliosphere, including the possible outer bow shock [*Jokipii*, 1989].

the sun [*Stone et al.*, 2005]. The layer between the termination shock and the heliopause is known as the heliosheath. If the interstellar plasma flows supersonically, a bow shock beyond the heliosphere will exist. This is widely regarded to exist at about 250 AU in the direction Voyager is currently travelling.

2.3 The Differential Rotation of the Sun

From surface observations it has long been known that the sun's rotation depends strongly on heliolatitude. This rotational behaviour of the photosphere was investigated by *Snodgrass* [1983], using observational data of magnetic features on the photosphere from the solar equator up to latitudes of 73° in both hemispheres. The data cover a period of more than 15 years, indicating that the rotational behaviour of the photosphere is fairly time-independent. Since the diffusion length scales of the magnetic features were significantly smaller than the rotational displacements of these features, their motions constituted sufficient tracers for the motion of the photosphere. The rotation profile of the photosphere was fitted with a standard function

$$\Omega(\theta') = A + B\sin^2\theta' + C\sin^4\theta', \tag{2.1}$$

where θ' is the solar latitude. Here, A denotes the absolute rotation rate, i.e. the rotation rate of the solar equator, Ω_{eq}. The coefficients B and C describe the differential rotation, i.e. rotation relative to $A = \Omega_{eq}$. The rotation rate of the photosphere (in μrad/s) was found to be

$$\Omega(\theta') = 2.902 - 0.464 \sin^2 \theta' - 0.328 \sin^4 \theta'. \tag{2.2}$$

When polar angles θ, also called co-latitudes, are used, the sine functions in Equation (2.2) are exchanged for cosine functions. The differential rotation rate is given by

$$\omega(\theta) = 0.464 \cos^2 \theta + 0.328 \cos^4 \theta \ \mu\text{rad/s}. \tag{2.3}$$

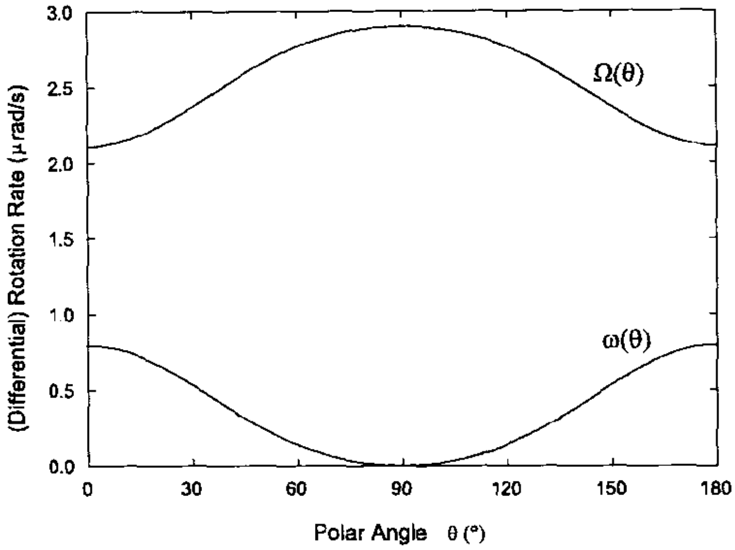

Figure 2.3: The rotation rate and differential rotation rate as function of polar angle, assuming that the expressions provided by *Snodgrass* [1983] remain valid in the polar regions.

Equations (2.2) and (2.3), assumed to remain valid in the polar regions, are drawn as function of polar angle in Figure 2.3. The rotation rate, $\Omega(\theta)$, increases from about 2.1 μrad/s $\approx$ 0.18 rad/day at the poles to about $\Omega_{eq} \approx 2.9$ μrad/s $\approx$ 0.25 rad/day at the equator. This corresponds to rotation periods of about 35 and 25 days, respectively. The behaviour of $\omega(\theta)$ is the inverse: a maximum rate of $\omega \approx 0.79$ μrad/s $\approx$ 0.068 rad/day is attained at the solar poles and decreases to zero at the equator. Note that $\Omega(\theta)$ is in a fixed observer's frame, while $\omega(\theta)$ is defined in the frame which co-rotates with the solar equator. In the following work, Ω_{eq} is abbreviated as Ω.

The rotation velocity of a magnetic feature in the photosphere is given by $\mathbf{V}_\Omega = \mathbf{\Omega} \times \mathbf{r}$, where $\mathbf{\Omega}$ is the angular frequency vector and $\mathbf{r}$ is the radial position vector of the feature. At a polar angle θ the absolute rotation speed is $V_\Omega(\theta) = \Omega(\theta) r_\odot \sin\theta$, where $r_\odot$ denotes the solar radius. Since the feature approximately remains at a constant latitude in the photosphere, it traces out a circular trajectory with radius $r_\odot \sin\theta$. Figure 2.4 shows the polar angle dependence of both the absolute rotation speed V_Ω and the differential rotation speed $V_\omega(\theta) = \omega(\theta) r_\odot \sin\theta$ of the photosphere, assuming that Equation (2.3) is valid for the whole photosphere. The absolute

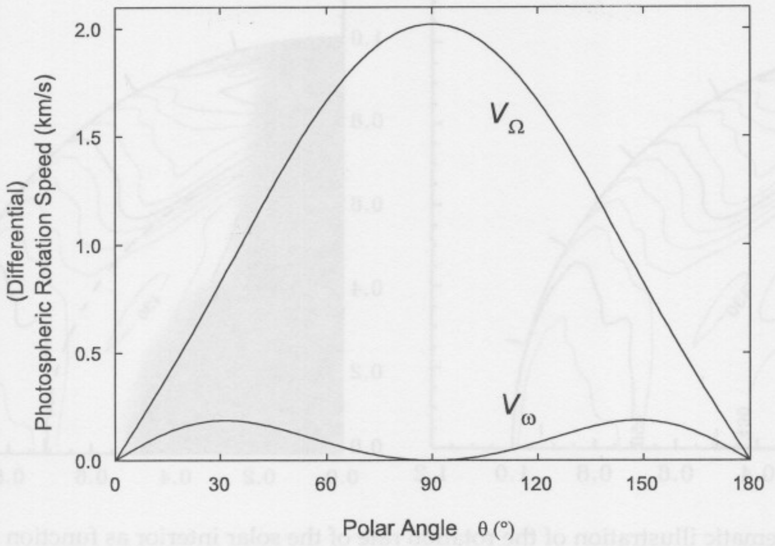

Figure 2.4: The absolute speed and differential speed of the photosphere as function of polar angle, assuming that Equation (2.3) describes the rotation rate of the whole photosphere. Note that V_Ω is measured in a fixed observer's frame, while V_ω is the speed in the co-rotating frame.

speed V_Ω is measured in a fixed observer's frame, while V_ω is the speed relative to the frame co-rotating rigidly with the solar equator. The largest rotation speed of a magnetic feature in the photosphere is attained at the equator, i.e. $V_{eq} \approx 2.0$ km/s. Snodgrass found a slight dimple of about 0.008 km/s in the rotation speed profile at the equator. This, however, is overwhelmed by V_{eq} and can therefore be neglected. Toward the pole, $\sin\theta$ approaches zero and the photosphere becomes essentially stationary in both the co-rotating and fixed observer's frames. The differential rotation speed V_ω attains a maximum of 0.19 km/s at a latitude of about 60° and drops to zero at the solar poles and equator.

Since the photosphere constitutes the topmost layer of the convection zone, its differential rotation is connected to the rotational behaviour of the solar interior. The angular velocity of the solar interior can be inferred from frequency splitting of acoustic oscillations in helioseismology. Such a study of solar oscillations allows for the investigation of the structure and dynamics of the solar interior. The frequency splitting is caused by the solar rotation, analogous to the splitting of the energy levels inside the hydrogen atom. Contours of constant angular frequency (in nHz) are shown in Figure 2.5 as function of the solar radius $r_\odot$ [*Schou et al.*, 1998]. Evidently, the rotation rate primarily increases with polar angle, as well as with radial depth inside the solar interior. The dashed line near the base of the convection region denotes the tachocline. This region of strong shear represents the transition between the latitudinal-dependent rotation of the outer convection zone and the nearly uniform rotation of the inner radiative zone.

Toward the solar poles and the inner regions of the sun, measurements of the rotation rate

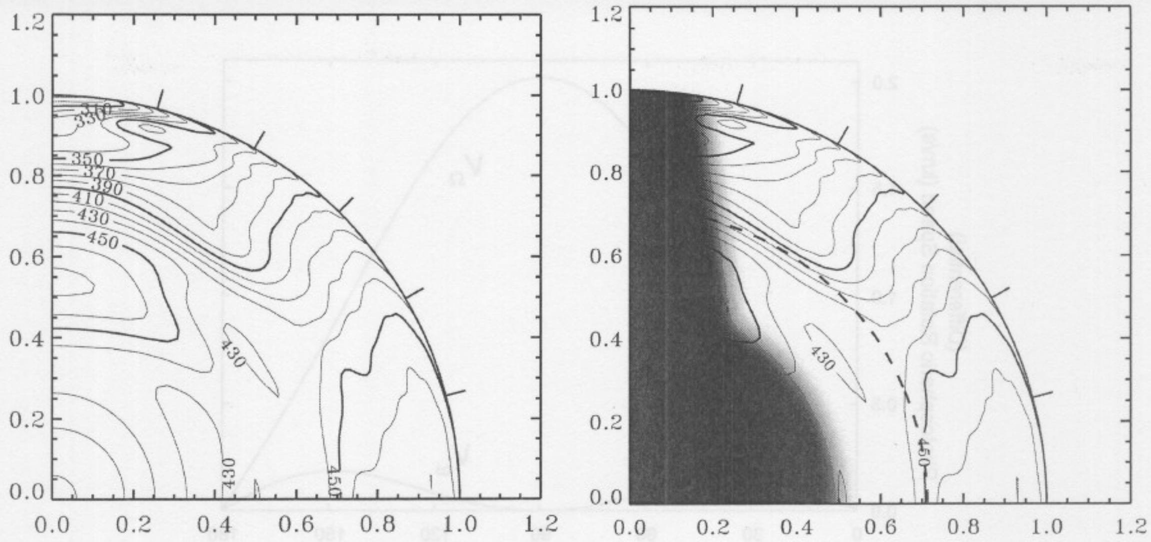

Figure 2.5: A schematic illustration of the rotation rate of the solar interior as function of $r_\odot$ for a cross-section through the solar poles, as obtained by helioseismology. The contours denote lines of constant rotation rate (in nHz). The shaded area in the right-hand figure indicates zones where the results are considered unreliable, and the dashed line indicates the location of the tachocline [*Schou et al.*, 1998].

become increasingly difficult. In Figure 2.5 the results in the shaded area are considered unreliable. At the pole the angular frequency is approximately 280 nHz, corresponding to a rotation period of about 41 days. This significantly exceeds the value of about 35 days obtained from Equation (2.2), indicating that either Equation (2.2) is inapplicable in the polar region, or the angular frequencies near the poles in Figure 2.5 are underestimations. For the purpose of this study, the latter is assumed.

The motion of the charged plasma particles inside the convection zone generates magnetic fields in the solar interior. The $\sim$ 22-year solar magnetic cycle probably originates inside the tachocline [see, e.g., *Kosovichev*, 2003, and references therein]. This is the discussion of the next section.

Interestingly, solar observations indicate that the solar corona tends to rotate more rigidly than the underlying differentially rotating photosphere, for a reason yet unknown [see, e.g. references in *Bird and Edenhofer*, 1990].

2.4 Solar Activity and the Origin of the Solar Magnetic Field

2.4.1 Historical Background of Solar Dynamo Models

It has long been known that the solar magnetic field is the source of solar activity and consequently the source of many interesting solar phenomena [see, e.g., *Kivelson and Russel*, 1996, for a historical overview]. In 1610, after inventing the telescope, Galileo Galilei and contemporaries extensively studied the dark spots on the photosphere, known as sunspots. In 1851, Heinrich Schwabe and Edward Sabine discovered that the number of sunspots varies with a mean period of ~ 11 years [cf. *Kivelson and Russel*, 1996]. Figure 2.6 shows this cycle dependence for sunspots observed during the last ~ 5.5 solar activity cycles [*Marshall Space Flight Center* webpage of NASA]. *Maunder* [1904] further investigated the properties of sunspots and found that the latitude distribution of sunspots varies with the same ~ 11-year period. He introduced the so-called 'butterfly' diagram, shown in Figure 2.7 [*NASA–Marshall Space Flight Center* webpage]. *Hale* [1908] discovered the existence of strong magnetic fields in sunspots by investigating the Zeeman splitting of sunspot spectra. He found that the leading spots in a sunspot pair have opposite polarities in opposite hemispheres, which alternate between successive sunspot cycles. This is known as Hale's law and led to the conclusion that the solar magnetic field oscillates with a mean period of ~ 22 years, reversing polarity every ~ 11 years. Therefore, the inclination of the magnetic axis $\mathbf{M}$ with respect to the rotation axis $\boldsymbol{\Omega}$ changes systematically, in other words, $\mathbf{M}$ rotates approximately in a meridional plane.

Several models have been proposed in order to explain the origin and maintenance of the solar magnetic field. The most accepted models are those based on turbulent dynamo theory, which describes how the toroidal (azimuthal) and poloidal (large-scale meridional) components of the solar magnetic field sustain one another due to the differential rotation and turbulent motion of the plasma inside the convection zone. A historical overview of solar dynamo models is presented by *Choudhuri* [2000].

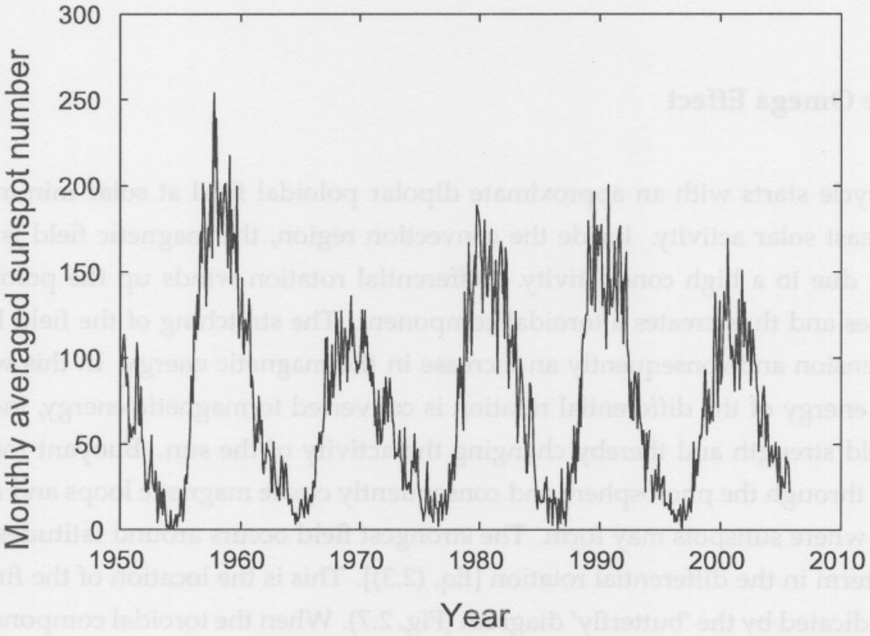

Figure 2.6: The sunspot cycle from January 1950 to September 2005, evidently depicting the ~ 11-year variation of the solar activity [*Marshall Space Flight Center* webpage of NASA (`http://science.msfc.nasa.gov`), courtesy of D. H. Hathaway].

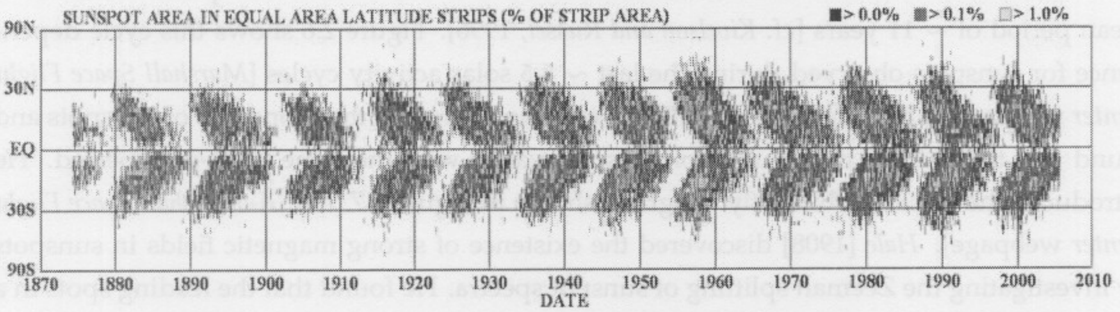

Figure 2.7: The butterfly diagram, showing the distribution of sunspots in latitude at different times. The darkest spots correspond to the largest sunspot area, averaged over individual solar rotations. The first spots appear at ∼ 30° and then migrate toward the solar equator. It is also apparent that the number of spots increases with solar activity [*Marshall Space Flight Center webpage* of NASA (`http://science.msfc.nasa.gov`), courtesy of D. H. Hathaway].

The basic theory of the turbulent solar dynamo was developed by *Parker* [1955b]. His model is based on the geophysical dynamo effect which describes the earth's magnetic field. The solar dynamo consists of two components: (1) the conversion from a poloidal field to a toroidal field due to differential rotation, known as the omega effect, after the symbol used to represent differential rotation; and (2) the conversion from a toroidal field to a poloidal field of opposite polarity due to the twisting of the field lines in the convection zone, called the alpha effect, after the Greek letter that looks like a twisted loop. The omega and alpha effects are illustrated in Figure 2.8 and 2.9, respectively. The figures were obtained on the *Marshall Space Flight Center* webpage of NASA.

2.4.2 The Omega Effect

The solar cycle starts with an approximate dipolar poloidal field at solar minimum, i.e. the period of least solar activity. Inside the convection region, the magnetic field is frozen into the plasma due to a high conductivity. Differential rotation winds up the poloidal field at low latitudes and thus creates a toroidal component. The stretching of the field lines creates magnetic tension and consequently an increase in the magnetic energy. In this way some of the kinetic energy of the differential rotation is converted to magnetic energy, increasing the toroidal field strength and thereby changing the activity of the sun. Buoyant toroidal loops may pierce through the photosphere and consequently create magnetic loops and active, bipolar regions where sunspots may form. The strongest field occurs around latitudes of 30°, due to the $\sin^2$ term in the differential rotation [Eq. (2.3)]. This is the location of the first active regions, as indicated by the 'butterfly' diagram (Fig. 2.7). When the toroidal component becomes dominant, the twisted field lines may reconnect into a large, axially symmetric toroidal field after a few solar rotations. During this period, the sun reaches its most active state in the solar cycle.

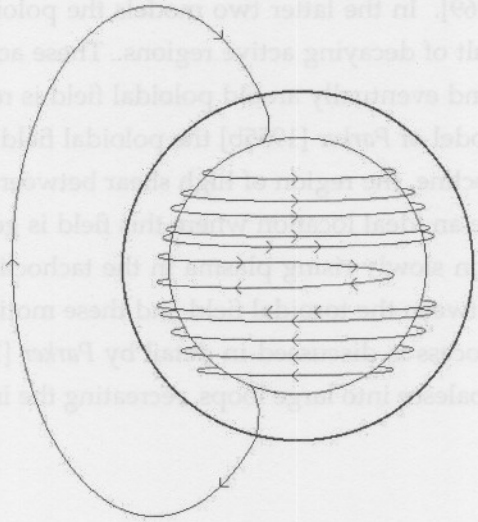

Figure 2.8: A representation of the omega effect, illustrating the effect of differential rotation on a poloidal field line, generating a toroidal field. The outer circle denotes the photosphere and the inner circle the tachocline, i.e. the region where the solar dynamo probably originates. [NASA's *Marshall Space Flight Center* webpage (`http://science.msfc.nasa.gov`), courtesy of D. H. Hathaway].

2.4.3 The Alpha Effect

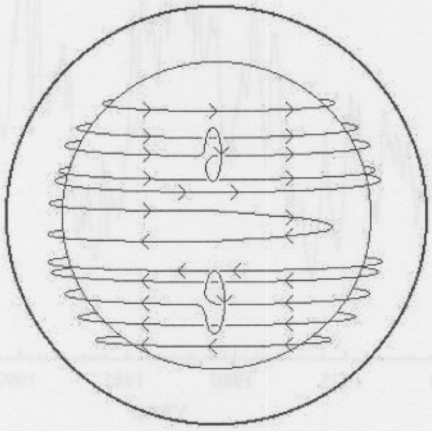

Figure 2.9: The alpha effect, illustrating the stretching of toroidal field lines due to convection in the convection zone. This eventually leads to a poloidal field, completing the solar activity cycle. In the Babcock-Leighton models, the alpha effect is produced near the photosphere; in the models based on the Parker-model, the effect is located in the tachocline [*Marshall Space Flight Center webpage* of NASA (`http://science.msfc.nasa.gov`), courtesy of D. H. Hathaway].

The interaction between the plasma and toroidal field in the convection zone can generate a poloidal field of opposite polarity. These models are based on the phenomenon that convecting plasma parcels stretch out the parts of the toroidal field lines that are frozen into them. Proposed models are mostly either based on the model of *Parker* [1955b] or the models of *Bab-*

cock [1961] and *Leighton* [1969]. In the latter two models the poloidal field is produced near the solar surface as the result of decaying active regions. These active regions migrate to the poles of opposite polarity and eventually an old poloidal field is replaced by a new one with opposite polarity. In the model of *Parker* [1955b] the poloidal field is produced deeper inside the solar interior. The tachocline, the region of high shear between the convection and radiative zones, has proved to be an ideal location where this field is generated (see Fig. 2.5). The effect of the Coriolis force on slowly rising plasma in the tachocline produces cyclonic fluid motions. The interaction between the toroidal field and these motions generates flux loops in meridional planes. This process is discussed in detail by *Parker* [1955b]. After several solar rotations these loops may coalesce into large loops, recreating the initial poloidal field, now of opposite polarity.

2.4.4 Attributes of Solar Cycle Models

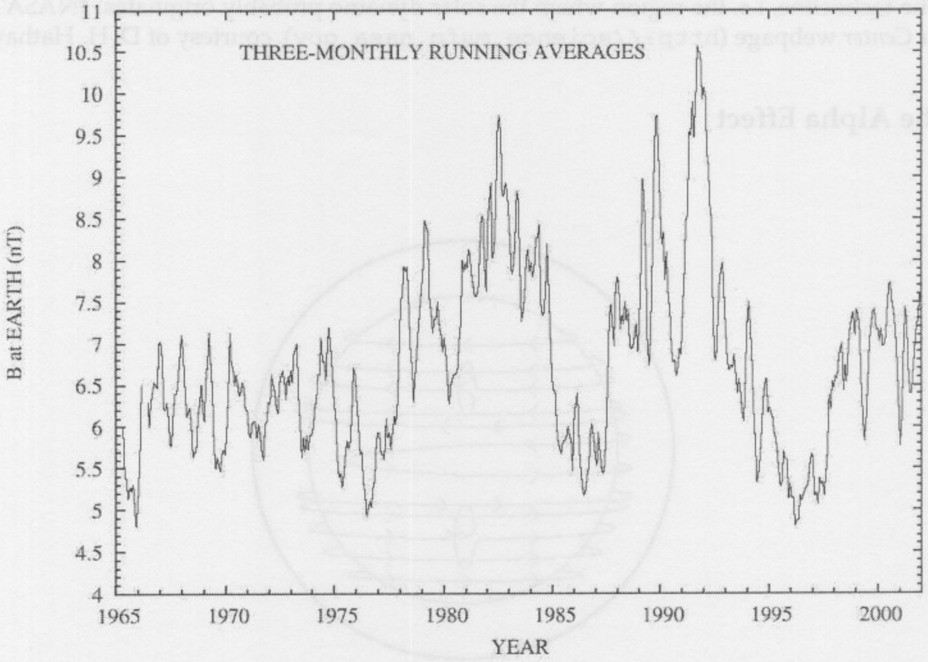

Figure 2.10: Three-monthly running averages of the solar magnetic field strength at the earth from 1965 to 2001. The ~ 11 year solar activity period is evident. [*Caballero-Lopez et al.*, 2004]

The decaying active regions in the Babcock-Leighton model and the helical turbulent plasma in the Parker model extract energy from the toroidal field and release this energy to the solar interior in the form of kinetic energy. During periods of increasing solar activity the opposite occurs. In this way the magnetic field strength in and above the photosphere changes significantly with solar activity. The dynamo models therefore constitute kinetic models. The magnitude of the field observed at the earth shows the same ~ 11 year period, as illustrated in Figure 2.10 [*Caballero-Lopez et al.*, 2004]. From solar minimum to solar maximum conditions the magnitude increases with a factor of up to ~ 2.

Some other proposed models for the solar cycle are based on oscillator theories, e.g. the oscillation of a deap-seated primordial solar magnetic field [e.g. *Layzer et al.*, 1979] or the large-scale oscillation of the heliosphere, analogous to an LC oscillator, where the heliospheric current system provides the inductance and the accumulated charge near the termination shock provides the capacitance [*Gurnett and Dangelo*, 1982]. These models, however, are not mathematically as well developed as the kinetic dynamo models.

The ~ 22 year magnetic cycle is composed of two ~ 11 year solar activity cycles with opposite magnetic polarities. Solar activity cycles were originally known as sunspot cycles. In this work, a solar cycle refers to an activity cycle. These cycles start at solar minimum activity and have been numbered since 1755 [*Gombosi*, 1998]. The current (2005) activity state is near the end of Solar Cycle 23.

The magnetic field that is generated in the solar interior features significantly above the surface. This will be discussed in the next section.

2.5 The Coronal Magnetic Field

The magnetic field from the photosphere to the solar corona is known as the coronal magnetic field (CMF). In this section the components and properties of this field are discussed. Open and closed field lines, the reconnection of field lines and some features that contribute to the activity of the CMF are also discussed. Lastly, some models of the CMF are described.

2.5.1 Magnetic Loops and Sunspots

Buoyant toroidal loops that are frozen into supergranules emerge frequently from the photosphere. The footpoints of these loops then migrate to the edges of the supergranules with the convective flow inside them [*Schrijver et al.*, 1998]. In this way the field lines become concentrated in the network lanes between supergranules. The toroidal field is the strongest in and near active regions. The 'butterfly' diagram (Fig. 2.7) is a good representation of the distribution of active regions on the photosphere, due to the connection of sunspots to these regions. It is evident that the toroidal field is the strongest at low latitudes and the most loops are therefore expected at these locations. However, due to the presence of convection streams at all latitudes, the toroidal loops are also expected up to the polar regions. Indeed, loops of various sizes have been observed on the whole photosphere and mostly small loops inside coronal holes [see, e.g., *Wiegelmann and Solanki*, 2004, and references therein]. Moreover, the number of loops is expected to be correlated with the number of sunspots during the solar activity cycle (see Fig. 2.6) and therefore to increase with solar activity.

The footpoints of the smallest loops are located inside a single network lane between granules or inside the lanes on opposite sides of a single or a few granules. Inside coronal holes (see Section 2.5.2) the footpoints of the largest loops are located on opposite sides of supergranules, separated by $\sim 3 \times 10^4$ km, the typical size of the supergranule. The corresponding height of such a loop is about the half of its width, i.e. $\sim 1.5 \times 10^4$ km. Outside coronal holes, loops are found to be much larger, with heights that range between 4×10^4 km and 4×10^5 km and footpoints separated by several supergranules. These large loops, known as coronal loops, are created by means of the coalescence of smaller loops, rather than a single large loop which emerges from underneath the photosphere [*Handy and Schrijver*, 2001]. Coronal loops have been studied systematically by e.g. *Feldman et al.* [1999].

When the intense local magnetic fields of loop structures have typical strengths of ~ 0.3 T, effective heat conduction in the structure is constrained, which consequently leads to a significant temperature reduction. The cooler regions then appear darker than the ambient photosphere and are hence known as sunspots. A fully developed sunspot has a typical size of $\sim 10^4$ km.

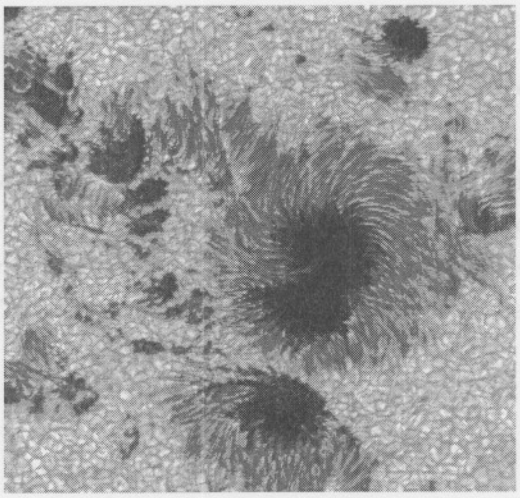

Figure 2.11: An image of an active region, containing a large sunspot pair and a group of smaller sunspots. The solar granulation patterns the background photosphere. Inside the umbra, the dark central region, only few granules are present. The fine filaments characterise the penumbra [*Scharmer et al.*, 2002].

Hale et al. [1919] discovered that the two sunspots in a pair nearly always have opposite polarities. The most obvious explanation is that a flux tube, i.e. a large loop structure, pierces through the photosphere and thus creates a bipolar pair on the photosphere. In each half of the bipolar pair a large sunspot or a group of sunspots forms, separated by $\sim 10^5$ km. Figure 2.11 [*Scharmer et al.*, 2002] shows a large sunspot pair and a group of smaller sunspots in an active region. The solar granulation, which patterns the background photosphere, is clearly visible. Note that no, or only very few, granules are present inside the sunspot due to ineffective conduction. The dark central region, called the umbra, is surrounded by the fine filaments of the penumbra. The sunspot further in the direction of the solar rotation is called the leading sunspot. According to Hale's law (see Section 2.4.1), this spot has the same polarity than the underlying hemisphere. The other sunspot in the pair, known as the trailing spot, has opposite polarity. The formation mechanism of sunspots from the toroidal field is described in detail by *Parker* [1955a]. Sunspots decay within a few months (or solar rotations) due to the underlying convection. Many aspects of sunspots can be explained by means of magnetoconvection, but the mechanism that determines the typical magnetic field strengths and sunspot sizes is still not completely understood.

2.5.2 Coronal Holes: Open Magnetic Field Structures

A coronal hole (CH) is a large-scale structure of open magnetic field lines in which a large number of fast solar wind streams flow. Particles from the photosphere and above can propagate easily along these field lines into the high corona. For this reason, CHs are the sources of the fast solar wind [*Nolte et al.*, 1976]. This wind has a lower proton density and temperature than the ambient plasma and therefore these regions appear dark in soft X-ray images. This explains the origin of the name 'coronal hole'. Not all open field structures have the characteristics of CHs. Many relatively small, open structures do not contain enough fast-moving particles to result in a fast wind stream which characterises CHs [see, e.g., *Zhao et al.*, 1999; *Hudson*, 2002].

Elongated CHs, called channels or grooves, were first observed by Waldmeier as early as 1956 and 1957 [*Waldmeier*, 1981, and references therein]. In 1972 they were rediscovered when soft X-ray images of the solar corona were taken [*Altschuler et al.*, 1972].

The locations of CHs are determined by a combination of the global poloidal (axisymmetric) and toroidal (non-axisymmetric) field components. CHs are observed not to be randomly distributed on the photosphere, but rather to appear in clusters, with a significant fraction located at certain longitudes and latitudes [*Bilenko*, 2004]. The mechanism of the formation and development of CHs is not yet fully understood. The most developed models are based on the solar dynamo theory. The observational properties of CHs provide important constraints for these models [*Fox et al.*, 1999].

CHs are grouped into three broad categories [*Harvey*, 1996]: (1) transient CHs, (2) polar coronal holes (PCHs) and (3) non-polar CHs.

2.5.2.1 Transient Coronal Holes

These holes are associated with eruptive events and have typical lifetimes of only one to two days. This category can therefore not be used to study the long-term properties of CHs.

2.5.2.2 Polar Coronal Holes (PCHs)

PCHs have been observed to expand significantly in latitude from the photosphere to the high corona at solar minimum conditions, eventually covering the largest fraction of the solar wind source surface [see, e.g., *Kopp and Holzer*, 1976; *Munro and Jackson*, 1977]. This property is investigated in detail in Section 5.6 as function of solar activity. PCHs have also been observed to be almost permanent features [e.g. *Waldmeier*, 1981]. This is probably the result of the meridional (poleward) flow of open magnetic flux [*Wang et al.*, 1991].

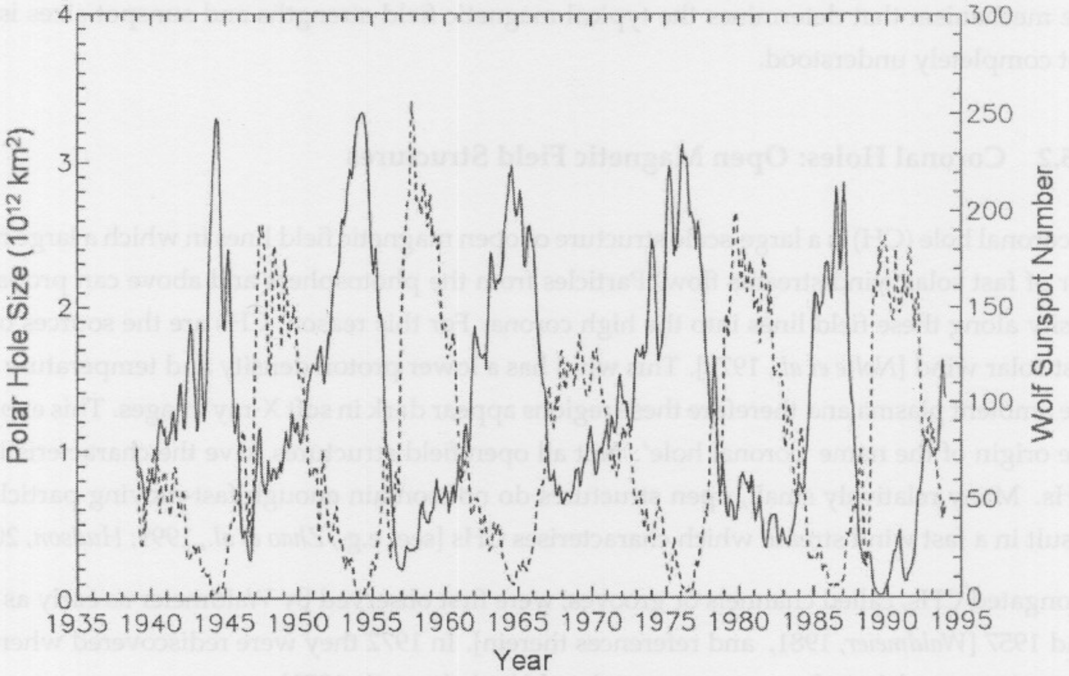

Figure 2.12: Monthly averages of the polar coronal hole (PCH) area on the photosphere (solid line) and the sunspot number (dashed line) [adapted from *Dorotovic*, 1996].

According to the solar magnetic cycle, PCHs change polarity every ~ 11 years. Furthermore, the PCH size anti-correlates reasonably accurately with the sunspot number, as shown in Figure 2.12 [adapted from *Dorotovic*, 1996], obtained from observations in the period from 1939 to 1993. The long-term behaviour of PCHs was investigated in detail by, e.g., *Waldmeier* [1981] and *Harvey and Recely* [2002]. The behaviour of a PCH during the magnetic polarity reversal process was studied by, e.g., *Fox et al.* [1999] and *Bilenko* [2002].

During solar minimum conditions, large PCHs cover the solar poles and non-polar CHs are located mainly in the equatorial region. As the solar activity increases, a large number of these CHs migrate toward the solar pole of opposite polarity [see, e.g., *Bilenko*, 2002]. Near solar maximum, particular small, mid-latitude CHs of the new-cycle polarity expand, rapidly drift into the polar region, merge and cover the polar cap within a few rotations. In this way the new-polarity PCH replaces the old-polarity hole, thereby reflecting the magnetic polarity reversal. The fragments of the old-polarity PCH gradually disappear or move to lower latitudes. The new-polarity PCH becomes larger and its position more symmetric about the pole within a few rotations. During the remaining period of the solar cycle, the PCH area gradually increases.

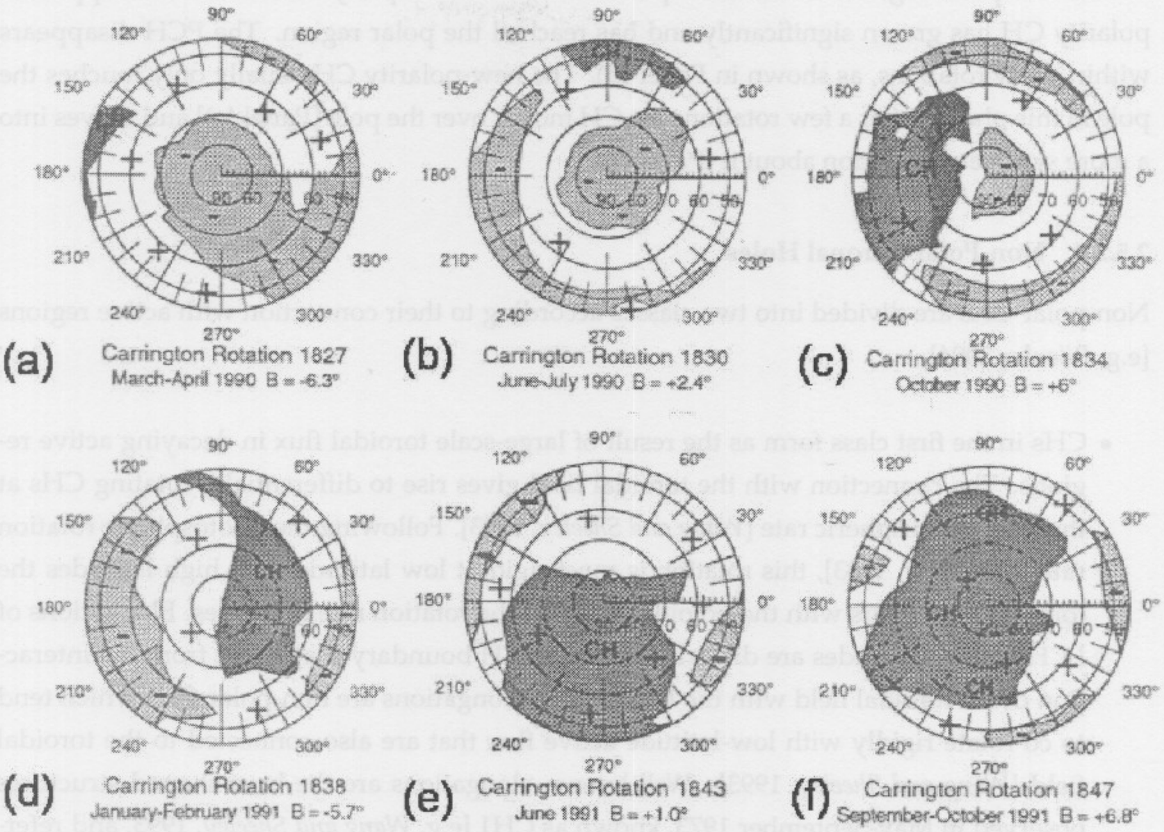

Figure 2.13: A selection of polar plots of the northern polar region around the polarity reversal of Solar Cycle 22. The lightly shaded regions denote negative-polarity regions; positive regions are left white. The darker shadings define the CH which becomes the new-polarity PCH [adapted from *Fox et al.*, 1999].

A selection of polar plots around the polarity reversal of Solar Cycle 22 in 1990-1991 is shown in Figure 2.13 [adapted from *Fox et al.*, 1999]. These plots illustrate the behaviour of the PCH and other CHs in the northern polar region of the photosphere. Negative-polarity regions are lightly shaded and positive regions are left white. The CH that develops into the new-polarity PCH is shaded darker. The average location of the CH boundaries in one Carrington Rotation is inferred from Hα synoptic charts and He I (λ1083 nm) spectroheliograms. (A Carrington Rotation is a period of $\sim$ 27.3 days, representing one complete rotation of the sun as seen from the earth. The first Carrington Rotation's starting date is 9 November 1853.) Since the CH locations are corrected for the effect of differential rotation, the values at the polar regions contain some uncertainties (see Fig. 2.5). Also shown on the polar plots is the B-angle. This angle is the tilt of the solar rotation axis toward the earth and its variation may affect the accuracy of the polar plots.

The first panel in Figure 2.13 shows the negative-polarity PCH, containing a large extension to mid-latitudes, and a positive-polarity, mid-latitude CH. In Figure 2.13(b) the extension of the PCH has become separated from the hole and the positive-polarity CH starts to drift rapidly toward the polar region. In the third panel the PCH has rapidly shrunk and the opposite-polarity CH has grown significantly and has reached the polar region. The PCH disappears within a few rotations, as shown in Panel (d). The new-polarity CH usually only touches the pole in this phase. After a few rotations the CH moves over the pole [Panel (e)] and moves into a more symmetric position about it [Panel (f)].

2.5.2.3 Non-Polar Coronal Holes

Non-polar CHs are divided into two classes according to their connection with active regions [e.g. *Bilenko*, 2004].

- CHs in the first class form as the result of large-scale toroidal flux in decaying active regions. The connection with the toroidal field gives rise to differentially rotating CHs at the local photospheric rate [*Wang and Sheeley*, 1993]. Following the photospheric rotation rate [*Snodgrass*, 1983], this rotation is most rigid at low latitudes. At high latitudes the toroidal flux shears with the poloidal flux and the rotation rate decreases. Elongations of PCHs to low latitudes are distortions of the PCH boundary that result from the interaction of the toroidal field with the PCH. These elongations are non-polar CHs which tend to co-rotate rigidly with low-latitude active flux that are also connected to the toroidal field [*Wang and Sheeley*, 1993]. Well-known elongations are the boot-shaped structures observed in May-September 1973, known as CH1 [e.g. *Wang and Sheeley*, 1993, and references therein] and in August-September 1996, known as the Elephant's Trunk [e.g. *Zhao et al.*, 1999; *Dobrzycka et al.*, 1999]. CHs in this class can persist for a few solar rotations.

- Nearly 70% of CHs belongs to the second class, in which the holes are not connected to active regions, but are governed by the global poloidal field [*Bilenko*, 2004] and therefore rotate rigidly with the heliographic equator. Since PCHs are also connected to the poloidal field, this field provides a strong connection between PCHs and these CHs [e.g. *Fox et al.*, 1999; *Bilenko*, 2002]. The common nature of PCHs and these CHs is reflected in several processes on the photosphere, such as the polar field reversal, the merger of CHs with PCHs and the separation of CHs from PCHs. Interestingly, elongations of the PCH to low latitudes are connected to active region and therefore belong to the first class [*Wang and Sheeley*, 1993].

  The rigid rotation of the CHs in this class supports the property that CHs in the photosphere should approximately co-rotate with the rigidly rotating magnetic field in the higher corona in order not to wind up [*Wang and Sheeley*, 1993]. This reflects the current-free nature of the solar corona, a property on which most of the CMF models are based (see Section 2.5.5).

  The typical lifetime of CHs in this class greatly exceeds that of the holes in the first class. CHs connected to PCHs, as well as CH clusters, usually exist for several solar rotations at solar minimum and even between one and two years at solar maximum [*Belenko*, 2001].

2.5.3 Magnetic Reconnection

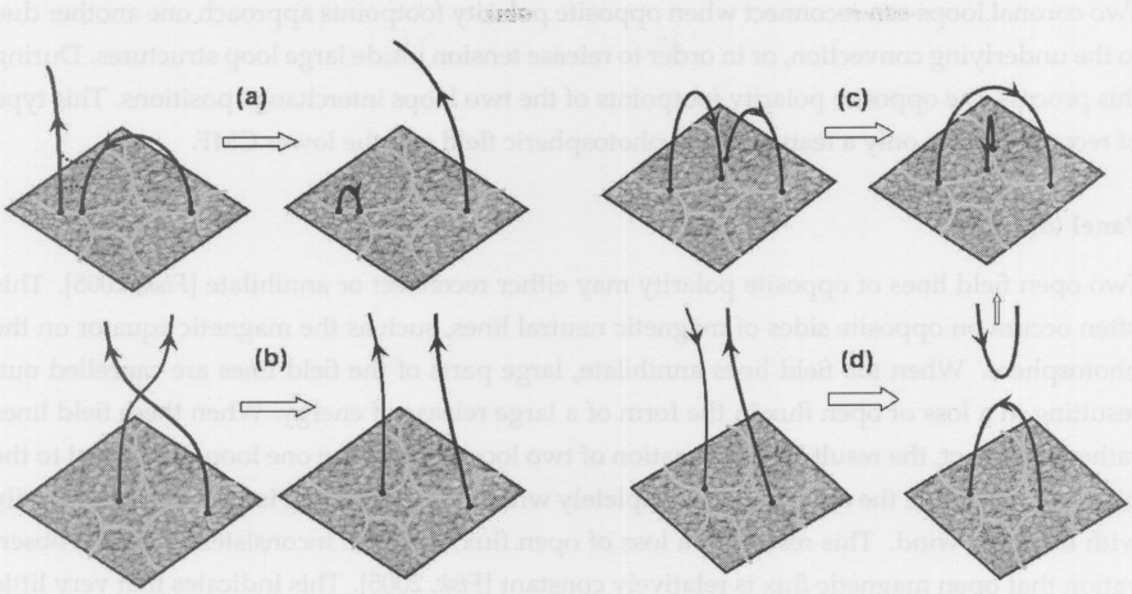

Figure 2.14: An illustration of reconnection between any two types of magnetic field lines. See text for detail.

Magnetic reconnection is the process which removes rapid, unstable changes in the field direction due to the stretching, twisting or bending of field lines. In the process two field lines 'break' and the free ends reconnect. This process may occur between any two types of field lines, as illustrated in Figure 2.14.

Panel (a)

When open and closed field lines reconnect, both field lines are displaced. This usually occurs when the open field line encounters the opposite polarity side of a coronal loop. The lower part of the open line reconnects with the nearby loop end, resulting in a small loop, and the remaining part of the open field line reconnects with the same-polarity side of the loop. In this way the footpoint of the open line and the opposite end of the loop interchange locations. The small loop usually disappears quickly beneath the photosphere, as discussed by *Fisk* [2005]. This type of reconnection occurs frequently above the photosphere, especially at CH boundaries.

Panel (b)

In order to release tension, two same-polarity open lines can reconnect and consequently interchange footpoints. This frequently occurs at regions where parts of the field lines are frozen into turbulent plasma and start to 'wind up'.

Panel (c)

Two coronal loops can reconnect when opposite polarity footpoints approach one another due to the underlying convection, or in order to release tension inside large loop structures. During this process, the opposite polarity footpoints of the two loops interchange positions. This type of reconnection is only a feature of the photospheric field and the lower CMF.

Panel (d)

Two open field lines of opposite polarity may either reconnect or annihilate [*Fisk*, 2005]. This often occurs on opposite sides of magnetic neutral lines, such as the magnetic equator on the photosphere. When the field lines annihilate, large parts of the field lines are cancelled out, resulting in a loss of open flux in the form of a large release of energy. When these field lines rather reconnect, the result is the formation of two loops, where the one loop is attached to the photosphere, while the other loop is completely within the corona and is convected outwardly with the solar wind. This results in a loss of open flux, which is inconsistent with the observation that open magnetic flux is relatively constant [*Fisk*, 2005]. This indicates that very little reconnection and annihilation occur, and that open field lines rather reconnect with coronal loops in order to release magnetic tension.

Since reconnection requires the dissipation of electric currents, it does not occur when the field is frozen into a perfectly conducting plasma [cf. *Harra and Mason*, 2004]. Reconnection therefore occurs more likely in the CMF where the magnetic field behaviour dominates that of the ambient plasma.

2.5.4 Other CMF Phenomena

Pressures in the CMF result in many interesting phenomena in the corona, such as solar flares, prominences and coronal mass ejections. These features create large currents in the CMF that may extend into the interplanetary space. The number and intensity of these features increase with solar activity. During high activity periods, the resulting CMF is highly time-dependent and unpredictable.

A solar flare is an explosive release of energy from an active region in the form of electromagnetic radiation and particles. This feature is probably caused by a sudden large perturbation of the magnetic field and then the very rapid dissipation of this large amount of magnetic energy.

When plasma in the chromosphere gets trapped in large magnetic structures, usually within flux tubes between sunspot groups, it can become significantly denser than the ambient plasma and then appear as elongated structures above the photosphere. These features are called prominences. They can stay suspended for several months and reach altitudes of several solar radii. Prominences that are observed on the solar disc appear as dark lines against the hotter, bright background and are known as filaments. Prominences can occur in many different forms, from large, quiescent, long-lived features to small, highly active, short-lived features. When they become unstable, rather than collapse, they break loose from the sun in an eruption. Such an eruption varies significantly in intensity, depending on its size and activity. Quiescent prominences can simply fade away after an eruption, whereas an active prominence may explode and let the material leave the sun entirely. Such a phenomenon is known as a coronal mass ejection (CME).

Most CMEs originate from plasma trapped in closed magnetic field regions, such as prominences. The plasma pressure may then increase, until the magnetic field cannot constrain the plasma anymore and the structure explodes. CMEs initially move outward along magnetic field lines. In the higher corona they often pull magnetic field lines along and the resulting CME loops propagate far into the heliosphere. During solar minimum conditions a CME occurs typically once every few days. Toward solar maximum conditions the solar magnetic field gets more active and up to ~ 10 events can be observed daily.

Large, bright, cap-like coronal structures with long pointed peaks usually overlie sunspots and active regions and often contain prominences at their bases. These structures are known as helmet streamers. They are formed by magnetic loop structures suspending coronal material and thereby causing dense structures. The helmet streamers usually extend into the high corona. The topmost loops are then captured by the solar wind, thereby producing the characteristic pointed peaks.

Sunspots are preceded by large, bright regions, known as faculae (literally 'little torches' in Latin). Faculae are caused by concentrations of magnetic field lines with a much smaller strength than the field structures within sunspots. The bright, dense regions which overlie sunspots and fluctuate with the same $\sim$ 11-year cycle are called plages (from the French word for 'beach').

Long, thin, bright concentrations of plasma in the chromosphere often follow open magnetic field lines at the solar poles into the corona during periods of low solar activity. These streamers are called polar plumes and are formed by the action of the solar wind similarly to the long peaks of helmet streamers. The brightest plumes have been observed at altitudes of more than 40 $r_\odot$ above the photosphere. Some features of polar plumes are used in Chapter 5 to construct a time-dependent model for the field from CHs.

2.5.5 Modelling the CMF: The Potential Field Source Surface Model

In the convection zone and photosphere, the plasma proton density and pressure are significantly larger than that of the magnetic field. This implies that the plasma-β, defined as the ratio between the plasma and magnetic pressures, is large in these regions and the magnetic field motion is dominated by the plasma motion, i.e. the field is essentially frozen into the convecting plasma. This frozen-in condition can also be described in terms of the conductivity of the solar wind. The solar wind is a highly ionised plasma with a large electric and thermal conductivity. When the conductivity of a plasma is infinitely large, a magnetic field within the plasma cannot move relative to the plasma, according to Lenz's law.

On small scales the magnetic field in and above the photosphere has a complicated, time-dependent structure due to varying concentrations and orientations of open field lines and loop structures. Such a field can be described by a spherical harmonic expansion. However, the higher order terms of such an expansion fall off much more rapidly with distance than the first-order dipolar term. Near solar minimum the poloidal field dominates and a simple dipole is a reasonable first-order description of the field on large scales. Such a dipole field is called a potential field. The first attempts to construct CMF models were based on potential fields.

After the seminal work of *Parker* [1958], better understanding of the behaviour of the solar magnetic field emerged. A current-free model of the CMF was first employed by *Rust* [1966] on a small scale and extended by *Newkirk* [1967] for a larger scale. Such a model is a reasonable description of the CMF near solar minimum conditions [*Schatten et al.*, 1969]. The motivation of a current-free CMF model will now be discussed.

The solar atmosphere is a complex plasma structure in which the magnetic and plasma pressures interchange dominance [see, e.g., *Gary*, 2001]. The magnetic pressure, also known as the magnetic energy density, is defined as $B^2/(8\pi)$ (in Gaussian units) or $B^2/(2\mu_0)$ (in SI units), where B is the field magnitude, i.e. the field density, and μ_0 is the permeability constant. The plasma pressure p is also known as the kinetic energy density $(1/2)\rho v^2$, where ρ is the plasma mass density and v the average plasma particle speed [cf. *Choudhuri*, 1998]. From these relations the plasma-β can easily be determined.

Above the photosphere the plasma proton density diminishes very rapidly, while the magnetic density decreases only moderately. This implies that $\beta < 1$, meaning that most of the plasma particles follow the CMF lines from the photosphere into the chromosphere and low corona. However, above $\sim 1.2\, r_\odot$, the behaviour of the plasma and magnetic field pressures in coronal streamers and inside CHs differ significantly [*Suess et al.*, 1996; *Gary*, 2001]. Magnetohydrodynamic (MHD) models of the global corona reveal that $\beta > 1$ is a general property of coronal streamers and other active regions above $1.2\, r_\odot$, while $\beta < 1$ is the condition in the largest parts of CHs. In coronal streamers, the magnetic density decreases drastically more with height than the plasma proton density, and the plasma-β attains very large values in the corona, implying that the magnetic field behaviour is dominated by that of the plasma. Global simulations indicate that the large pressure in streamers is balanced by the pressure from the adjacent CHs. In CHs, β decreases to $\lesssim 10^{-2}$ at several solar radii from the photosphere [*Fisk et al.*, 1999a, and references therein]. The field lines in the CHs expand superradially with height over the closed magnetic structures above active regions in order to relieve lateral magnetic stresses. When entering a CH above an active region, the plasma-β decreases rapidly. In the acceleration region, where the high corona accelerates radially outward to form the solar wind (see Section 2.2), β increases again. The radial distance up to where the magnetic energy remains larger than the kinetic energy of the plasma is known as the Alfvén radius, estimated at 10 $r_\odot$ [see *Choudhuri*, 1998, and references therein]. Beyond this radius, β largely exceeds unity and the magnetic field motion is almost completely dominated by the plasma motion, i.e. the field is essentially frozen into the solar wind.

Magnetic loops of the poloidal field having a large enough scale to permeate the high corona are captured by the solar wind and become open field lines. These field lines are essentially frozen into the wind and follow it to the outer heliosphere. This frozen-in field, which fills the entire heliosphere, is called the heliospheric magnetic field (HMF). In the acceleration region a virtual surface can be defined from where the solar wind and hence the HMF lines extend radially into the outer heliosphere. This surface is approximately spherical and is commonly known as the (solar wind) source surface (SS), for reasons that will become clear in Section 3.2. Since $\beta < 1$ in the low corona inside CHs, the force-free condition, $\mathbf{j} \times \mathbf{B} = 0$, is a reasonable description of the CMF in this region during low solar activity conditions. In order to simplify calculations, it is further assumed that no currents are present in this region. The magnetic potential can then be solved from Laplace's equation and the magnetic field can be derived. Two boundary conditions, which follow from observations, are specified: the magnetic field is assumed to be radial on both the photosphere and the SS. The consequent field provides a representation of the CMF from the photosphere to the SS, consisting of a large network of open lines, coronal loops and even some features such as prominences. These current-free CMF models are commonly known as potential field source surface (PFSS) models, since the simulated field is confined between a potential field on the photosphere, and the SS.

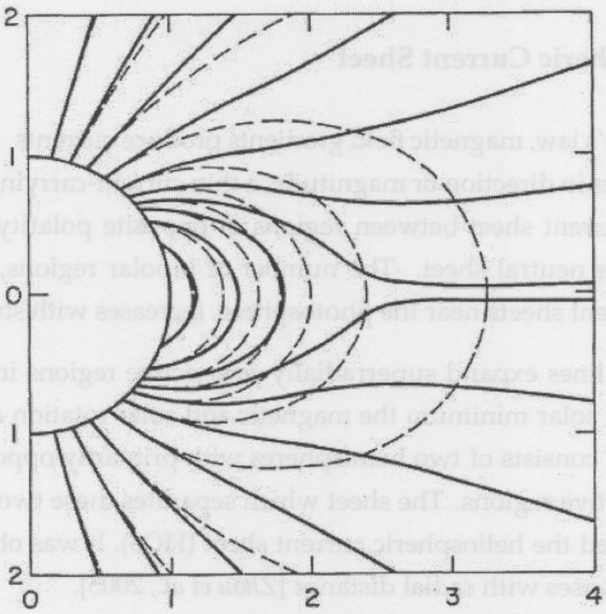

Figure 2.15: A simple model of the CMF configuration, simulating the effect of the solar wind on the field lines by employing a PFSS model. The wind stretches out the field lines of a potential magnetic field (dashed lines), opening it up into interstellar space [*Pneuman and Kopp*, 1969].

Pneuman and Kopp [1969] were the first to simulate the CMF numerically and schematically by employing a simple steady-state PFSS model. Ampère's law and the continuity, momentum and induction equations were solved iteratively and an isothermal plasma flow and an initial dipolar magnetic field were used. Figure 2.15 illustrates how a potential field (dashed lines) is transformed by the solar wind: the dipolar field lines which originate at mid-latitudes on the photosphere are pulled radially outward in the high corona, and the field lines originating at high latitudes are captured by the solar wind to become open. The boundary condition which constrains the field lines to be radial on the SS simulates the MHD effect of the solar wind.

The PFSS model has evoked some criticism [e.g. *Hudson*, 2002; *Gary*, 2001; *Fisk*, 2005]. Firstly, the small plasma energy density required for this model implies that the energy storage needed for CMEs, flares and non-radial streamers cannot be described by it. Secondly, some physical properties of the CMF are inconsistent with the force-free and current-free conditions essential to the PFSS model, e.g. the SS above active regions is 'sandwiched' between two regions where $\beta > 1$, i.e. where the magnetic field behaviour is dominated by the plasma behaviour, and the magnetic field is observed to diffuse on and above the photosphere, but can only do so in the presence of currents. Nonetheless, the PFSS model serves reasonably well to predict solar wind flow speeds and even the locations of coronal holes [e.g. *Schatten*, 2001].

Improvements of the PFSS model were provided by, e.g., the MHD model of *Pneuman and Kopp* [1969] and the heliospheric current sheet model of *Schatten* [1971]. From more recent observational results, more reasonable boundary conditions were provided by *Hoeksema et al.* [1996] and *Wang and Sheeley* [1992].

2.5.6 The Heliospheric Current Sheet

According to Ampère's law, magnetic field gradients produce currents. At the location where a magnetic field changes in direction or magnitude, a thin current-carrying layer, called a current sheet, forms. The current sheet between regions of opposite polarity in a bipolar region is generally known as a neutral sheet. The number of bipolar regions, and consequently the number of small current sheets near the photosphere, increases with solar activity.

Open magnetic field lines expand superradially over active regions in order to release magnetic pressures. Near solar minimum the magnetic and solar rotation axes are approximately aligned and the CMF consists of two hemispheres with primarily opposite polarities at all locations well above active regions. The sheet which separates these two large regions with opposite polarity is called the heliospheric current sheet (HCS). It was observed to have a finite thickness which decreases with radial distance [*Zhou et al.*, 2005].

The meridional rotation of the rotation axis **M**, i.e. the change in the inclination of **M** with the solar cycle, causes the HCS to have a warped or wavy structure which increases with solar activity. The HCS is therefore frequently called the wavy current sheet (WCS). This structure is derived in Section 3.4. When the northern magnetic hemisphere is predominantly positive, the angle between $+\mathbf{\Omega}$ and $+\mathbf{M}$ is called the tilt angle. During the opposite polarity epoch, α is defined as the angle between $+\mathbf{\Omega}$ and $-\mathbf{M}$. The tilt angle, α, therefore denotes the smallest angle between $\mathbf{M}$ and $\mathbf{\Omega}$. Since the magnetic equator is perpendicular to $\mathbf{M}$, the angle between the magnetic and rotational equators is also α.

The Wilcox Solar Observatory (WSO) has recorded tilt angle data since May 1976 by calculating the maximum extent of the HCS in potential field models of the CMF. These data are obtainable from `http://quake.stanford.edu/~wso/wso.html`, courtesy of J. T. Hoeksema. Figure 2.16 shows the tilt angle values since 1976, calculated from the newer model that uses a radial boundary condition and $r_{SS} = 3.25\ r_{\odot}$. Note that the values above 70° constitute only lower limits. Interestingly, α becomes small, but never zero, which indicates that $\mathbf{M}$ does not rotate in an exact meridional plane, but always remains inclined to a larger or smaller degree with respect to $\mathbf{\Omega}$.

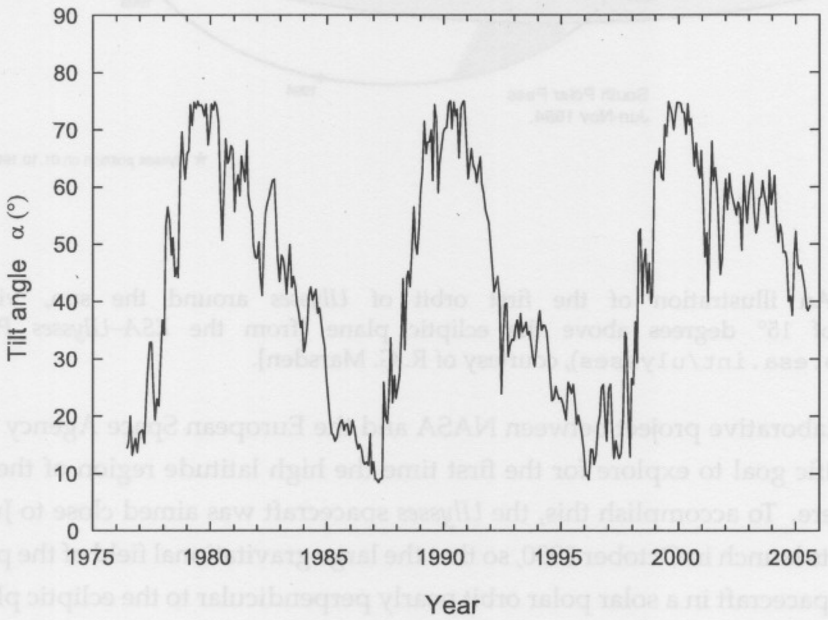

Figure 2.16: The $\sim$ 11-year variation of the tilt angle, α, from monthly-averaged data since 1976. Angles above 70° constitute lower limits [data from the Wilcox Solar Observatory (`http://quake.stanford.edu/~wso/wso.html`), calculated from the so-called 'new' model that uses a radial boundary condition and $r_{SS} = 3.25\ r_{\odot}$, courtesy of J. T. Hoeksema].

2.6 The Solar Wind

In Sections 2.2 and 2.5.5 it was discussed how the solar plasma follow the CMF lines continually to the outer corona and expands radially outward at supersonic speeds in order to maintain dynamic equilibrium. This expanding solar plasma, called the solar wind, pulls the

CMF lines along, determining the basic structure and some important properties of the field. It is therefore essential to discuss some properties of the solar wind.

2.6.1 The *Ulysses* Mission

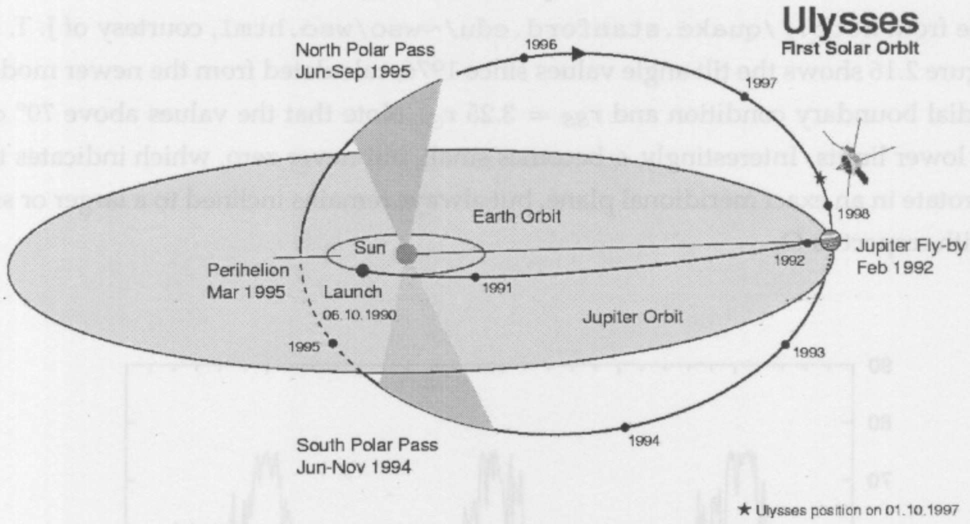

Figure 2.17: An illustration of the first orbit of *Ulysses* around the sun, viewed from a perspective of 15° degrees above the ecliptic plane [from the *ESA–Ulysses Project Office* (`http://helio.esa.int/ulysses`), courtesy of R. G. Marsden].

Ulysses is a collaborative project between NASA and the European Space Agency (ESA) with its main scientific goal to explore for the first time the high latitude region of the sun in the inner heliosphere. To accomplish this, the *Ulysses* spacecraft was aimed close to Jupiter from the earth after its launch in October 1990, so that the large gravitational field of the planet could accelerate the spacecraft in a solar polar orbit nearly perpendicular to the ecliptic plane and up to a maximum latitude of 80.2°.

In June 2004, *Ulysses* completed its second orbit with a period of about 6.3 years. The two completed orbits are shown in Figures 2.17 and 2.18, respectively. (The figures were obtained from the *ESA–Ulysses Project Office* on `http://helio.esa.int/ulysses`, courtesy of R. G. Marsden.) The location of the spacecraft at the beginning of every year, as well as other relevant information, is indicated on the figures. Note that the second orbit of *Ulysses* is viewed from a perspective which shows the 80° inclination of the orbit with respect to the ecliptic plane.

Each orbit can be divided into different stages. The first stage comprises a slow south polar transit, reaching 80° S at around 2.4 AU from the sun. Then a fast latitude scan (FLS) to 80° N at a relatively constant solar distance is performed within ~ 10.5 months. In the first (second)

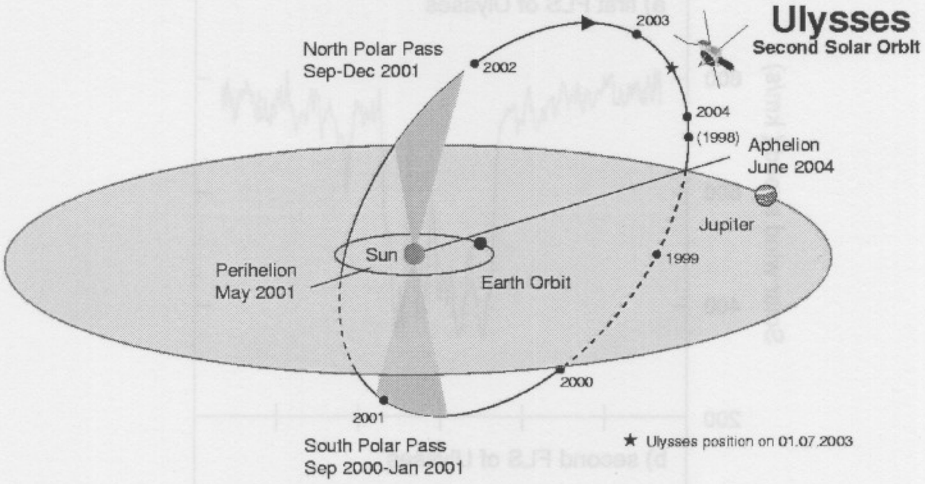

Figure 2.18: An illustration of the second orbit of *Ulysses*, viewed from a perspective which shows the 80° inclination of the orbit with respect to the ecliptic plane [from the *ESA–Ulysses Project Office* (`http://helio.esa.int/ulysses`), courtesy of R. G. Marsden].

orbit this was performed during solar minimum (maximum) activity, thereby providing valuable information about conditions at various levels of solar activity. The last stage describes the return to the ecliptic plane.

2.6.2 Latitude Dependence of the Solar Wind

The latitude dependence of the solar wind speed, observed by *Ulysses* during each FLS, is shown in Figure 2.19 for each orbit. Note that *Ulysses* travelled from south to north during each FLS, implying that time runs from right to left in the figures. (The data were obtained from the Space Physics Data Facility of the *NASA–Goddard Space Flight Center* webpage on (`http://lewes.gsfc.nasa.gov`), courtesy of R. McGuire.) *Ulysses'* first FLS was performed from September 1994 to August 1995 during the minimum solar activity period. Evidently, the wind speed can be divided into two latitude regions: a fast wind with a speed of $\sim 700 - 800$ km/s from the poles to a latitude of about 22.5°, and alternating streams of moderate and relatively slow wind streams at low latitudes. The average wind speed in the low latitude (slow wind) region is $\sim$ 450 km/s [*Goldstein et al.*, 1995]. The rapid transition in the region between the fast and slow winds occurs within a few degrees.

The second FLS was performed from November 2000 to October 2001. This period started at solar maximum and covered the first part of the declining solar activity. The large speed variation of the wind streams is evident. The average wind speed changed significantly from

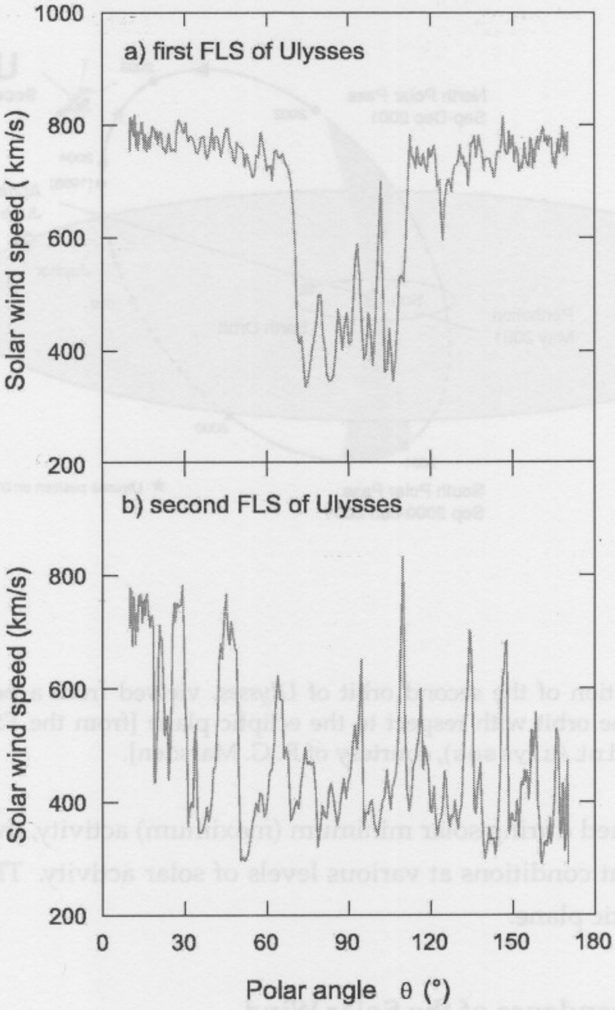

Figure 2.19: The latitude dependence of the solar wind speed from the *Ulysses* observations during the two completed FLSs. In both panels time runs from right to left. [Data from the Space Physics Data Facility of the *NASA–Goddard Space Flight Center* (`http://lewes.gsfc.nasa.gov`), courtesy of R. McGuire].

pole to pole. It started with an average speed of ~ 400 km/s at solar maximum in the southern polar region and increased with decreasing solar activity to ~ 600 km/s in the northern polar region.

The two panels in Figure 2.19 indicate that the solar wind speed profile changes significantly with solar activity. In order to understand this behaviour, the distribution of the fast and slow wind streams during the development of the solar activity cycle first needs to be explained.

The Origin of the Fast and Slow Wind Speed Components

A simple representation of the location of the fast and slow wind streams is illustrated in Figure 2.20 [*Dryer*, 1987]. The high speed wind emerges primarily from PCHs, because the

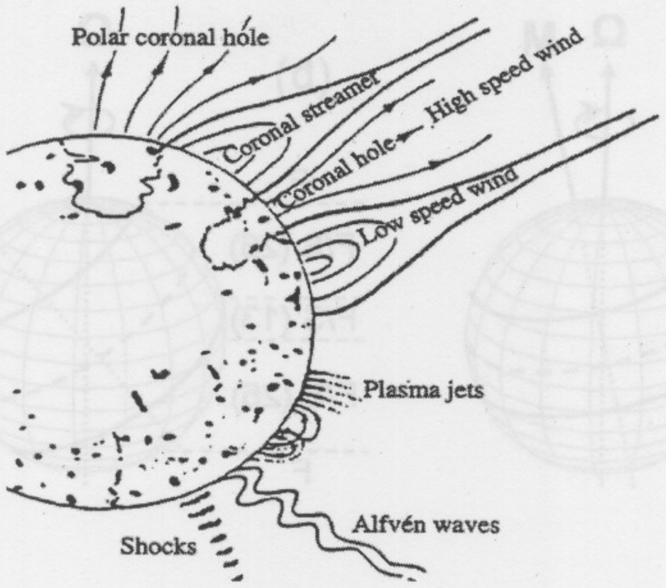

Figure 2.20: A representation of the fast solar wind connected to the open magnetic field lines from coronal holes and the slow wind associated with coronal streamers above coronal loops [*Dryer*, 1987].

plasma can move relatively unrestrictedly along the field lines from these structures to the high corona. The inner regions of CHs also contribute to the fast wind, but to a lesser extent (see Section 2.5.2). During the largest period of the solar activity cycle, both solar poles are covered with a PCH and therefore only fast wind streams are present at high latitudes. Fast streams occur also at lower latitudes and in the equatorial region, wherever CHs are present. The main component of the slow wind originates near CH boundaries where the plasma can escape the confining effect of coronal loop structures. This component propagates mainly along the open field lines that define the edges of coronal streamers. Plasma which follows the open field lines in small structures above active regions, as well as the escaping particles in the remaining part of the corona, contributes to the slow wind to a lesser extent.

The Influence of Solar Activity on the Wind Speed Profile

The slow solar wind is confined almost entirely to a relatively narrow latitude band, known as the streamer belt, centred on the HCS. *Ulysses* observations near solar minimum indicate that the width of this streamer belt ranges between about 20° and 30° on both sides of the HCS [see, e.g., *Gosling et al.*, 1995]. Figure 2.21 shows a simple representation of the distribution of the slow and high speed winds at the SS for (a) low and (b) moderate solar activity conditions. The HMF and HCS are assumed to originate at the SS. The streamer belt (solid lines) and the HCS (dashed line) are shown on this surface. First consider a time-stationary observer detecting the solar wind from the rotating sun near solar minimum [Fig. 2.21(a)]. The heliolatitude ranges where only the fast wind or the slow wind is detected, are denoted by F and S, respectively. Due to the inclination of the HCS with respect to the solar equator, and the almost rigidly rotating HCS and streamer belt, two latitude ranges exist where fast and slow winds alternate

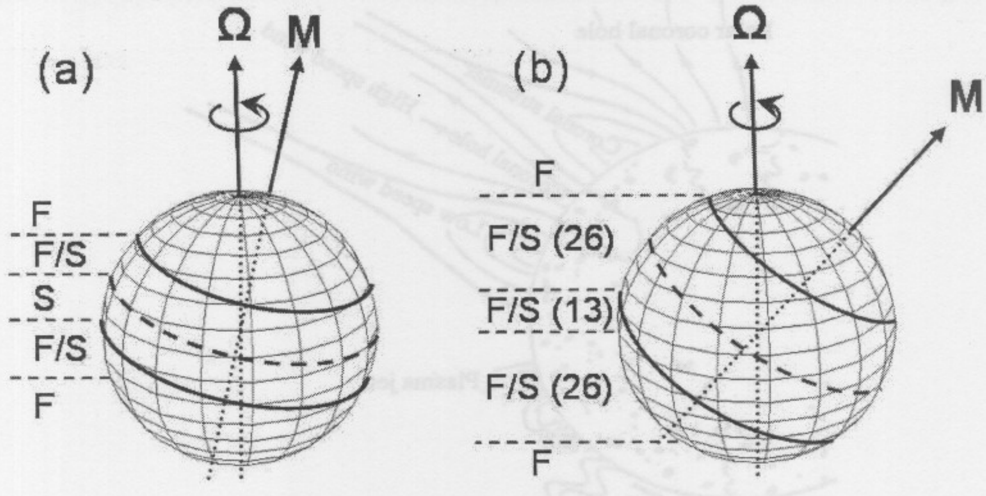

Figure 2.21: A representation of the streamer belt on the SS and the heliolatitudinal locations of the fast (F) and slow (S) solar winds for (a) low and (b) moderate solar activity conditions. Regions where the fast and slow winds alternate are denoted by F/S. In the left panel the fluctuation period is ~ 26 days; in the right panel the approximate fluctuation period (in days) is given in brackets.

with a period of ~ 26 days. This region is denoted by F/S.

The first FLS occurred at solar minimum when the HCS was almost aligned with the heliographic equator and the F/S-region very narrow. *Ulysses* therefore travelled relatively rapidly through the F/S-region and the 26-day variations are not expected to be apparent. This expectation is confirmed by Figure 2.19(a), revealing the abrupt transition between the two wind components. Inside the slow wind region S, smaller fluctuations in the wind speed occur as the result of faster streams that penetrate the slow wind region due to ragged PCH boundaries, spatial variability in the coronal expansion and CHs located in this region.

During increasing solar activity, the PCHs decrease significantly in size and the number of active regions increases [see, e.g., *Waldmeier*, 1981; *Belenko*, 2001]. This implies that the fast wind region decreases with solar activity and the slow wind region covers a broader heliomagnetic latitude range about the HCS. The width of the streamer belt was observed to change from ~ 20° at solar minimum to ~ 35° at higher activity states [*Gosling et al.*, 1995, 1997]. Furthermore, during increasing solar activity the streamer belt follows the inclination of the HCS with respect to the solar equator and covers a larger heliocentric latitude range. The result is that the width of the F/S-regions increases significantly in heliolatitude. The region of alternating wind streams in Figure 2.19(a) therefore broadens significantly with solar activity, until all heliolatitudes are covered at solar maximum in Figure 2.19(b). When the PCH disappears near solar maximum, fast wind streams still emanate from a large number of CHs which are distributed all over the solar surface.

In Figure 2.21(b) a latitude range exists around the solar equator where the transition from the fast to the slow wind (F/S), and vice versa, occurs twice within a solar rotation, i.e. in a period of ~ 13 days. This latitude range is denoted by F/S(13). Below and above this region, F/S occurs only once per rotation and is therefore denoted by F/S (26). These large-amplitude, well-defined ~ 26-day waves are clearly visible in Figure 2.19(b). An occurrence of a ~ 13-day variation may be present between ~ 20° – 30° on both sides of the solar equator. However, the 13-day pattern, which is expected in the whole equatorial region, is largely modified by asymmetries and transients at the sun. *Jokipii and Kóta* [1995] predicted the quasi-periodic 13-day and 26-day variations of the solar wind speed long before the second FLS by using their three-dimensional numerical simulation of the solar wind.

Since the number of active regions increases with solar activity, the number of slow wind streams increases accordingly and the streamer belt broadens around the HCS. It is known that the number of CHs at all latitudes also increases with solar activity [e.g. *Belenko,* 2001]. This property contributes to the fluctuation of the wind streams in the S- and F/S-regions.

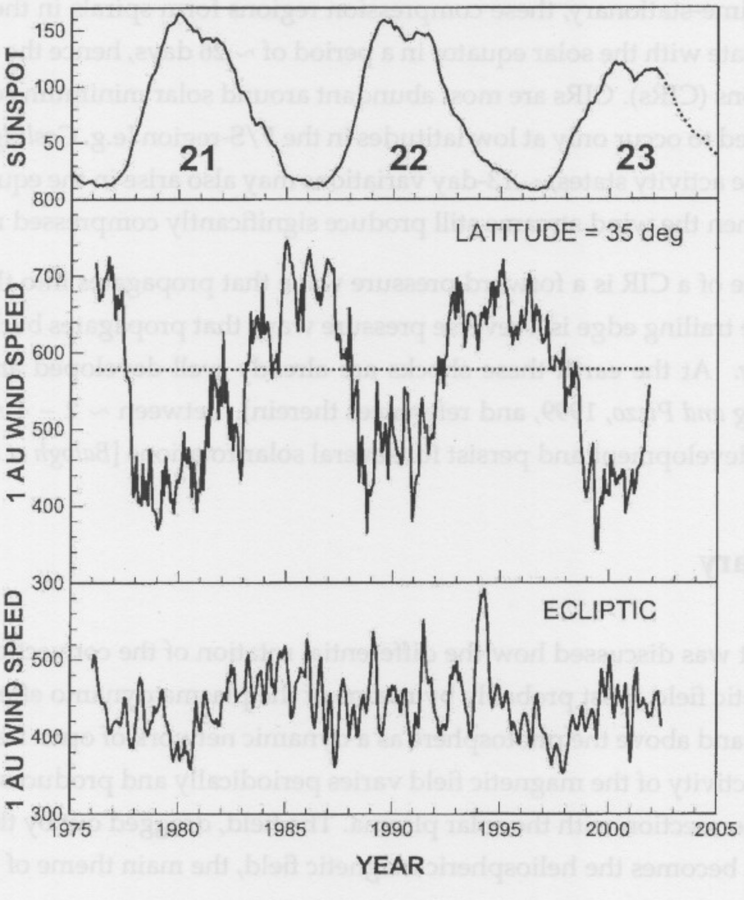

Figure 2.22: Solar cycle dependence of the 1 AU wind speed at 35° latitude (center) and in the ecliptic (bottom) for the last ~ 3 solar activity cycles according to the model of *Whang et al.* [2003]. Also shown are the corresponding sunspot numbers.

Wang and Sheeley [1990] constructed an empirical model to calculate the solar wind speed at 1 AU as function of latitude and longitude from the observed photospheric magnetic field.

This model was extended by *Whang et al.* [2003] to simulate the wind speed beyond 10 AU at all latitudes and solar activity periods. A simulation of the solar cycle dependence of the 1 AU wind speed at 35° latitude and in the ecliptic for the last ~ 3 solar activity cycles is shown in Figure 2.22. The corresponding sunspot numbers are shown to illustrate the inverse correlation of the wind speed with the solar activity. The wind speed shows a decrease of ~ 40% at 35° latitude and ~ 20% in the ecliptic from solar minimum to maximum activity. The results in the ecliptic are consistent with the observed speeds at the earth [*Gazis et al.*, 1994].

2.6.3 Co-Rotating Interaction Regions

From Figure 2.21 it is evident that the combination of the rigidly rotating SS and the radial outflow of the solar wind causes solar wind flows of different speeds to become radially aligned. Compressive interaction regions are then produced where high speed streams run into slower plasma ahead [e.g. *Gosling and Pizzo*, 1999]. When the flow pattern emanating from the sun is approximately time-stationary, these compression regions form spirals in the solar equatorial plane that co-rotate with the solar equator in a period of ~ 26 days, hence the name co-rotating interaction regions (CIRs). CIRs are most abundant around solar minimum conditions and are therefore expected to occur only at low latitudes in the F/S-region [e.g. *Gosling and Pizzo*, 1999]. During moderate activity states, ~ 13-day variations may also arise in the equatorial plane (see Section 2.6.2) when the wind streams still produce significantly compressed regions.

The leading edge of a CIR is a forward pressure wave that propagates into the slower plasma ahead, while the trailing edge is a reverse pressure wave that propagates back into the trailing high speed flow. At the earth these shocks are already well-developed and are frequently detected [*Gosling and Pizzo*, 1999, and references therein]. Between ~ 2 – 4 AU the structures reach their full development and persist for several solar rotations [*Balogh et al.*, 1999].

2.7 Summary

In this chapter it was discussed how the differential rotation of the convection zone generates the solar magnetic field most probably by means of the plasma dynamo effect. This magnetic field features in and above the photosphere as a dynamic network of open field lines and coronal loops. The activity of the magnetic field varies periodically and produces many interesting phenomena in connection with the solar plasma. The field, dragged out by the solar wind into the heliosphere, becomes the heliospheric magnetic field, the main theme of the next chapter.

Chapter 3

The Heliospheric Magnetic Field: Structure and Properties

3.1 Introduction

The coronal magnetic field (CMF) in the outer corona is dragged outward by the radially expanding solar wind to the outer regions of the heliosphere, consequently becoming the heliospheric magnetic field (HMF). This chapter is devoted to the description of the structure and properties of this field. Firstly, it is described how the potential field source surface (PFSS) model, which was introduced in the previous chapter, connects the CMF and HMF. Then the Parker spiral, the most simple representation of the HMF, is derived. Being part of the HMF, the structure of the heliospheric current sheet (HCS) is also deduced. The significance of magnetic field diffusion for the HMF is introduced and different proposed representations of the HMF are discussed.

3.2 Connecting the Coronal and Heliospheric Magnetic Fields

In Section 2.5, the current-free CMF model that describes the magnetic field from the photosphere to the SS in the mid-corona is introduced. This PFSS model was developed by *Schatten et al.* [1969] to connect the potential (dipolar) field model near the photosphere to the newly proposed HMF model of *Parker* [1958]. The HMF is completely governed by currents and is assumed to originate in the high corona and extend to the outer regions of the heliosphere. The current-free description of the potential field is therefore inapplicable to the HMF. This is solved both mathematically and physically by defining a surface that separates the CMF and HMF. This surface is called the source surface (SS), because it serves as a source of currents to the HMF. Below the SS no currents are present; on the SS and beyond, large currents can restrict the magnetic field in order to be radial. The HMF and HCS are then assumed to originate at the SS. *Schatten et al.* [1969] remark that the sudden appearance of currents on the SS does not affect the global field structure.

The radius of the SS that is usually assumed, depends on the purpose of the field model, i.e. the type of features that are to be described. When a SS radius, r_{SS}, of $\sim 1.5 - 2.5\ r_\odot$ is used, CMF and HMF magnitudes can be simulated reasonably accurately. With larger values, a more accurate, qualitative description of the CMF configuration is obtained, e.g. CH sizes and locations [*Balogh et al.*, 1999, and references therein]. Currently, the most models are based on the model of *Wang and Sheeley* [1992] or *Hoeksema et al.* [1996], who commonly use a radius of $2.5\ r_\odot$. Recently, Hoeksema and co-workers introduced a model with $r_{SS} = 3.25\ r_\odot$. These are all CMF models, models which depend significantly on the value of r_{SS}. On the opposite side of the SS, the large-scale HMF models are usually employed at radial distances $r \gg r_\odot, r_{SS}$ and therefore $r_{SS} \sim r_\odot$ is often assumed [see, e.g., *Kóta and Jokipii*, 1983]. However, the HMF model of *Fisk* [1996] and *Fisk et al.* [1999a], based on the PFSS model, depends qualitatively on the SS. This model only requires a source surface radius well below the Alfvén radius of $\sim 10\ r_\odot$. The model of *Schwadron* [2002], a generalised Fisk HMF model, employs the value $r_{SS} = 10\ r_\odot$.

The PFSS model not only have difficulties to decribe some features in the CMF that develop as the result of currents, but also has some implications for the HMF. *Fisk* [2005] remarks that both diffusion of the field lines and the differential rotation of the photospheric footpoints create systematic, large-scale motions of the CMF lines, adding transverse components to the HMF. This result is inconsistent with the assumption of radial field lines on the SS. *Fisk* [2005] therefore introduced a new model in which a diffusion-convection equation solves the deficiencies of the PFSS model. His model also includes the effect of reconnection between open lines and coronal loops, an important process which cannot be described effectively by the PFSS model.

The Parker HMF, which was developed prior to the PFSS model, only depends on the field condition on the SS. More recently, *Smith and Bieber* [1991] and *Jokipii and Kóta* [1989] modified the Parker HMF to account for some observed effects in the CMF (see Section 3.6). The next generation of HMF models started with the proposed model of *Fisk* [1996], who derived an HMF model using some properties of the current-free CMF in the PFSS model.

3.3 The Parker Heliospheric Magnetic Field

The simplest representation of the HMF traces out an Archimedian spiral: The field lines, which extend radially into the outer heliosphere beyond a certain surface, are wound up by their footpoints being rooted in this surface. This spiral structure is analogous to the water pattern from a rotating garden sprinkler. Parker deduced this field structure in 1958 and it is therefore also known as the Parker spiral. Note that this spiral structure has the same shape in both the co-rotating and time-stationary frames. This follows as a consequence of the special theory of relativity, since the plasma wind speed is much less than the speed of light in the heliosphere [*Smith*, 2000].

The Parker HMF can be derived by considering a simple geometry in which the rotation axis, $\mathbf{\Omega}$, and magnetic axis, $\mathbf{M}$, are aligned, so that heliographic polar coordinates can be used. Consider the spherical symmetric outflow of the solar wind from the solar corona. Suppose that the flow velocity V_{sw} is constant beyond a certain surface. This condition is satisfied at the SS. Assume further that the plasma rotates approximately like a solid body at the rate Ω from the inner corona out to the Alfvén radius (see Section 2.5.5) [cf. references in *Bird and Edenhofer*, 1990; *Choudhuri*, 1998]. In the frame of reference co-rotating rigidly at this rate, the flow velocity beyond the SS in heliocentric spherical coordinates (r, θ, ϕ) is given by

$$\mathbf{V} = V_{sw}\mathbf{e}_r - \Omega(r - r_{SS})\sin\theta\,\mathbf{e}_\phi. \tag{3.1}$$

Note that $\mathbf{V}$ has only a constant, radial component on the SS where $r = r_{SS}$. At the SS the solar wind plasma is highly ionised and the HMF is frozen into it. From Equation (3.1) and the frozen-in condition, $\mathbf{B} \times \mathbf{V} = 0$, it follows that $B_\theta = 0$ and B_ϕ is independent of ϕ. By using the divergence-free property of the field, its radial component can easily be obtained:

$$\begin{aligned} \nabla \cdot \mathbf{B} &= \frac{1}{r^2}\frac{\partial}{\partial r}\left(r^2 B_r\right) + \frac{1}{r\sin\theta}\frac{\partial}{\partial\theta}\left(\sin\theta B_\theta\right) + \frac{1}{r\sin\theta}\frac{\partial B_\phi}{\partial\phi} &&= 0 \\ \Longrightarrow &\quad \frac{1}{r^2}\frac{\partial}{\partial r}\left(r^2 B_r\right) &&= 0 \\ \Longrightarrow &\quad r^2 B_r &&= \mathit{constant}. \end{aligned} \tag{3.2}$$

It is the most convenient to normalise the HMF in terms of the average magnitude of the field at the earth, $B_e = B(r_e)$, where $r_e = 1$ AU is the radial distance between the sun and the earth. At solar minimum $B_e \sim 5$ nT; at higher activity B_e can reach values larger than 10 nT [e.g. *Caballero-Lopez et al.*, 2004]. Now, from Equation (3.2) it follows that

$$B_r(r_e)r_e^2 = B_r(r)r^2 \tag{3.3}$$

and hence

$$B_r = A\left(\frac{r_e}{r}\right)^2, \tag{3.4}$$

where $|A| = |B_r(r_e)|$ is the radial magnetic field strength at the earth. The sign of A corresponds to the polarity of the magnetic field: during a positive solar cycle, $A > 0$ and the field is directed outward in the northern hemisphere and inward in the southern hemisphere; during the $A < 0$ epoch the field direction is reversed.

In order to derive the transverse components of $\mathbf{B}$, the frozen-in condition, $\mathbf{B} \times \mathbf{V} = 0$, is used, from which it follows that

$$\frac{B_\theta}{B_r} = \frac{V_\theta}{V_r} \quad \Longrightarrow \quad B_\theta = B_r\frac{V_\theta}{V_r} = 0, \tag{3.5}$$

and

$$\frac{B_r}{B_\phi} = \frac{V_r}{V_\phi} \quad \Longrightarrow \quad B_\phi = B_r\frac{V_\phi}{V_r} = -B_r\frac{\Omega\,(r - r_{SS})}{V_{sw}}\sin\theta. \tag{3.6}$$

The angle between the field direction and the radial direction is known as the (Parker) spiral angle, the winding angle or the garden hose angle, ψ, i.e.

$$\tan\psi \equiv \frac{B_\phi}{B_r} = \frac{\Omega\,(r - r_{SS})}{V_{sw}}\sin\theta \tag{3.7}$$

at a radius r and polar angle θ. The spiral angle is an indication of how tightly wound the HMF lines are. Since B_r decreases with $1/r^2$, but B_ϕ decreases only with $1/r$, the field gets accordingly more tightly wound at larger distances. The spiral angle has a value of ~ 45° at the earth and increases with radial distance to almost 90° beyond 10 AU in the equatorial plane. When the field is directed away from the sun, $0° < \psi < 90°$, and when it is directed towards the sun, $180° < \psi < 270°$.

The well-known expression for the Parker spiral, normalised at earth, is then given by

$$\begin{aligned}\mathbf{B} &= A\left(\frac{r_e}{r}\right)^2\left[\mathbf{e}_r - \frac{\Omega\,(r - r_{SS})}{V_{sw}}\sin\theta\,\mathbf{e}_\phi\right]\\ &= A\left(\frac{r_e}{r}\right)^2\left(\mathbf{e}_r - \tan\psi\,\mathbf{e}_\phi\right),\end{aligned} \tag{3.8}$$

where $\mathbf{e}_r$ and $\mathbf{e}_\phi$ are the unit vector components of the field in the radial and azimuthal directions, respectively, and with $\tan\psi$ given by Equation (3.7).

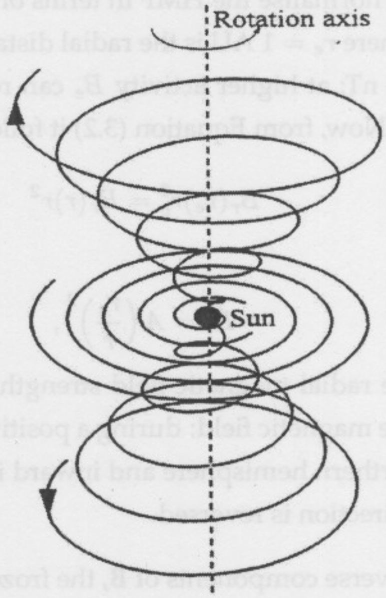

Figure 3.1: An idealised, three-dimensional representation of the Parker spiral, shown for the field lines which originate at the solar equator and at northern and southern latitudes of 45° [from *Hattingh*, 1998].

An idealised, three-dimensional representation of the Parker spiral is illustrated in Figure 3.1 [*Hattingh*, 1998]. The field lines originating at the solar equator and at northern and southern latitudes of 45° in both hemispheres are shown. Note that the spirals rotate clockwise.

3.4 Modelling the Heliospheric Current Sheet

The HCS is the extension of the magnetic equator (or neutral line) from the SS to the outer regions of the heliosphere, separating the two hemispheres with opposite magnetic polarities. Being part of the HMF, it is frozen into the solar wind and propagates radially outward with the wind. Even at solar minimum there is a small offset between **Ω** and **M** (see Fig. 2.16). As the sun rotates, the HCS also rotates, resulting in a wavy or warped structure. Assuming a radial solar wind velocity with a constant magnitude at the SS, an expression for the HCS originating at the magnetic equator can easily be derived. Firstly, it is evident from the solar rotation that the HCS varies sinusoidally with azimuthal angle. It may then be inferred that the inclined magnetic equator results in an HCS that varies sinusoidally with radial distance as well. This is indeed reasonable for periods of low solar activity. However, when the angle between **M** and **Ω** approaches 90°, the magnetic equator becomes almost aligned with **Ω** and the amplitude of the wavy HCS approaches infinity, contradicting the sinusoidal prediction. The actual variation is described by a tangent function, as will now be derived using Figure 3.2 [*R.A. Burger, private communication*].

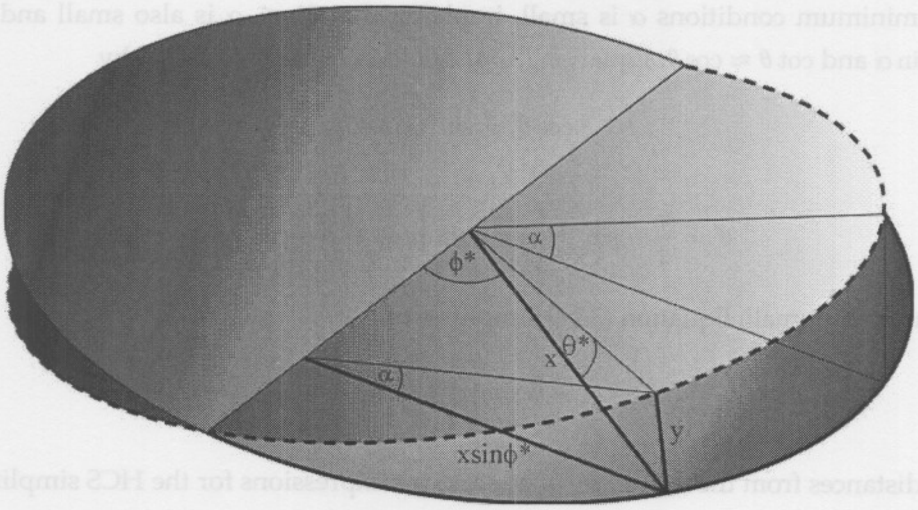

Figure 3.2: A plane through the solar magnetic equator (dashed circle), tilted at an angle α relative to the rotational equator (solid cirle). The HCS originates in the tilted plane and rotates in the equatorial plane. From this configuration, it is simple to derive the expression for the HCS [*Burger, private communication*].

In Figure 3.2 the solid circle is in the rotational equator of the sun. The dashed circle denotes the position of the magnetic equator on the SS, tilted with an angle α relative to the equatorial plane. Consider the triangle on the tilted plane, being projected onto the equatorial plane, and the coordinates that are shown. The angles ϕ^* and θ^* denote the azimuthal angle and latitude at (x,y) in the co-rotating system, respectively. From this figure it follows that

$$\tan\alpha = \frac{y}{x\sin\phi^*} \Longrightarrow \frac{y}{x} = \tan\alpha\sin\phi^* . \tag{3.9}$$

But

$$\frac{y}{x} = \tan\theta^*. \tag{3.10}$$

Therefore,

$$\tan\theta^* = \tan\alpha\sin\phi^*. \tag{3.11}$$

The angle ϕ^* is measured in a system co-rotating with the SS; for a fixed observer's frame, $\phi^* = \phi + \frac{\Omega(r-r_{SS})}{V_{sw}}$. The general expression for the HCS is then given by

$$\theta^* = \tan^{-1}\left\{\tan\alpha\sin\left[\phi + \frac{\Omega\,(r-r_{SS})}{V_{sw}}\right]\right\} \tag{3.12}$$

or, in terms of the polar angle $\theta' = \frac{\pi}{2} - \theta^*$,

$$\theta' = \frac{\pi}{2} - \tan^{-1}\left\{\tan\alpha\sin\left[\phi + \frac{\Omega\,(r-r_{SS})}{V_{sw}}\right]\right\}, \tag{3.13}$$

or, in a compact form,

$$\cot\theta' = \tan\alpha\sin\phi^*, \tag{3.14}$$

in agreement with *Kóta and Jokipii* [1983], who assumed an HCS which originates at the photosphere.

At solar minimum conditions α is small, implying that $\theta^* \leq \alpha$ is also small and therefore $\tan\alpha \approx \sin\alpha$ and $\cot\theta \approx \cos\theta$. Equation (3.14) can then be approximated by

$$\cos\theta' = \sin\alpha\sin\phi^*, \tag{3.15}$$

or

$$\theta' = \frac{\pi}{2} - \sin^{-1}\left\{\sin\alpha\sin\left[\phi + \frac{\Omega\,(r-r_{SS})}{V_{sw}}\right]\right\}. \tag{3.16}$$

If α is reasonably small, Equation (3.16) simplifies to

$$\theta' = \frac{\pi}{2} - \alpha\sin\left[\phi + \frac{\Omega\,(r-r_{SS})}{V_{sw}}\right]. \tag{3.17}$$

At large distances from the sun, $r \gg r_\odot, r_{SS}$ and the expressions for the HCS simplify to

$$\theta' = \frac{\pi}{2} - \alpha\sin\left[\phi + \frac{\Omega r}{V_{sw}}\right]. \tag{3.18}$$

The HCS structure is commonly referred to as the 'ballerina skirt'. A three-dimensional schematic representation of Equation (3.18) for $\alpha = 30°$ and to a radial distance of 10 AU is shown in Figure 3.3. Physically, dynamic processes in the solar wind severely distort the shape of the HCS and its structure is therefore considerably more complex than illustrated here [see, e.g., *Crooker et al.*, 1993].

It is usually assumed that the HMF is an approximate dipole field [e.g. *Gosling and Pizzo*, 1999; *Smith et al.*, 2003]. The simplest HMF configuration then consists of a single HCS with open flux of opposite polarity on either side of it. This is a reasonable approximation near solar

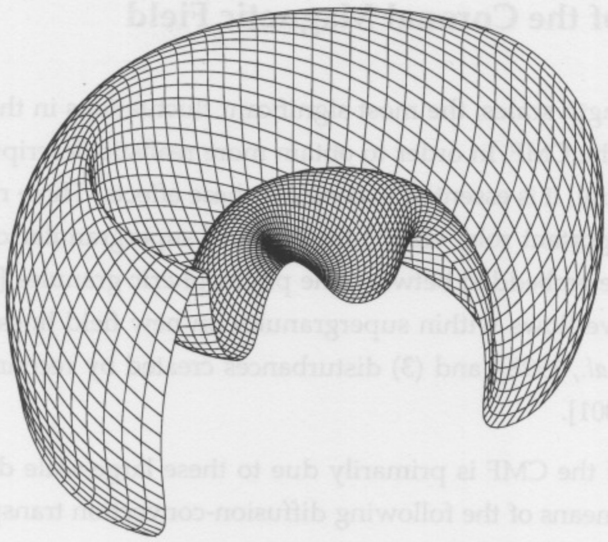

Figure 3.3: A schematic representation of the HCS with a tilt angle of 30° drawn up to a radial distance of 10 AU. A sector has been cut away to emphasise the wavy structure.

minimum conditions. However, near solar maximum, the large number of perturbations in the CMF, which result due to features such as flares and prominences, is reflected in the HMF. The higher order terms in the spherical harmonic expansion of the HMF then become significant and the dipole field is distorted by quadrupole moments, which can give rise to multiple HCSs [see, e.g., *Crooker et al.*, 1993; *Kóta and Jokipii*, 2001a]. Furthermore, at high solar activity, CHs of different polarities are distributed to high latitudes in both hemispheres. This reflects the large degree of waviness of the magnetic equator on the photosphere and may even result in a sectorial global structure where the sectors are divided by multiple current sheets [e.g. *Kóta and Jokipii*, 2001a, b]. During the most active state of the sun, **M** rotates through the heliographic equator and the field reverses polarity. During this period the HCS covers all heliolatitudes.

According to the mathematical definition of the HCS, the transition from positive to negative polarity across the sheet is abrupt. The polarity change can then be included in the magnetic field by a step function which gives the sign of the field. This step function equals +1 when $\theta > \theta'$ and -1 when $\theta < \theta'$. Such a step function is given by $1 - 2H(\theta - \theta')$, where $H(\theta - \theta')$ is the Heaviside unit step function given by

$$H(\theta - \theta') = \begin{cases} 0, & \theta < \theta'; \\ 1, & \theta > \theta'. \end{cases} \tag{3.19}$$

A bipolar field is then described by

$$\mathbf{B} = \mathbf{B}_m \left[1 - 2H(\theta - \theta')\right], \tag{3.20}$$

where $\mathbf{B}_m$ is the magnetic field in the northern hemisphere, such as the Parker field in Equation (3.8).

3.5 Diffusion of the Coronal Magnetic Field

On large time and length scales, the most significant fluctuations in the HMF originate from diffusive motions of the CMF. In order to obtain more realistic descriptions of the HMF than the normal Parker spiral, it is essential to consider these effects. Three random-walk diffusion processes play an important role, viz. (1) the effect of supergranular convection currents on the footpoints that are embedded between the photospheric granules [*Leighton*, 1964], (2) the effect of the convective flows within supergranules on new field lines that emerge from the granules [*Schrijver et al.*, 1998], and (3) disturbances created by reconnecting field lines [e.g. *Fisk and Schwadron*, 2001].

The total diffusion of the CMF is primarily due to these large-scale diffusive processes and can be described by means of the following diffusion-convection transport equation [*Fisk and Schwadron*, 2001, and references therein]:

$$\frac{\partial B_o}{\partial t} = \nabla^2(\kappa B_o) - \nabla \cdot (\mathbf{u} B_o), \tag{3.21}$$

where B_o is the open magnetic field strength, κ the diffusion coefficient and $\mathbf{u}$ the transverse convective velocity along the solar surface due to the combination of all convective motions.

Diffusion over a characteristic length δh in a characteristic time δt is expressed by

$$\kappa = \frac{(\delta h)^2}{2\delta t} \tag{3.22}$$

and the transverse speed of the field lines is

$$u_\perp \sim \frac{\delta h}{\delta t}. \tag{3.23}$$

3.5.1 Supergranulation

The convection currents in the convection zone and photosphere cause the systematic differential rotation of the photospheric granules as described in Section 2.3, as well as random supergranular diffusion, also known as supergranulation. Both processes are fairly independent of solar activity conditions. Moreover, supergranulation occurs at all locations on the photosphere, except inside sunspots, where granules cease to exist (see Fig. 2.11).

Magnetic field lines are concentrated in the network lanes between supergranules [*Schrijver et al.*, 1998]. These field lines reorientate themselves when the neighbouring supergranules submerge and new supergranules fill these positions due to supergranulation. This happens on a timescale of $\sim 1-2$ days, the typical lifetime of a supergranule. To calculate the diffusion coefficient, an average value of $\delta t = 1.5$ days can be used. The characteristic diffusion length δh is at most the size of a supergranule, typically $\sim 3 \times 10^4$ km. However, during the period when an old supergranule submerges and a new one emerges, the field line footpoints are expected to travel only a fraction of the scale size of a supergranule, say $\delta h \sim 10^4$ km. Using

Equations (3.22) and (3.23), the resulting values for the diffusion coefficient and transverse diffusive speed are $\kappa \sim 400$ km^2/s and $u_\perp \sim 0.077$ km/s, respectively.

3.5.2 The Emergence of New Magnetic Flux

Fisk et al. [1999c] proposed a diffusion process that is connected to supergranulation, but dominates the actual supergranular diffusion. The footpoints of new magnetic loops that have emerged from the centre of supergranules move with the usual convective flow inside the supergranules to the edges where field lines are concentrated [*Schrijver et al.*, 1998]. When the two loop footpoints approach the flux concentrations at the edges of a supergranule, magnetic tension is increased. This tension is released when the loop ends reconnect with open lines, a process which is entirely random. The characteristic scale of diffusion, δh, is the distance each loop footpoint travels from the location of emergence to the edge of the supergranule. The upper limit for δh is the characteristic size of a supergranule, typically 3×10^4 km. The time during which flux concentrations are observed to change significantly is $\delta t \sim 1.5$ days [*Schrijver et al.*, 1998], coincidently the typical lifetime of a supergranule. From Equations (3.22) and (3.23) the values for the diffusion coefficient and transverse diffusive speed are $\kappa \sim 3500$ km^2/s and $u_\perp \sim 0.23$ km/s, respectively.

3.5.3 Reconnective Diffusion

The most frequent type of reconnection occurs between open and closed field lines. For this diffusion process, *Fisk and Schwadron* [2001] define $\delta h \sim 2 \times 10^5$ km to be the average coronal loop height and $\delta t \sim 38$ hr the characteristic reconnection time. This gives the values $\kappa \sim 1.4 \times 10^5$ km^2/s and $u_\perp \sim 1.4$ km/s. The scale size for supergranulation is at most the size of a single supergranule, whereas reconnection has a scale size of several supergranules and therefore results in more rapid diffusion.

Fisk [2005] altered Equation (3.22) slightly to describe the diffusion resulting from the reconnection between open and closed field lines. The new expression is given by

$$\kappa = \frac{\overline{h}^2}{4\tau_c}. \tag{3.24}$$

Here, $\overline{h} \sim 10^5$ km represents the mean separation of loop footpoints and $1/\tau_c \sim 1/\delta t \sim 1/(38\,\mathrm{hr})$ the 'collision' frequency between open field lines and coronal loops. The additional factor of 2 in Equation (3.24), as opposed to Equation (3.22), arises because a field line can reconnect with any side of a coronal loop, depending on the orientation of the loop. In contrast, convective currents only flow in one direction. More reasonable values for κ and $u_\perp$ are then $\sim 2 \times 10^4$ km^2/s and ~ 0.7 km/s, respectively.

These values apply to coronal loops, which are located primarily on the outside of CHs. Inside fully developed CHs, only relatively small loops are present (see Section 2.5.1) and this type of reconnection therefore occurs infrequently. Instead, the small loops result from new flux that has emerged from beneath the photosphere and the diffusion of these loops is related to the convection in the photosphere, which is discussed in Section 3.5.2.

3.5.4 Total Diffusion

The diffusion that results from the emergence of new magnetic flux, as well as reconnective diffusion, is expected to increase both toward the equator and with solar activity (see Section 2.5.1). However, due to the presence of convection streams at all latitudes, new flux also emerges from the photosphere in the polar regions. This means that the two convection-related diffusion processes, supergranulation and new flux emergence, occur frequently inside PCHs. However, in large regions inside these holes, the systematic motion of the photosphere's differential rotation (see Section 2.3) dominates the diffusion due to these processes. This is discussed in Chapter 5. Outside PCHs all diffusion processes are present, but it can be inferred from the calculations provided in this section that reconnective diffusion is the principal diffusion process.

The three types of diffusion discussed above only apply to small scale sizes compared with the solar radius. The diffusion speeds resulting from the diffusion related to convection are only valid within the scale size of a few supergranules. On larger scales the random behaviour of these diffusive processes gives rise to significantly smaller average speeds. Similarly, the values obtained for the reconnective diffusion speed are only local to the scale size of a few coronal loops. *Fisk et al.* [1999a] remark that the period for small-scale reconnective diffusion over a distance of $\sim 1\ r_\odot$ is $10 - 20$ solar rotations and therefore much longer than the nearly steady differential rotation. Globally, the total diffusion is therefore significantly less than on smaller scales. *Fisk* [2005] calculates the long-term global effect of the combination of all the diffusion processes. For this purpose, κ is expressed in terms of the rate of emergence of new magnetic flux on the photosphere and the values $\kappa \sim 600\,\mathrm{km}^2/\mathrm{s}$ and $u_\perp \sim 0.005$ km/s are obtained. These values are consistent with the meridional flow values obtained by *Wang et al.* [2000] in their simulation of the sunspot cycle. This meridional flow is probably a result of the solar dynamo effect. The photospheric granules diffuse gradually to the solar poles within a timescale of ~ 2.2 years [*Wang et al.*, 1989].

3.5.5 Numerical Simulation of Magnetic Field Diffusion

Giacalone and Jokipii [2004] simulated the effect of supergranulation, or a process connected to it, which is transferred from the CMF to the HMF. By means of their numerical simulation, a value for κ in the range between $1500\,\mathrm{km}^2/\mathrm{s}$ and $1920\,\mathrm{km}^2/\mathrm{s}$ was found. This value is a factor of ~ 2 smaller than the value obtained by *Fisk and Schwadron* [2001]. With the use of a power spectrum, the rms transverse speed of the photospheric footpoints was found to be ~ 0.6 km/s, a factor of about 2.6 larger than the value of *Fisk and Schwadron* [2001].

Giacalone and Jokipii [2004] remark that the discrepancies between their values and those of *Fisk and Schwadron* [2001] are probably due to two processes that were not included in their model, viz. transverse flows with non-zero divergence, and magnetic reconnection. However, the former process, meridional flow, is very slow and the resulting diffusion coefficient is negligible on the time-scales of supergranulation. Furthermore, magnetic reconnection was considered as a separate diffusion process by *Fisk and Schwadron* [2001] and therefore cannot be compared with supergranular diffusion. Since reconnective diffusion is a vital component of the CMF, its effect is effectively transferred to the HMF. The inclusion of this process in the HMF model of *Giacalone and Jokipii* [2004] will indeed present a more realistic representation of the total diffusion of the field.

Giacalone and Jokipii [2004] report that the transverse variations in the HMF are in agreement with observations from *Ulysses*, even though significant superradial expansion of the PCH field lines from the photosphere to the SS was not included in their model. If it was, the calculated variance of the HMF along the *Ulysses* trajectory would have been significantly larger than the values which were obtained from the *Ulysses* observations. *Giacalone and Jokipii* [2004] then suggest that superradial expansion does not play a significant role. However, the omission of superradial expansion probably explains the discrepancies between the values in the two papers (*Fisk and Schwadron* [2001] and *Giacalone and Jokipii* [2004]). The values calculated by *Fisk and Schwadron* [2001], who assume a large superradial expansion in PCHs near solar minimum, therefore seem more realistic and will be used in what follows.

3.6 Other Heliospheric Magnetic Field Models

The Parker HMF, though introduced in 1958 as a first-order approximation of the HMF, is still widely used [see, e.g., *Parhi et al.*, 2003]. According to observations, this model is reasonable in the ecliptic plane [see, e.g., *Ness and Burlaga*, 2001, and references therein], but significant deviations over the solar poles were observed [e.g. *Forsyth et al.*, 1996]. *Smith and Bieber* [1991] and *Jokipii and Kóta* [1989] suggested such modifications of the Parker HMF even before results from *Ulysses* were obtained. Recently, more modifications and alternative HMF models were proposed. *Burger* [2005] discusses a selection of the frequently used HMF models. The purpose of this section is to present a similar overview.

3.6.1 Modifications of the Parker Field

The Jokipii-Kóta Modification

In the polar region, the rotation speed of the photosphere is largely exceeded by the diffusion speed caused by supergranulation (see Sections 2.3 and 3.5). *Jokipii and Kóta* [1989] argued that this turbulence of the photospheric footpoints creates significant transverse components of the HMF, such that both B_θ and B_ϕ decrease as 1/r, whereas B_r decreases as $1/r^2$. They therefore introduced the correction term $\delta(\theta, \phi)$, which amplifies the field strength at large radial distances in the polar region.

For a small perturbation, $\delta|A|\mathbf{e}_\theta$, of the Parker field due to the average effect of supergranulation in the photosphere, the expression for the magnitude of the HMF at large radial distances becomes

$$B = A\left(\frac{r_e}{r}\right)^2 \sqrt{1 + \tan^2\psi + \left(\frac{r\delta}{r_\odot}\right)^2}. \tag{3.25}$$

The presence of a transverse field in the polar region increases the field strength significantly in comparison with what is expected from the Parker spiral field. This is in agreement with observations from *Ulysses* near the southern pole [*Smith et al.*, 1995]. See *Langner* [2004] for an implementation of this field in a numerical modulation model.

The Moraal Modification

Moraal [1990] suggested that the whole expression for the Parker HMF can be multiplied by an arbitrary function $\Theta(\theta)$, where $\Theta = 1$ at the solar equator and increases toward the poles. This modification maintains a divergence-free magnetic field for all functions of θ. The expression for the modified Parker field is then given by

$$\mathbf{B} = A\left(\frac{r_e}{r}\right)^2 \Theta(\theta) \left[\mathbf{e}_r - \tan\psi \mathbf{e}_\phi\right]. \tag{3.26}$$

The Smith-Bieber Modification

Smith and Bieber [1991] examined HMF measurements from the period 1965 to 1987 in a distance range from 0.7 to 15.9 AU in order to test the Parker field. They found that the spiral angle, ψ, increases with about 10° from solar minimum to maximum conditions. This solar cycle dependence of ψ could not be explained with the normal Parker field. They suggested that the differential rotation of the photosphere may increase the azimuthal component of the CMF. This increase is subsequently convected to the HMF, which originates at the SS. The Parker field configuration can be corrected by adding a correction term $r\delta_{SB}$ to the azimuthal component. Note that δ_{SB} should only depend on the heliolatitude in order to maintain a divergence-free magnetic field. The resulting modified Parker field,

$$\mathbf{B} = A\left(\frac{r_e}{r}\right)^2 \left[\mathbf{e}_r + \left(r\delta_{SB} - \tan\psi\right)\mathbf{e}_\phi\right], \tag{3.27}$$

can then describe the observed overwinding at the solar poles during active periods of the sun.

The Giacalone Modification

In Section 3.5 it was discussed that diffusive motions of the CMF result in significant fluctuations in the HMF. *Giacalone* [1999] stated that these transverse motions are the consequence of

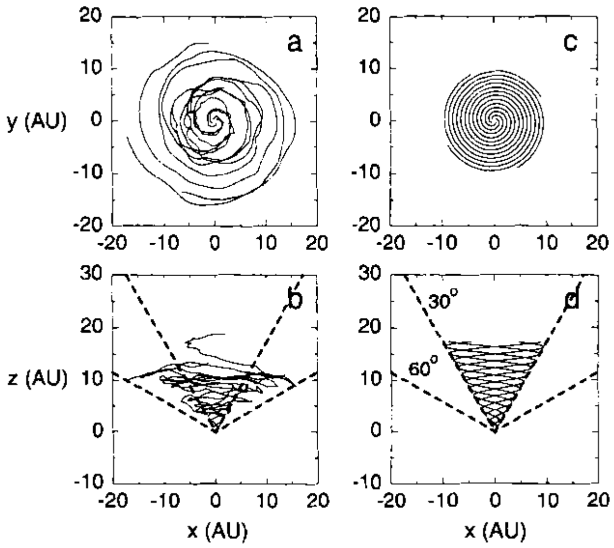

Figure 3.4: The effect of the random motion of magnetic footpoints on the HMF configuration (left panels) compared with the standard Parker spiral (right panels) as viewed from the top (upper panels) and side (lower panels) [*Giacalone*, 1999].

supergranulation in the photosphere and added random fluctuations to the meridional and azimuthal components of the velocity field of the Parker HMF. Figure 3.4 [*Giacalone*, 1999] shows a representation of such a field (left panels) in comparison with the normal Parker spiral (right panels) as viewed from the top and side, respectively.

3.6.2 The Fisk Heliospheric Magnetic Field

Fisk [1996] proposed a new structure for the HMF in the fast solar wind emanating from the PCHs at the solar poles, which is significantly different from the standard Parker spiral. He suggested that the combination of the differential rotation of the magnetic footpoints on the photosphere and the subsequent superradial expansion of these field lines results in an HMF with a meridional component, consisting of field lines that exhibit extensive excursions in heliographic latitude. The next chapter is devoted to a study of this HMF.

3.6.3 Modifications of the Fisk Field

The Schwadron Modification

Schwadron [2002] generalised the Fisk HMF to include the effect of the latitude dependence of the solar wind. Rarefaction regions are typically present in the slow wind region outside coronal holes. A strong shearing between the fast solar wind within the hole and the slow wind in these rarefaction regions continually occurs across CH boundaries. When a magnetic footpoint on the SS moves across the CH boundary into such a region, the magnetic field line becomes stretched out due to the shearing in the solar wind. The consequence is a strongly underwound magnetic field in rarefaction regions, which is supported by observations [*Murphy et al.*, 2002].

The Fisk-Parker Hybrid Field

In order to obtain an expression that describes the HMF at all latitudes, *Burger and Hitge* [2004] proposed a model which combines the Fisk field inside PCHs at mid- and high latitudes on the SS, and the Parker field at low latitudes. This HMF model is described in detail and refined in Chapter 5.

3.7 Summary

This chapter was devoted to describing some attributes of the HMF and different models representing the field. It is generally believed that significant deviations from the standard Parker field occur over the solar poles. A few modifications of this field were therefore introduced. In the next chapter it is shown that systematic motions of the CMF footpoints give rise to a completely new description of the HMF, known as the Fisk field.

Chapter 4

Fisk-Type Models of the Heliospheric Magnetic Field

4.1 Introduction

In Section 2.6.3, systematically rotating compression regions, resulting from the interaction between slow and fast wind streams, are introduced. The particles at these co-rotating interaction regions (CIRs) are accelerated and propagate with the solar wind into the outer heliosphere. In the standard Parker field these recurrent energetic particle events are expected to remain near the latitudes where the CIRs occur, which is at low latitudes during solar minimum conditions [see, e.g., *Gosling and Pizzo*, 1999]. However, during the fast latitude scan (FLS) of *Ulysses*, 26-day periodic variations of particle intensities were observed up to the highest latitudes ($\sim$ 80°S) [*Simpson et al.*, 1995; *Roelof et al.*, 1997; *Zhang*, 1997]. These particles could have originated in CIRs at low latitudes and propagated to higher latitudes by means of some as yet unknown process. Moreover, the latitudinal gradients of particle intensities from the equatorial region to high latitudes were significantly smaller than expected [*Simpson et al.*, 1996; *McKibben et al.*, 1996]. Since this phenomenon is probably connected to the recurrent variations [*Zhang*, 1997; *Burger and Hitge*, 2004], its occurrence suggests a significant flux of particles from low to high latitudes. Two mechanisms were suggested.

Kóta and Jokipii [1995] simulated the behaviour of the CIR particles and found that the co-rotating variations in the intensity can persist to quite high heliographic latitudes. This was obtained by using a Parker-type HMF, but including large cross-field diffusion of the particles, i.e. easy access in heliographic latitudes due to scattering by irregularities in the HMF.

An alternative mechanism is a magnetic field with field lines that connect low latitudes near the sun to high latitudes at regions further away. Such a model was proposed by *Fisk* [1996], hereafter called the Fisk model or Fisk field. The accelerated particles in CIRs can then in principle readily follow the magnetic field lines into the heliosphere.

The purpose of this chapter is to describe Fisk-type models in detail. The footpoint motion equations, which describe the connection between a field line's coordinates on the photosphere and source surface, are derived for two different photospheric field configurations. Thereafter the derivation of the Fisk HMF is briefly described and the resulting footpoint velocities on the source surface are illustrated. A detailed discussion about the basic assumptions in the Fisk model is given, the necessary boundary conditions are investigated and some important restrictions of the model are summarised. Finally, a Fisk-Parker hybrid model, which provides easy implementation of the Fisk model in numerical modelling codes, is discussed.

4.2 The Global Structure of the Fisk HMF

In the Fisk model of the HMF, field lines exhibit large variations in heliographic latitudes, in particular from low latitudes near the sun to high latitudes further away. Since the HMF is directed radially outward from the SS, the latitudes of the field lines will vary only if the SS footpoints move in heliographic latitudes. This can be obtained by using the two non-parallel axes $\mathbf{\Omega}$ and **M**, the (meridional) rotation and magnetic axes, respectively, and by noting that the photospheric footpoints rotate about $\mathbf{\Omega}$, while the field lines near the photosphere expand almost symmetrically about **M**.

An essential assumption in the Fisk model is the different rotation rates of **M** and the photospheric magnetic footpoints: **M** co-rotates rigidly with the solar equator, while the photospheric footpoints are anchored in the underlying photosphere and hence co-rotate differentially with it. Non-equatorial photospheric footpoints then rotate slower than **M** and therefore move in heliomagnetic coordinates. It is further assumed that the field lines near the photosphere expand non-radially and symmetrically about **M**, where the expansion rate only depends on the magnetic latitude of a particular field line according to the PFSS model. Consequently, as a photospheric footpoint rotates differentially about $\mathbf{\Omega}$, it moves in magnetic latitude and subsequently experiences a varying non-radial expansion. Furthermore, the solar wind stretches out the field lines until they become essentially radial on the SS, where the magnetic field is uniform according to the PFSS model. The footpoints, which remain at constant heliolatitudes on the photosphere, then map to varying heliolatitudes on the SS as the sun rotates, thus leading to latitudinal excursions in the heliosphere. Briefly stated, the Fisk model is the result of the combination of differentially rotating photospheric footpoints and the non-radial expansion of the field lines about a rigidly rotating magnetic axis. In Section 4.6 the implication and validity of each assumption are considered in detail.

The SS is defined to be located well below the Alfvén radius [*Fisk et al.*, 1999a], and therefore the solar plasma at the SS rotates rigidly [see, e.g., *Choudhuri*, 1998]. Since the magnetic field is frozen into this rigidly rotating solar wind which passes through the SS, the consequent field configuration is described most conveniently in the co-rotating system. Its rotation rate is the same as the solar equatorial rotation rate on the photosphere. Features at higher latitudes on the differentially rotating photosphere then appear to move clockwise in this anti-clockwise rotating system, or primarily leftward when observed from the side.

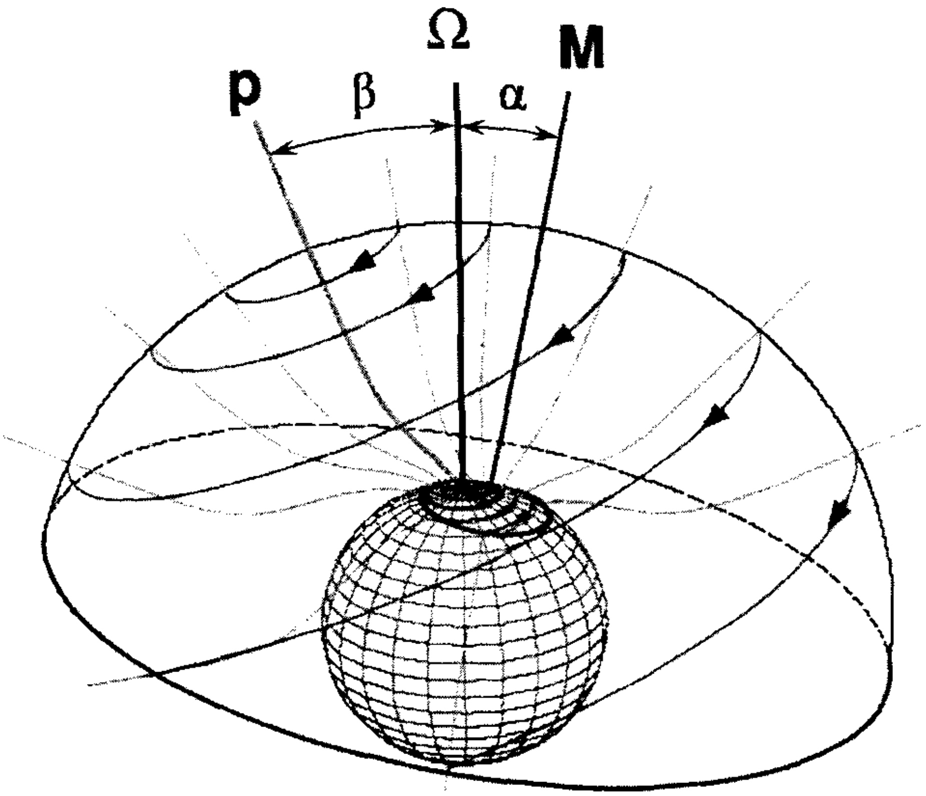

Figure 4.1: An illustration of the expansion of magnetic field lines in the northern hemisphere in a polar coronal hole (PCH), as predicted by the model of *Fisk* [1996] in a frame that co-rotates at the solar equatorial rotation rate. The expansion occurs from the photosphere to the source surface (SS), i.e. the outer surface which is penetrated only by open field lines. The PCH boundary on both the photosphere and SS is located at a constant heliomagnetic latitude. The magnetic axis, **M**, is tilted at an angle α with respect to the rotation axis, Ω. The virtual axis **p** is defined by the field line that connects to the solar pole [adapted from *Zurbuchen et al.*, 1997].

The resulting footpoint motion on the SS in this system is illustrated in Figure 4.1 [adapted from *Zurbuchen et al.*, 1997]. The inner sphere denotes the photosphere. It contains a small PCH that is symmetric about **M**. The photospheric footpoints are attached to the photosphere and trace out clockwise, circular trajectories about Ω. The magnetic field lines inside the PCH are open and expand superradially about **M** from the photosphere out to the SS. The SS footpoints trace out large trajectories about another axis, denoted by **p**, which is also offset from Ω by an angle β. The virtual axis **p** is the tangent to the field line at the SS that maps to the solar pole on the photosphere. This field line therefore experiences no differential rotation, but intersects the SS at a fixed location in the co-rotating system. As the magnetic field lines expand radially from the SS into the outer heliosphere and the SS footpoints rotate about **p**, the resulting field lines exhibit large variations in heliographic latitudes and particles can in principle propagate easily along the field lines. Note that the rotation in the southern hemisphere will be in the opposite sense.

After a first glance at the rotation of the SS footpoints, it may be concluded that the field configuration is similar to the Parker spiral, now only about the **p**-axis. However, since the observer is in the co-rotating frame, the footpoints actually rotate about two axes simultaneously, viz. **Ω** and **p**. The resulting configuration is a significant deviation from the Parker field. This is evident when considering the time-stationary system, i.e. the system in which the observer is at rest with respect to the solar centre of mass. Here, **M** rotates rigidly about **Ω**, causing the expansion directions of the field lines from the photosphere to co-rotate with **M**, and hence all the SS footpoints rotate about **Ω**. In the standard Parker field, this is the only motion of the SS footpoints. In the Fisk model, **p** is defined by a field line and therefore it co-rotates rigidly with **M** about **Ω**. Clearly, the SS footpoints rotate about **p**, which in turn rotates about **Ω**, and the field lines are wound up about these two axes simultaneously.

4.3 Derivation of the Footpoint Motion Equations

The photospheric and SS footpoints of a particular open field line are mapped in a one-to-one relation [*Fisk*, 1996]. The transformation between the coordinates of these two footpoints can be derived in a simple fashion from the divergence-free property of the magnetic field, i.e. $\nabla \cdot \mathbf{B} = 0$, as was done by e.g. *Van Niekerk* [2000].

Consider a field line that expands from the photosphere at the spherical magnetic coordinates $(r_\odot, \theta_m, \phi_m)$ to the SS at $(r_{SS}, \theta'_m, \phi'_m)$. According to the law of Gauss for magnetic fields, the net flux of this field line through any Gaussian surface is zero, i.e. $\oint \mathbf{B} \cdot d\mathbf{A} = 0$, where $d\mathbf{A}$ is a differential area vector on the Gaussian surface. This law follows from applying the Divergence Theorem to the divergence-free property of the field:

$$0 = \int_{volume} (\nabla \cdot \mathbf{B}) d\tau = \oint_{surface} \mathbf{B} \cdot d\mathbf{A}, \tag{4.1}$$

where $d\tau$ is a differential volume element enclosed by the Gaussian surface defined by two spheres with radii $r_\odot$ and r_{SS}, respectively. Then Equation (4.1) becomes

$$\oint \mathbf{B} \cdot d\mathbf{A} = \int \mathbf{B}_\odot \cdot d\mathbf{A}_\odot + \int \mathbf{B}_{SS} \cdot d\mathbf{A}_{SS} = 0, \tag{4.2}$$

where $d\mathbf{A}_\odot = -r_\odot^2 \sin\theta_m d\theta_m d\phi_m \mathbf{r}_1$ and $d\mathbf{A}_{SS} = r_{SS}^2 \sin\theta_m d\theta_m d\phi_m \, \mathbf{r}_1$, with $\mathbf{r}_1$ a unit vector in the radial direction. Equation (4.2) means that the total flux of the field from the photosphere equals the flux through the SS, independent of what occurs to the field between these two surfaces.

In order to proceed, further assumptions are necessary. The magnetic field is assumed to be uniform on the SS [see, e.g., *Balogh et al.*, 1995], and dipolar on the photosphere and in the low corona [*Fisk*, 1996]. These approximations are reasonable near solar minimum conditions (see Section 2.5). The photospheric and SS field strengths are then given by $B_r = B_0 \cos\theta_m$ and $B_{SS} = \overline{B}$, respectively, where B_0 and $\overline{B}$ are both constants. Then,

$$\int_0^{\theta_m} B_0 \cos\theta_m r_\odot^2 \sin\theta_m d\theta_m \int_0^{2\pi} d\phi_m = \int_0^{\theta'_m} \overline{B} r_{SS}^2 \sin\theta'_m d\theta'_m \int_0^{2\pi} d\phi'_m. \tag{4.3}$$

Moreover, the expansion is assumed to be symmetric about **M**, implying that the magnetic azimuthal angle of a field line remains fixed during the expansion. Therefore, $\phi_m = \phi'_m$ and

$$B_0 r_\odot^2 \int_0^{\theta_m} \cos\theta_m \sin\theta_m d\theta_m = \overline{B} r_{SS}^2 \int_0^{\theta'_m} \sin\theta'_m d\theta'_m, \tag{4.4}$$

from which it follows that

$$\frac{1}{2} B_0 r_\odot^2 \sin^2\theta_m = \overline{B} r_{SS}^2 (1 - \cos\theta'_m), \tag{4.5}$$

and hence $\sin^2\theta_m \propto 1 - \cos\theta'_m$. This relation applies to all locations inside the PCH on the photosphere and SS, and therefore also to the fixed boundary angles of the PCH on the photosphere and SS, denoted by θ_{mm} and θ'_{mm}, respectively. Consequently,

$$\frac{\sin^2\theta_m}{\sin^2\theta_{mm}} = \frac{1 - \cos\theta'_m}{1 - \cos\theta'_{mm}}, \tag{4.6}$$

or,

$$\cos\theta'_m = 1 - (1 - \cos\theta'_{mm}) \left(\frac{\sin^2\theta_m}{\sin^2\theta_{mm}} \right). \tag{4.7}$$

Knowing the polar angles of the PCH boundary on the photosphere and SS, the exact location of the SS footpoint can be derived for a field line that maps to a certain location on the photosphere inside a PCH. From Equation (4.7) an expression for the angle β can easily be obtained, since the field line originating at the solar pole maps to the **p**-axis. Therefore, $\theta_m = \alpha$, implying that $\theta'_m = \alpha + \beta$, and

$$\beta = \cos^{-1}\left[1 - (1 - \cos\theta'_{mm}) \left(\frac{\sin^2\alpha}{\sin^2\theta_{mm}} \right)\right] - \alpha. \tag{4.8}$$

The expansion of a few field lines from the PCH is illustrated schematically in Figure 4.2 [*Fisk*, 1996]. The field lines that define the PCH boundary expand from θ_{mm} to θ'_{mm}.

Fisk et al. [1999a] remark that a uniform photospheric field is more appropriate than a dipole field, because differential rotation distorts the dipolar structure. In Equation (4.5), the term $\sin^2\theta_m$ follows from the dipolar field and the term $1 - \cos\theta'_m$ from the uniform field. For a magnetic field that is uniform on both the photosphere and SS, it readily follows, similarly to the derivation above, that $1 - \cos\theta_m \propto 1 - \cos\theta'_m$. Hence,

$$\frac{1 - \cos\theta_m}{1 - \cos\theta_{mm}} = \frac{1 - \cos\theta'_m}{1 - \cos\theta'_{mm}}, \tag{4.9}$$

or,

$$\cos\theta'_m = 1 - (1 - \cos\theta'_{mm}) \left(\frac{1 - \cos\theta_m}{1 - \cos\theta_{mm}} \right). \tag{4.10}$$

The expression for β is then given by

$$\beta = \cos^{-1}\left[1 - (1 - \cos\theta'_{mm}) \left(\frac{1 - \cos\alpha}{1 - \cos\theta_{mm}} \right)\right] - \alpha. \tag{4.11}$$

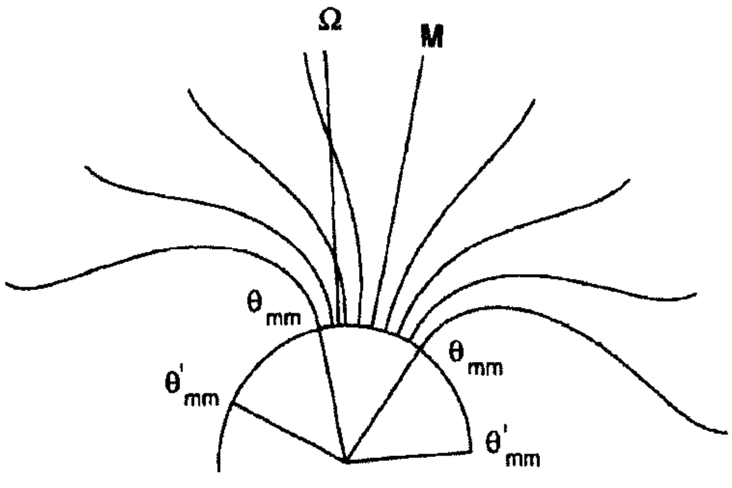

Figure 4.2: A schematic illustration of the expansion of a few field lines inside a PCH from the photosphere to the SS. Also shown are the boundary field lines that expand from the polar angle θ_{mm} on the photosphere to θ'_{mm} on the SS [*Fisk*, 1996].

Previously published results have only considered a dipolar photospheric field. Equations (4.10) and (4.11) are therefore slightly different from these published results. The fact that Equation (4.11) yields smaller values for β than Equation (4.8) follows readily:

Since the Fisk field is only a solar minimum phenomenon [*Fisk et al.*, 1999a], $\alpha < \theta_{mm}$ is an appropriate condition. Then,

$$1 + \cos\alpha > 1 + \cos\theta_{mm}. \tag{4.12}$$

Since

$$1 + \cos\alpha = \frac{1 - \cos^2\alpha}{1 - \cos\alpha} = \frac{\sin^2\alpha}{1 - \cos\alpha}, \tag{4.13}$$

and similar for the right-hand side of Equation (4.12), it follows that

$$\frac{\sin^2\alpha}{1 - \cos\alpha} > \frac{\sin^2\theta_{mm}}{1 - \cos\theta_{mm}} \quad \text{and hence} \quad \left(\frac{\sin\alpha}{\sin\theta_{mm}}\right)^2 > \frac{1 - \cos\alpha}{1 - \cos\theta_{mm}}, \tag{4.14}$$

from which follows that β in Equation (4.11) is smaller than in Equation (4.8). This result is expected from a PCH that is symmetric about **M**, as in Figure 4.2, because such a PCH originates from the magnetic polar region on the photosphere, where the field strength of a dipolar field is significantly larger than that of a uniform field. Consequently, the field lines at the pole of the dipole field expand significantly more than those at the pole of the uniform field in order to release the larger magnetic pressure.

The qualitative effect of the two different field configurations, however, does not differ significantly, and the first configuration, consisting of a dipole structure in the inner corona, is a reasonable approximation for the assumed time-independent field, especially near solar minimum conditions. In Chapter 5 it is assumed that the dipole structure persists throughout a solar activity cycle.

Since the radial propagation speed of a feature in the magnetic field is much larger than the rotation speed of the magnetic footpoints, an immediate expansion from the photosphere to the SS is assumed. The equations describing the expansion of the field lines are therefore independent of the rotation rate.

4.4 Derivation of the Fisk Heliospheric Magnetic Field

The Fisk HMF originates at the SS due to the combination of the footpoint motions on the SS and the subsequent radial expansion of the magnetic field into the outer space. First, it is assumed that the solar wind flow is radial with a constant speed according to the PFSS model. Then, by transforming the components of the wind speed to the time-stationary frame which corrects both for the equatorial rotation of the sun about $\mathbf{\Omega}$ and the differential rotation ω of the SS footpoints about $\mathbf{p}$, it can readily be shown that the meridional and azimuthal components of the footpoint velocities on the SS in the co-rotating system are [see, e.g., *Zurbuchen et al.*, 1997; *Van Niekerk*, 2000]

$$\begin{aligned} u_\theta &= r\omega \sin\beta \sin\phi \\ u_\phi &= r\omega\left[\sin\beta\cos\theta\cos\phi + \cos\beta\sin\theta\right]. \end{aligned} \tag{4.15}$$

By assuming a radial and uniform magnetic field on the SS and beyond, the radial component of the magnetic field is the same as that for the Parker field [Eq. (3.8)]. Similar to the Parker field, the transverse field components are derived from the frozen-in condition, $\mathbf{B} \times \mathbf{U} = 0$, by implementing the footpoint velocities (4.15). The resulting components in the fixed observer's frame are given by [*Zurbuchen et al.*, 1997; *Van Niekerk*, 2000]

$$\begin{aligned} B_r &= A\left(\frac{r_0}{r}\right)^2 \\ B_\theta &= B_r \frac{r\omega}{V_{sw}} \sin\beta \sin\left(\phi + \frac{\Omega(r - r_{SS})}{V_{sw}}\right) \\ B_\phi &= B_r \frac{r}{V_{sw}}\left[\omega\sin\beta\cos\theta\cos\left(\phi + \frac{\Omega(r-r_{SS})}{V_{sw}}\right) + \sin\theta(\omega\cos\beta - \Omega)\right]. \end{aligned} \tag{4.16}$$

According to the PFSS model (see Section 2.5.5) that is used to derive Equation (4.15) and therefore the Fisk field (4.16), the magnetic field is radial and constant in magnitude on the SS. This implies that the transverse components of the field in Equation (4.16) should be zero when $r = r_{SS}$, a condition which can be attained by replacing $B_r r$ with $B_r(r - r_{SS})$ in the expressions for both B_θ and B_ϕ. However, such a construction implies that the corresponding velocity field reduces to zero on the SS, resulting in the normal Parker spiral [Eq. (3.8)]. *Fisk* [2005] remarks that the differential rotation of the photospheric footpoints causes transverse field components on the SS and beyond (see Section 2.5.5). The PFSS model is therefore only valid to describe the immediate expansion from the photosphere to the SS and therefore the field structure at a given instant.

Figure 4.3 [*Fisk et al.*, 1999a] compares the global structure of the Fisk field with that of the Parker field. Both configurations are shown for a co-rotating frame and describe the field lines that originate at a latitude of 70° on the SS and which extend out to $\sim$ 20 AU in the heliosphere. The bottom panel illustrates the normal Parker spiral in which the magnetic footpoint rotation is only about $\mathbf{\Omega}$. The top panel includes footpoint motion in the Fisk model and shows the large latitudinal excursions of the field.

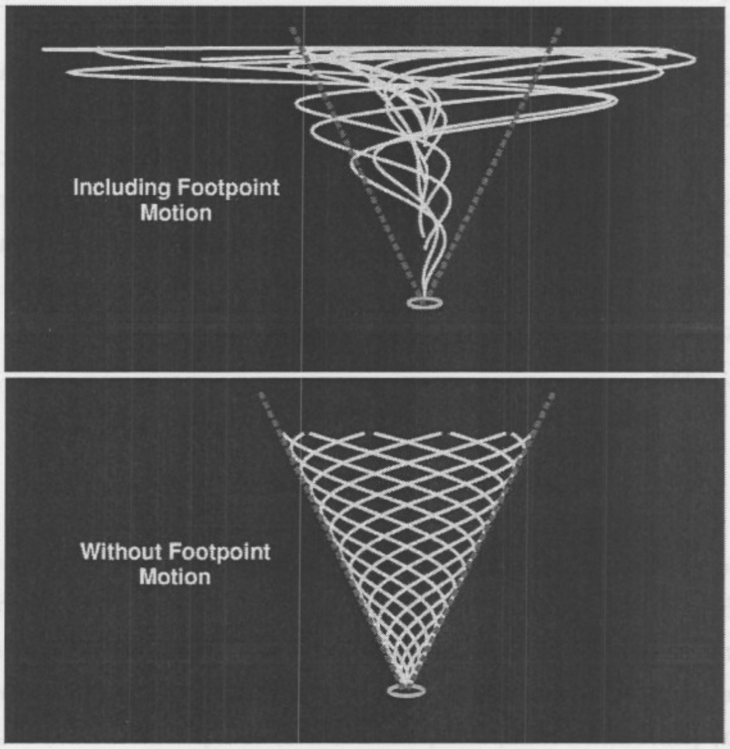

Figure 4.3: The expected configuration of the heliospheric magnetic field in the Fisk model, in which footpoint motion is included (top), and in the Parker field, in which there is no footpoint motion (bottom). All field lines shown originate at a northern latitude of 70° in the photosphere. [*Fisk et al.*, 1999a]

4.5 Footpoint Velocities in the Fisk Model

The propagation speed of the footpoints on the SS can easily be calculated from the velocity field in Equation (4.15). Figure 4.4 shows a three-dimensional representation of this speed as function of the heliographic polar angle θ and azimuthal angle ϕ. Similar to *Fisk* [1996], $\beta = 30°$ is assumed. For convenience, the PCH boundary is assumed at the constant heliographic polar angle $\theta = 70°$ on the SS. Furthermore, a SS radius of $r_{SS} = 10\ r_{\odot}$ and a constant differential rotation rate of $\omega = \Omega/4$ are used. The footpoint located at the $\mathbf{p}$-axis at $\theta = 30°$ and $\phi = 180°$ is stationary. Evidently from the variation in ϕ, the speed varies in a 26-day period as the sun rotates. A maximum speed of $\sim$ 5.5 km/s is attained at the PCH boundary.

From the footpoint motion equation (4.7), the exact location of the SS footpoint, corresponding

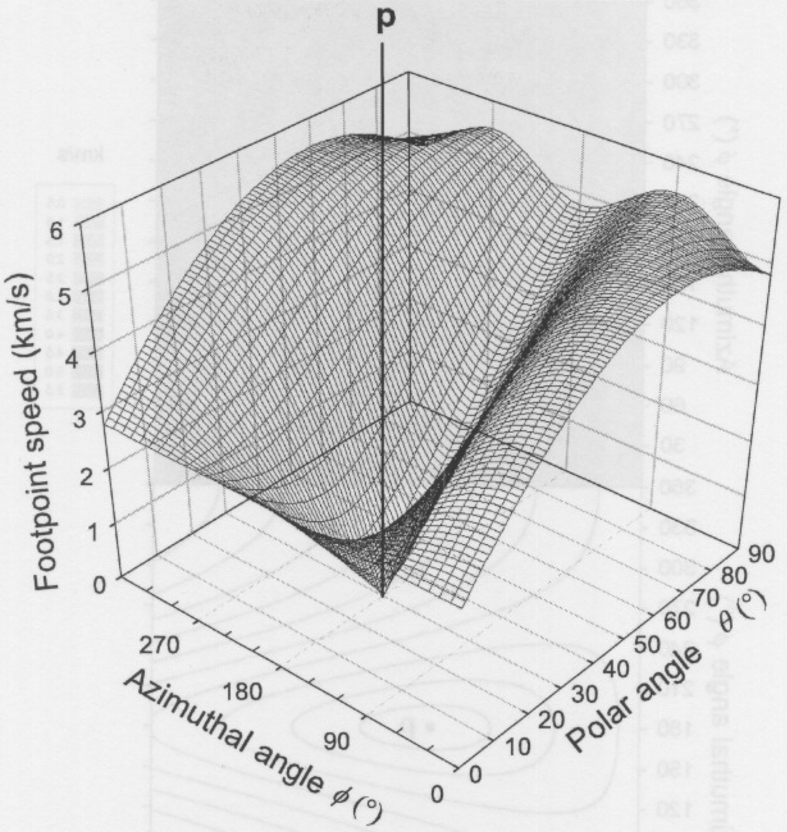

Figure 4.4: A three-dimensional representation of the footpoint speed distribution in the PCH from the poles to a constant heliographic polar angle of 70° on the source surface, assumed to be at a radial distance $r_{SS} = 10\, r_{\odot}$. The **p**-axis is located at $\theta = \beta = 30°$ and $\phi = 180°$. A constant differential rotation rate of $\omega = \Omega/4$ is assumed.

to the field line's photospheric footpoint, can be derived if the PCH boundaries on the photosphere and SS are known. The circular footpoint trajectories on the photosphere can then easily be mapped to the corresponding trajectories on the SS. This is done by performing a few coordinate transformations. The photospheric trajectories are concentric and circular about Ω and thus independent of θ. Transformation to magnetic coordinates is performed and the corresponding magnetic coordinates of the SS footpoints are then calculated. Finally, the coordinates of the SS footpoints are transformed back to heliographic coordinates. A contour graph of the speed distribution and the corresponding footpoint trajectories is shown in Figure 4.5. The trajectories are quasi-circular about the **p**-axis on the surface of a sphere. The flat geometry in Figure 4.5 distorts these trajectories. The open trajectories are the result of footpoints leaving the PCH. Clearly, the speed of a footpoint is correlated with the scale size of its trajectory and typically increases with increasing polar angle (decreasing latitude).

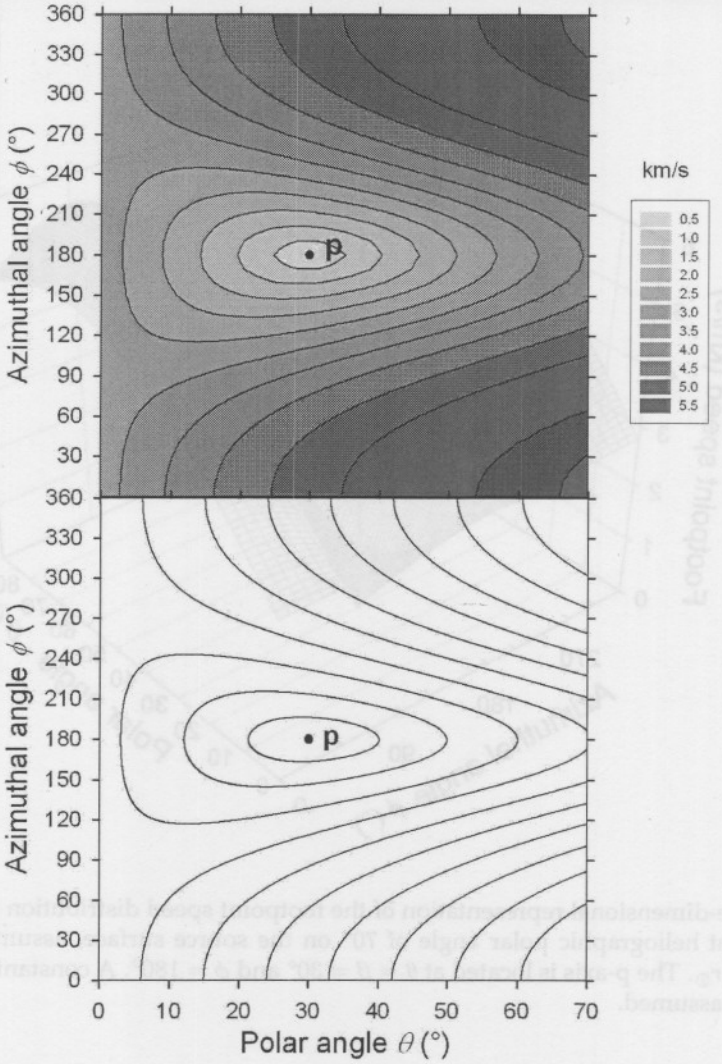

Figure 4.5: A contour graph of Figure 4.4 (above) and the corresponding footpoint trajectories (below), both on the SS as function of heliographic coordinates. The speed in the top panel is given in km/s. The location of the **p**-axis is shown in both panels.

4.6 Investigation into the Basic Assumptions of the Fisk Model

In this section the implication and validity of all assumptions necessary to obtain the Fisk HMF are investigated. *Fisk* [1996] initially described the model systematically in four points, while *Fisk et al.* [1999a] based the model on three basic assumptions. The Fisk model is only valid when the magnetic field lines on the SS move significantly in heliographic latitudes. In order to attain this condition, all three basic assumptions are necessary and are considered separately. The information contained in these assumptions can be rearranged in order to separate the behaviour of the magnetic axis **M** from that of the field lines and their footpoints. The modified assumptions are then the following:

- The magnetic field lines are attached to the differentially rotating photosphere.
- The magnetic axis, **M**, is offset from the rotational axis Ω and rotates rigidly at almost the equatorial rotation rate.
- The magnetic field lines expand non-radially from the photosphere and symmetrically about **M**.

Here, the first assumption describes the behaviour of the field lines' photospheric footpoints, the second assumption deals with the properties of **M** and the last assumption describes the behaviour of the CMF lines, i.e. the field lines between the photosphere and the SS.

4.6.1 Assumption 1: The magnetic field lines are attached to the differentially rotating photosphere

The first assumption becomes *invalid* when either (a) the HMF is not attached to the photosphere or when (b) the magnetic footpoints inside a PCH co-rotate rigidly with **M**, which in turn co-rotates at the equatorial rate.

(a) First consider the case if the statement in Part (a) is *true*. When the field lines are not attached to the photosphere, the photospheric footpoints will rotate slower than the ambient plasma, implying that the differential rotation of the photospheric footpoints, with respect to **M**, will be significantly larger and consequently the SS footpoints will rotate faster about **p**. If the footpoints are essentially stationary in the time-stationary observer system, the photospheric footpoints do not wind up about Ω and neither the Parker spiral nor the Fisk field is obtained.

In order to test the validity of Part (a), note that magnetic field lines are continuous according to Maxwell's equations and that the largest number of open CMF lines is connected to the deep interior regions of the sun. These field lines will therefore be attached to the photosphere, unless the diffusion rate of the field exceeds the differential rotation rate of the underlying photosphere. In Section 2.5.3 it is noted that differential rotation is the dominant transport mechanism at most locations inside PCHs during minimum solar activity conditions and therefore the footpoints can be assumed to remain attached to the photosphere. However, at certain locations inside PCHs and during higher solar activity conditions, the diffusion of the CMF dominates the Fisk field completely and a turbulent Parker field becomes a more realistic approximation.

Inside non-polar CHs, diffusion plays a significant role, due to the relatively small scale sizes and short lifetimes of most of these holes. *Horbury et al.* [1998] remark that the photospheric footpoints must remain connected to those on the SS for periods longer than the solar rotation period in order for the Fisk field to have a significant global effect. The Fisk field is therefore expected to originate only from the inner regions of the larger and steadier differentially rotating CHs. Such CHs occur typically in the polar region during solar maximum (see Section 2.5.2). These CHs may therefore make a small contribution to the Fisk field.

(b) Next, consider the case when the photospheric footpoints co-rotate rigidly with **M** and not differentially. The footpoints then remain approximately at fixed heliomagnetic coordinates and consequently the amount of non-radial expansion of every field line remains approximately the same. The result is not a Fisk field, but the well-known Parker spiral. This is evident in the time-stationary system where the magnetic configuration rotates as a unit about $\mathbf{\Omega}$. Rigid rotation corresponds to $\omega = 0$, for which the Fisk HMF [Eq. (4.16)] reduces to the standard Parker HMF.

4.6.2 Assumption 2: The magnetic axis, M, is offset from the rotational axis Ω and rotates rigidly at approximately the equatorial rotation rate.

The second assumption consists of two parts: (a) **M** is inclined with respect to $\mathbf{\Omega}$, and (b) rotates rigidly at nearly the equatorial rotation rate.

(a) When **M** is parallel to $\mathbf{\Omega}$, the photospheric footpoints remain at fixed magnetic coordinates. The axes **p**, **M** and $\mathbf{\Omega}$ then coincide and a Parker field results. However, observations indicate that **M** is always inclined with respect to $\mathbf{\Omega}$, i.e. α becomes small, but never zero (see Fig. 2.16). Due to the presence of large PCHs during solar minimum, a significant Fisk field is expected during these conditions.

(b) Consider the case when Part (b) is *invalid*. First note that it is reasonable to assume that the whole photosphere in the PCH rotates at a single angular rate, since the PCH covers only a relatively small area on the photosphere. The case of **M** co-rotating with the local differentially rotating photosphere is similar to Part (b) in the first assumption for the case when **M** co-rotates rigidly with the photosphere in the PCH, resulting in a Parker field.

According to observations and the plasma dynamo model, Part (b) of Assumption 2 is reasonable during minimum and moderate solar activity conditions. Firstly, since the magnetic equator co-rotates rigidly with the low-latitude field at low solar activity and **M** is normal to the magnetic equator, **M** also rotates rigidly and hence remains fixed in the co-rotating frame. From the plasma dynamo model it follows that **M** is connected to the rigidly rotating poloidal field and therefore rotates rigidly during periods when the poloidal field dominates. At higher solar activity states, the magnetic equator reaches high heliolatitudes and becomes distorted due to the differentially rotating photosphere. The influence of the toroidal field then contributes to the property that **M** may not be defined clearly, and the Fisk effect should decrease significantly.

4.6.3 Assumption 3: The magnetic field lines expand non-radially from the photosphere and symmetrically about M.

A few conditions can be identified for which the third assumption becomes *invalid*, viz. (a) when the expansion of the field lines from the photosphere to the SS is not symmetric about **M**, and (b) when the field lines expand essentially radially rather than superradially.

(a) The PFSS model ensures a uniform magnetic field on the SS and therefore eliminates effects which result in a magnetic pressure build-up on the SS. The symmetric expansion of the field lines about **M** is accordingly a consequence of the PFSS [*Fisk et al.*, 1999a], which was employed in Section 4.3 to derive the footpoint motion equations.

Observations from *Ulysses* indicate a uniform magnetic pressure in the higher corona near solar minimum conditions [*Balogh et al.*, 1995]. As discussed in Sections 2.5.5 and 3.2, the validity of a PFSS model is questioned by some researchers, but it nevertheless yields reasonable results.

(b) Above closed field structures in the corona, most of the field lines are concentrated in CHs, resulting in large magnetic pressure gradients between the outside and the inside of the holes. In order to release this tension, the field lines expand laterally over the closed field structures. It has been observed that the subtended solid angle of a PCH increases by more than a factor of 7 from the photosphere to the high corona [see, e.g., *Cranmer et al.*, 1999, and references therein]. Only when a CH is sufficiently small and when other large pressure gradients, resulting from highly active features, are present, can it be expected that the amount of superradial expansion will be greatly reduced. A few rotations before the disappearance of the PCH near the polarity reversal of the global field, magnetic stresses may force an almost radial expansion. Obviously, for radial expansion the field lines remain at fixed heliolatitudes on the SS in the co-rotating frame, and a Parker spiral is obtained. Briefly stated, superradial expansion from PCHs and all CHs during the largest fraction of the solar cycle is a reasonable assumption.

4.6.4 Conclusion

From the discussion about the validity of the three basic assumptions of the Fisk model, it can be concluded that the occurrence of the Fisk field depends strongly on latitude and solar activity. The Fisk field is mainly restricted to PCHs, with its largest effect during moderate activity periods of the sun and a smaller effect during solar minimum. During these periods a Fisk field is an unavoidable consequence according to the three basic assumptions. During solar maximum conditions no Fisk field is expected from PCHs, but the presence of quasi-steady non-polar CHs in the polar region may result in a small Fisk effect. During the remaining period of the solar cycle, non-polar CHs do not contribute significantly to the Fisk field due to the rigid rotation of most of the holes as well as their relatively short lifetimes and small scale sizes.

4.7 Boundary Conditions of the Source Surface Footpoint Motion

As shown in the previous section, the Fisk field is only present well inside PCHs and the inner regions of long-living CHs. At the PCH boundary and outside, the behaviour of the SS footpoints change significantly. The velocity field is therefore subject to certain boundary conditions. *Fisk et al.* [1999a] proposed the following three assumptions to be valid on the whole SS.

- A steady magnetic field on the SS is assumed, i.e. a field that is constant in time. This is a reasonable approximation near solar minimum conditions [*Balogh et al.*, 1995]. During higher activity conditions, the magnetic field can become highly time-dependent and perturbed and this assumption becomes invalid.
- Following the PFSS model, the field strength is assumed to be uniform on the SS.
- Magnetic field lines are not allowed to cross the magnetic equator and consequently change polarity. Conservation of magnetic flux then requires that the meridional component of the velocity field vanishes at this boundary.

The combination of the first two assumptions results in a divergence-free velocity field on the whole SS. This is derived in Section 4.8. Physically, a divergence-free velocity field prevents any pressure build-up on the SS and the field thus remains force-free. A force-free, radial magnetic field has a constant magnitude, satisfying the second boundary condition [*Fisk et al.*, 1999a].

Fisk et al. [1999a] argue that the footpoint velocities should be non-zero outside the PCH in order to prevent a pressure build-up, resulting from the continuous flux of field lines that cross the PCH boundary. The non-zero, divergence-free velocity field then requires closed footpoint trajectories. Since the field lines cannot cross the magnetic equator, the only recourse is footpoint motion around the PCH in a region between the PCH boundary and the magnetic equator. This region is referred to as the 'return region' and is shown in Figure 4.6 [adapted from *Fisk et al.*, 1999a]. Here, the boundary between the PCH and the return region is located at a constant magnetic polar angle θ_{M1}, and the return region is defined by the magnetic latitude band between this boundary and the magnetic equator, referred to as the neutral line in this figure, in both hemispheres. Inside the return region, a SS footpoint that leaves the PCH on one side is transported around the PCH to the location of entrance on the opposite side in order to create a closed trajectory. This transport results from the dominant diffusion process outside the PCH, viz. reconnection between open and closed field lines (see Section 3.5). The SS footpoints then propagate from one side to the opposite side of the sun by means of a series

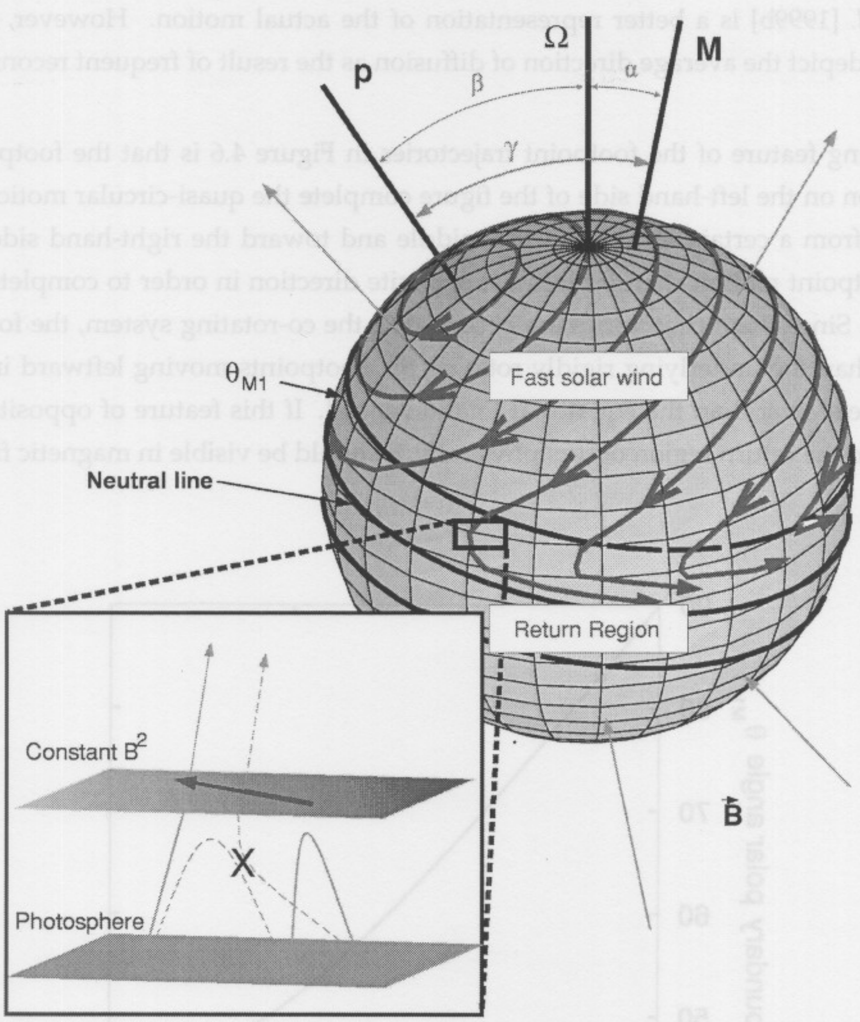

Figure 4.6: An illustration of the closed footpoint trajectories on the source surface. The footpoints that leave the PCH, denoted by the fast solar wind region, return to the opposite side of the sun in the so-called 'return region'. In terms of magnetic coordinates, this region is located between the PCH boundary θ_{M1} and the magnetic equator, or neutral line, at $\theta_m = \pi/2$. The reconnection process by which the footpoints in the return region propagate, is illustrated in the inset [adapted from *Fisk et al.*, 1999a].

of rapid reconnections. This process is illustrated in the inset in Figure 4.6: The dashed lines denote the original field lines. The open dashed field line originates from the photosphere near the PCH boundary. It expands superradially, passing close to a coronal loop on the outside of the boundary. In order to maintain a constant magnetic pressure on the SS, the stress resulting from the sharp bend in the open line is released by means of reconnection between the two field lines (see Section 2.5.3). The resulting field lines are denoted by the solid lines. In this way the SS footpoint 'jumps' in the direction of the reconnection, as indicated by the arrow. A similar process describes the flux of field lines into the PCH on the opposite side of the sun.

In reality, reconnection is a random walk process and the resulting footpoint trajectories in the return region are not as smooth as illustrated in Figure 4.6. The zig-zag motion discussed by *Fisk et al.* [1999b] is a better representation of the actual motion. However, the smooth trajectories depict the average direction of diffusion as the result of frequent reconnections.

An interesting feature of the footpoint trajectories in Figure 4.6 is that the footpoints in the return region on the left-hand side of the figure complete the quasi-circular motion about the **p**-axis, but from a certain location in the middle and toward the right-hand side of the figure, the footpoint motion changes into the opposite direction in order to complete the closed trajectories. Since these trajectories are observed in the co-rotating system, the footpoints rotate faster than the underlying rigidly rotating SS. Footpoints moving leftward in the return region move slower than the equatorial rotation speed. If this feature of oppositely directed footpoints in the return region occurs physically, it should be visible in magnetic field data.

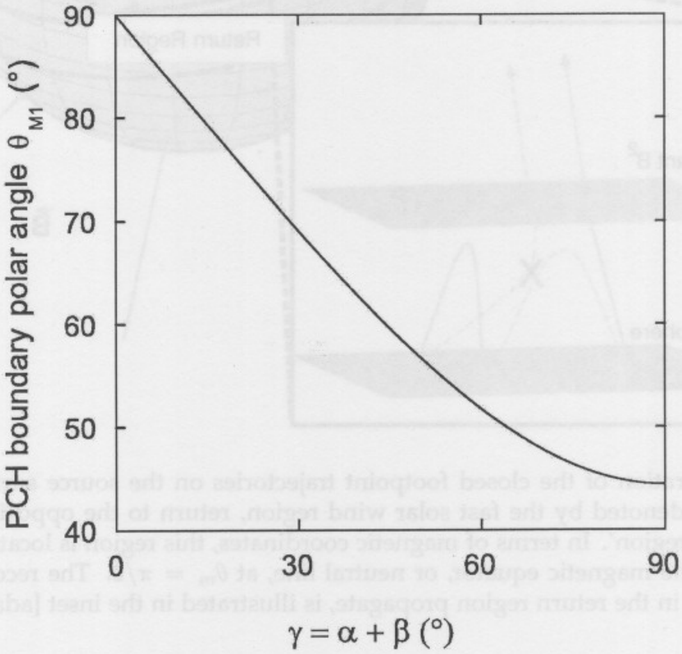

Figure 4.7: The upper limit of the magnetic polar angle of the PCH boundary as function of the angle between **M** and **p** when a PCH symmetric about **M** is assumed.

Since the PCH boundary is symmetric about **M** on the SS in the model of Fisk, whereas the trajectories are symmetric about **p**, the number of incomplete footpoint trajectories increases with $\gamma = \alpha + \beta$, i.e. the amount of flux into and out of the PCH increases with γ (see, e.g., the projections illustrated by *Fisk* [1996] and *Van Niekerk* [2000]). This implies that the density of footpoint trajectories increases with γ outside the PCH, which must be compensated for by increasing the width of the return region. Assuming that the return region covers the whole region between the PCH boundary, θ_{M1}, and the magnetic equator, the maximum value that θ_{M1} can attain depends strongly on γ. *Fisk et al.* [1999a] proposed that θ_{M1} must satisfy the following condition:

$$\cos\theta_{M1} > \frac{\omega r_{\odot}\sin\gamma}{\lambda/\tau}, \tag{4.17}$$

where λ and τ are the typical size and lifetime of a loop, respectively, and ω is the differential rotation rate of the photosphere. Figure 4.7 shows the relation between θ_{M1} and γ according to Equation (4.17) for the typical values $\lambda = 10^5$ km and $\tau = 1.5$ days from *Schwadron et al.* [1999] and $\omega = 0.79$ μrad/s. Note that the y-axis only shows the upper limit of θ_{M1}. When $\gamma = 0$, all the footpoint trajectories are inside the PCH and accordingly, no return region is needed. Each PCH can then cover a whole magnetic hemisphere. Physically, the PCH, as indication of the fast wind region, does not intersect this far into the slow wind region (see Section 2.6) and a smaller θ_{M1} is more reasonable. The PCH boundary decreases with γ until $\gamma = 90°$ when **p** is located on the magnetic equator. Then θ_{M1} cannot exceed $\sim 45°$. *Fisk* [1996] assumes the values $\alpha = 15°$, $\beta = 30°$ and $\theta_{M1} = 75°$. However, these values are inconsistent with the condition in Equation (4.17) which yields $\theta_{M1} \lesssim 60°$ for $\gamma = 45°$. The validity of the return region is discussed in Section 4.9.

4.8 The Divergence-Free Nature of the Source Surface Velocity Field

The dynamics of a magnetic field is described by the induction equation

$$\frac{\partial \mathbf{B}}{\partial t} = \nabla \times (\mathbf{u} \times \mathbf{B}) + \lambda \nabla^2 \mathbf{B}, \tag{4.18}$$

where $\mathbf{u}$ is the velocity field and $\lambda = \frac{c^2}{2\pi\sigma}$ is the magnetic diffusivity, with σ the electrical conductivity and c the speed of light in vacuum.

In the PFSS model, the frozen-in condition implies $\sigma = \infty$, hence $\lambda = 0$ and Equation (4.18) reduces to

$$\frac{\partial \mathbf{B}}{\partial t} = \nabla \times (\mathbf{u} \times \mathbf{B}). \tag{4.19}$$

Now,

$$\begin{aligned} \frac{\partial}{\partial t}\left(\frac{B^2}{2}\right) &= \mathbf{B} \cdot \frac{\partial \mathbf{B}}{\partial t} \\ &= \mathbf{B} \cdot [\nabla \times (\mathbf{u} \times \mathbf{B})] \\ &= \mathbf{B} \cdot [(\mathbf{B} \cdot \nabla)\mathbf{u} - (\mathbf{u} \cdot \nabla)\mathbf{B} + \mathbf{u}(\nabla \cdot \mathbf{B}) - \mathbf{B}(\nabla \cdot \mathbf{u})]. \end{aligned} \tag{4.20}$$

The second last term in the last line falls away due to the divergence-free property of a magnetic field. Let $u_\perp$ denote the transverse velocity, i.e. the velocity normal to the magnetic field direction. Then only the last term in Equation (4.20) remains non-zero. This is evident by writing the last line in tensor notation and by using the fact that **B** is radial and constant in magnitude on the SS:

$$\begin{aligned} \frac{\partial}{\partial t}\left(\frac{B^2}{2}\right) &= B_i\left(B_j\frac{\partial u_i}{\partial x_j} - u_j\frac{\partial B_i}{\partial x_j} + 0 - B_i\frac{\partial u_j}{\partial x_j}\right) \\ &= B_r\left(B_r\frac{\partial u_\perp}{\partial r} - u_\perp\frac{\partial B_r}{\partial x_\perp} - B_r\frac{\partial u_\perp}{\partial x_\perp}\right) \\ &= -B^2(\nabla\cdot\mathbf{u}_\perp). \end{aligned} \tag{4.21}$$

According to the PFSS model, the magnetic pressure on the SS is constant and therefore the left-hand side of Equation (4.21) equals zero, implying that the velocity field is divergence-free, i.e.

$$\nabla\cdot\mathbf{u}_\perp = 0. \tag{4.22}$$

To obtain this result, *Fisk et al.* [1999a] first rewrites Equation (4.21) in the form

$$\begin{aligned} &= -\nabla\cdot(B^2\mathbf{u}_\perp) + \mathbf{u}_\perp\cdot\nabla B^2 \\ &= -\nabla\cdot(B^2\mathbf{u}_\perp) - 2\mathbf{u}_\perp\cdot\left[(\nabla\times\mathbf{B})\times\mathbf{B}\right], \end{aligned} \tag{4.23}$$

where the product rule for divergences is used in the first line, and the last term follows from

$$\begin{aligned} \nabla B^2 &= \nabla(\mathbf{B}\cdot\mathbf{B}) \\ &= 2\left[\mathbf{B}\times(\nabla\times\mathbf{B}) + 2(\mathbf{B}\cdot\nabla)\mathbf{B}\right] \\ &= -2\left[(\nabla\times\mathbf{B})\times\mathbf{B}\right] + 2\mathbf{B}(\nabla\cdot\mathbf{B}) \\ &= -2\left[(\nabla\times\mathbf{B})\times\mathbf{B}\right]. \end{aligned} \tag{4.24}$$

Then, since the magnetic field on the SS is force-free and uniform in strength, the last term in Equation (4.23) vanishes and

$$-\nabla\cdot(B^2\mathbf{u}_\perp) = -B^2(\nabla\cdot\mathbf{u}_\perp) = 0, \tag{4.25}$$

implying the divergence-free property of the velocity field. (Note the constant of two in Equation (4.23), which is not given in *Fisk et al.* [1999a].)

4.9 Restrictions of the Fisk Model

4.9.1 The Return Region

Although the return region is a mathematical necessity according to the assumptions proposed by *Fisk et al.* [1999a], it is physically difficult to motivate.

The property that the footpoints in the return region on the left- and right-hand sides of Figure 4.6 propagate on average in opposite directions can and should be tested with magnetic field data. Until such time, it suffices to say that it seems unlikely that such behaviour exists. Furthermore, the closed footpoint trajectories suggest that every footpoint that enters the return region propagates to the opposite side of the sun and enters the PCH again. Since the randomness of the reconnection of the open field lines in the return region is expected to increase with distance from the PCH, the footpoint behaviour in the return region, as suggested by Figure 4.6, may be altered significantly.

4.9.2 Polar Coronal Hole Boundaries

It is assumed that the PCH boundary is defined at a constant heliomagnetic latitude. In reality, the boundaries of PCHs are very ragged and time-dependent due to the variable and sporadic reconnections between the loops that define the PCH boundaries and other field lines. Furthermore, the two hemispheres of the sun are not alike and therefore the PCHs differ in both strength and position [see, e.g., *Hoeksema*, 1995; *Roelof et al.*, 1997]. Realistic PCH boundaries influence the Fisk field configuration significantly and the use of smooth, circular and steady boundaries may be necessary [*Fisk et al.*, 1999a], but it is an oversimplification.

4.9.3 Axial Symmetry of the PCH Boundaries

Fisk and co-workers proposed a PCH that is symmetric about the magnetic axis **M** in the whole region from the PCH to the SS. In this field configuration, the PCH follows **M** toward the heliographic equator during the increasing activity phase of the sun. Such behaviour, however, is inconsistent with observations indicating that PCHs remain at the heliographic poles on the photosphere during their lifetime [see, e.g., *Waldmeier*, 1981; *Webb et al.*, 1984; *Harvey and Recely*, 2002].

4.10 Evidence for the Fisk Field

If the Fisk HMF exists, its signature is expected to be observed in both the local and global behaviour of energetic particles in the heliosphere, as well as in the variation of the magnetic field magnitude and direction, especially in the regions above the solar poles.

4.10.1 The Behaviour of Energetic Particles

Perhaps the strongest current evidence for the Fisk field is the property that this model can in principle explain the observations of the high-latitude 26-day variations [*Burger and Hitge*, 2004]. In Chapter 6, this phenomenon is investigated by means of numerical simulations.

4.10.2 Magnetic Field Properties

Zurbuchen et al. [1997] show that the Fisk model provides an explanation for the over- and underwound field structure in comparison with the Parker spiral at different locations in the heliosphere. *Fisk et al.* [1999a] remark that the overwound field at high latitudes in the southern hemisphere observed by *Ulysses* [see, e.g., *Forsyth et al.*, 1995] is difficult to explain sufficiently by any other model. *Zurbuchen et al.* [1997] analysed the magnetic field measurements from *Ulysses* and found that the systematic variations of the meridional and azimuthal components of the observed field are consistent with the unique periodicity of about 20 days at high latitudes that results from the Fisk field. This indicates that the Fisk model gives rise to a field structure with a systematically varying spiral angle, ψ, in comparison with the Parker spiral at different locations in the heliosphere. However, this property was also investigated by *Forsyth et al.* [2002], who found that it is very difficult to confirm any systematic variability produced by the Fisk field. According to their analysis, systematic variations of ψ can still be present, but the amplitude is probably too small to be reliably detected in *in situ* HMF measurements. By using data averaged over a larger time-scale than what *Zurbuchen et al.* [1997] used, they found that the presence of large-scale Alfvén waves at high latitudes reduces the systematic variations. This result is confirmed by *Erdös and Balogh* [2005]. *Van Niekerk* [2000] shows that the average spiral angle of the Fisk and Parker fields differ by only $\sim 1^\circ$. This result also indicates that observations of an over- or underwound field do not support the Fisk field.

Identifying the signature of the Fisk field from magnetic field data therefore still needs some conscientious investigation.

4.11 The Fisk-Parker Hybrid Field

Burger and Hitge [2004] modified the Fisk field in order to implement the field in the three-dimensional numerical modulation code of *Hattingh* [1998]. Their purpose was to develop a divergence-free HMF that is easier to implement than the Fisk field but which is still a reasonable approximation of the field. This modified Fisk field constitutes a Fisk-Parker hybrid field.

Since it is more convenient to use spherical heliographic coordinates in the numerical modulation code, the PCH boundary in the hybrid model is assumed to be symmetrical about $\mathbf{\Omega}$, instead of about $\mathbf{M}$ on the SS. The footpoint velocity equations (4.15) on the SS are then described in terms of these heliocentric coordinates instead of magnetic coordinates. This change of symmetry does alter the qualitative global effect of the Fisk field near solar minimum conditions [*Burger and Hitge*, 2004].

A PCH does not intersect far into the slow solar wind region around the magnetic equator and therefore the PCH boundary is at least $10^\circ - 20^\circ$ from it (see Section 2.6). Outside the PCH, in the slow wind region, the photosphere rotates rigidly and a Parker field is therefore a reasonable approximation. This motivates the Parker field at the solar equator in the model of *Burger and Hitge* [2004].

Fisk [1996] points out that it is not clear whether differential rotation persists to the polar regions. Figure 2.5 in Section 2.3 suggests that differential rotation occurs in the polar regions of the sun, but model results are not considered reliable at these latitudes [*Schou et al.*, 1998]. It is therefore possible that the polar region rotates rigidly, which will result in the standard Parker field originating from these regions. This motivates the Parker field at the solar poles in the hybrid model of *Burger and Hitge* [2004]. In the next chapter it is shown that a Parker field may be a reasonable description of the HMF in the polar regions, but due to a different reason.

For the purpose of the numerical model, a latitude dependent transition function which becomes zero at the equator and poles is used, given by

$$F_S = \{\tanh[\delta_p\theta] + \tanh[\delta_p(\theta - \pi)] - \tanh[\delta_e(\theta - \pi/2)]\}^4, \tag{4.26}$$

where the constants δ_p and δ_e determine the steepness of the transition to a Parker field at the poles and equator, respectively, and θ denotes the polar angle. The first two terms describe the behaviour at the northern and southern poles, respectively, and the last term at the equator. The transition function is shown in Figure 4.8 for the values $\delta_p = 5$ and $\delta_e = 4$. The heliocentric spherical coordinates components of the divergence-free hybrid magnetic field in a fixed frame

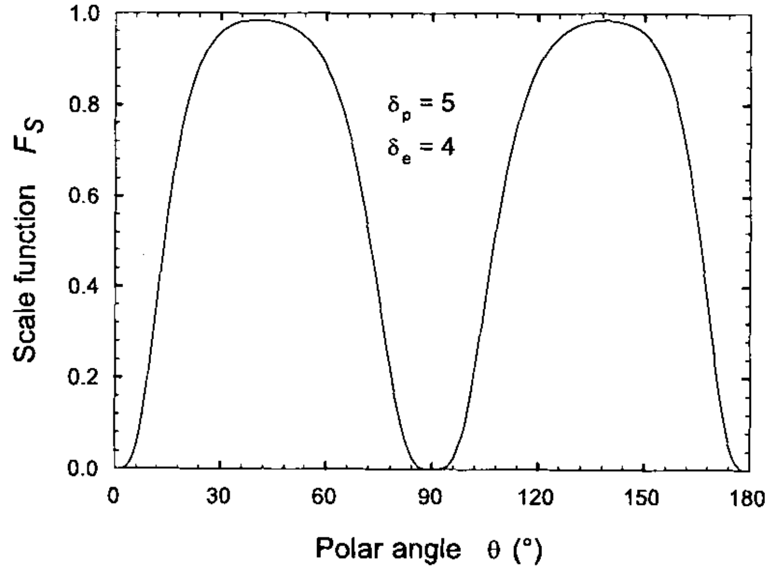

Figure 4.8: The transition function which is multiplied into the Fisk HMF in order to implement the resulting hybrid field easily in numerical codes. The function scales to zero at the solar poles and equator, where the HMF reduces to a Parker field. The steepness of the function at the poles and equator are determined by the constants δ_p and δ_e, respectively.

are then given by

$$\begin{aligned} B_r &= A\left(\frac{r_0}{r}\right)^2 \\ B_\theta &= B_r\frac{r\omega F_S}{V_{sw}}\sin\beta\sin\phi^* \\ B_\phi &= B_r\frac{r}{V_{sw}}\left[\omega F_S\sin\beta\cos\theta\cos\phi^* + \sin\theta(\omega F_S\cos\beta - \Omega) + \omega\frac{dF_S}{d\theta}\sin\beta\sin\theta\cos\phi^*\right]. \end{aligned} \tag{4.27}$$

where $\phi^* = \phi + \frac{\Omega(r-r_{SS})}{V_{sw}}$. This HMF results from a divergence-free footpoint velocity field on the SS, which in the co-rotating system is given by

$$\begin{aligned} u_\theta &= r\omega F_S\sin\beta\sin\phi_\Omega \\ u_\phi &= r\omega\left[F_S\sin\beta\cos\theta\cos\phi_\Omega + F_S\cos\beta\sin\theta + \tfrac{dF_S}{d\theta}\sin\beta\sin\theta\cos\phi_\Omega\right]. \end{aligned} \tag{4.28}$$

At mid-latitudes, $F_S \approx 1$ and the magnetic field reduces to the Fisk field [Eq. (4.16)]. At the equator and poles, $F_S = 0$, and the Parker field [Eq. (3.8)] is attained. The steepest transition between the Parker field and the Fisk field occurs within about 30° from the solar pole and equator. Note that the only constraint on F_S to obtain a divergence-free magnetic field is that it depends only on latitude. The Fisk field reduces to a Parker field when all the terms containing ω and β become zero. The footpoints then remain steady on the SS in the co-rotating system.

A Parker field at the solar equator, of course, prevents the footpoint trajectories on the SS to cross the solar rotational equator. The velocity field is then expected to yield footpoint trajectories that correspond qualitatively to the predicted trajectories obtained by *Fisk et al.* [1999a] at mid- and low latitudes. However, in the polar region the rotation rate of the SS footpoints decreases due to the transition to a Parker field and the trajectories are expected to become distorted. In order to compare the vizualised footpoint trajectories described by the hybrid field with those in Figure 4.6, it is therefore firstly assumed that the field remains a Fisk field over the solar poles. Then the first two terms in Equation (4.26) vanish, yielding

$$F_S = \tanh^4\left[\delta_e(\theta - \pi/2)\right], \tag{4.29}$$

so that $F_S = 1$ in the polar region.

Fisk [1996] uses PCH boundary values of $\theta_{mm} = 24°$ and $\theta'_{mm} = 75°$ and a tilt angle of $\alpha = 15°$, resulting in $\beta \approx 30°$. Furthermore, since the PCH only covers a small area in the polar region on the photosphere, the differential rotation rate of the photospheric footpoints in the PCH is fairly constant and can be approximated by the value at the pole, viz. $\omega \sim \Omega/4$ (see Section 2.3). Employing the values $\beta = 30°$, $\omega = \Omega/4$, $\delta_p = 5.0$ and $\delta_e = 4.0$ in Equation (4.28), the resulting footpoint trajectories are illustrated in Figure 4.9. These trajectories were constructed in **Mathematica** by solving the velocity field equations (4.28) simultaneously.

As expected, by employing a Fisk field in the polar region, Figure 4.9 corresponds qualitatively to Figure 4.6. Only the symmetry is different: in the former the PCH is symmetric about Ω;

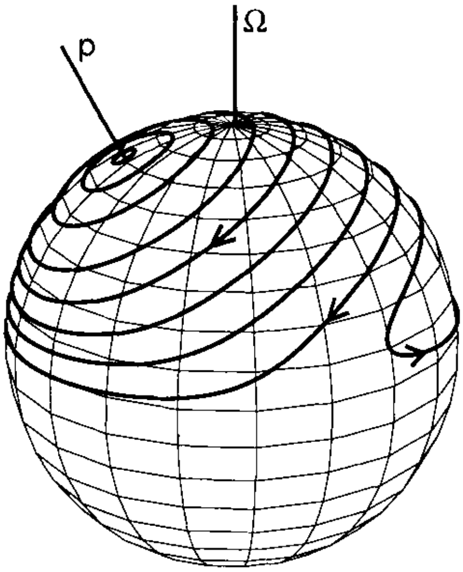

Figure 4.9: Footpoint trajectories on the source surface according to a hybrid field that scales to a Parker field toward the PCH boundary at the solar equator, but remains a Fisk field over the solar poles. These trajectories are observed in a frame that co-rotates at the solar equatorial rotation rate. The angle β between $\mathbf{\Omega}$ and the virtual axis $\mathbf{p}$ is assumed as 30° [*Burger and Hitge*, 2004].

in the latter the symmetry is about **M**. The behaviour of the trajectories in Figure 4.9 can be explained as follows. The influence of the latitude dependent transition function [Eq. (4.29)] greatly distorts the circular trajectories near the solar equator. Toward the equator, F_S decreases and $dF_S/d\theta$ becomes dominant. The component u_θ in Equation (4.28) then decreases and u_ϕ increases. At the equator, $F_S = dF_S/d\theta = 0$ and the footpoint velocity becomes zero so that the footpoint on the equator takes an infinite time to rotate.

Evidently, the effect of the transition function in the velocity field results in a return region similar to that proposed by Fisk and co-workers [*Fisk et al.*, 1999a]. In this region, the circular trajectories are distorted and the footpoints return to the opposite side of the sun. Note that the density of trajectories in the return increases, similar to those in Figure 4.6. This accumulation of the trajectories does not imply an increase in the magnetic density. The constant magnitude of the magnetic field is attained by the slower rotating footpoints in the return region.

The PCH boundary is not clearly defined. The polar angle where the distortion starts, as well as the amount of distortion, only depends on the steepness of transition. In Figure 4.9 it can be observed that the largest distortion of the circular trajectories occurs between $\theta \sim 75^\circ$ and the solar equator. The polar angle $\theta \sim 75^\circ$ is coincidently the SS PCH boundary used by Fisk and co-workers. The return region then covers the region between this angle and the solar equator and the boundary of the PCH is located at $\theta \sim 75^\circ$.

In the hybrid model, both the PCH and return region are symmetric about $\mathbf{\Omega}$. Since the return region extends to the rotational equator, this symmetry causes the return region to cross the magnetic equator for all non-zero values of α. It is therefore clear that the size of the PCH and therefore the polar angle of its boundary must decrease with solar activity. This is the main object of Section 5.6.

4.12 Summary

The Fisk model is the first attempt to construct a solar magnetic field which connects the behaviour in and above the photosphere to the outer regions of the heliosphere. In this chapter the structure, properties and attributes of the Fisk HMF were investigated. This field could present an acceptable explanation for the 26-day periodic variations of particle intensities that were observed up to high latitudes during the first FLS of *Ulysses*. The Fisk field is created by the varying non-radial expansion of the CMF lines inside PCHs and some long-living CHs, resulting from the varying magnetic location of their differentially rotating photospheric footpoints. The corresponding source surface footpoints of the field lines wind up the radially directed magnetic field lines about two axes simultaneously.

It is suggested that for the largest fraction of the solar activity cycle, the Fisk field is unavoidable for a field originating inside a PCH. Non-polar CHs do not contribute significantly to the Fisk field except probably at high latitudes near solar maximum conditions during the time when the PCH decreases significantly in size.

The footpoint motion equations and the resulting footpoint velocities on the SS were derived. The global structure of the Fisk field was briefly described and the conditions at the PCH boundary were investigated. Some important restrictions of the Fisk model result from the concept of the return region, the smooth, steady PCH boundaries that are assumed and the symmetry of the PCH. It was further shown that identifying a signature of the Fisk field from observational data is extremely difficult and needs some further investigation.

In the next chapter it is shown that a refined Fisk-Parker hybrid model resolves some of the restrictions of the Fisk model and may be a better representation of the actual heliospheric field. Furthermore, the refined hybrid model is constructed to remain valid during the whole solar cycle, given some basic assumptions.

Chapter 5

A Fisk-Parker Hybrid Model of the HMF

5.1 Introduction

The hybrid field model developed by *Burger and Hitge* [2004] makes it possible to implement a Fisk-type field in numerical modulation models, as was the original intention, and it is also a reasonable representation of the actual heliospheric magnetic field. The transformation from a Fisk-type field in a PCH to a Parker-type field outside of it is not only a mathematical construction, but simulates the behaviour of magnetic field footpoint motion in the so-called return region, where differential rotation no longer dominates.

The main focus of this chapter is to explain the significance of the hybrid field model and to refine it. Firstly, the influence of magnetic field diffusion on the Fisk field from a PCH is investigated. Thereafter, the Fisk-Parker hybrid magnetic field equations from Section 4.11 are refined and the subsequent footpoint velocities on the source surface are illustrated. It is then shown how the hybrid field resolves some restrictions of the Fisk model. Part of the refinement consists of making the hybrid model applicable during the whole solar activity cycle. The magnetic field equations that are used in a numerical code and the relevant parameters that are used in these field equations are also given. Finally, the validity of the hybrid field is discussed and some general applications of the field are given.

5.2 The Role of Magnetic Diffusion in a Polar Coronal Hole

In this section it is shown that magnetic diffusion plays a significant role in Fisk-type fields near the PCH boundary, as well as over the solar poles. In order to determine the dominant transport process of the magnetic footpoints at all locations on the photosphere and SS, all the relevant diffusion processes need to be compared with one another. First, the processes on the photosphere are considered and thereafter their effect on the SS footpoints and some consequences are inferred. Finally, the resulting behaviour is explained with the help of an analogy.

5.2.1 Transport Processes on the Photosphere

In Section 3.5 the most important diffusion processes on the photosphere are discussed. It is found that the two convection-related diffusion processes, supergranulation and the emergence of new magnetic flux, dominate inside PCHs on a scale of several supergranules, resulting in a diffusion speed of $\sim 0.2 - 0.3$ km/s. Outside PCHs, reconnection becomes the dominant transport process on a scale of several coronal loops, with a diffusion speed of ~ 0.7 km/s.

Section 2.3 is devoted to the discussion of differential rotation, a nearly steady transport process of the plasma in the solar interior, which features on the photosphere. Since the magnetic field lines that emerge from the photosphere are essentially frozen into it, this differential rotation results in a nearly steady, coherent motion of the photospheric field lines. On large time and length scales, this motion could completely dominate the random behaviour of all the diffusion processes.

Comparing the characteristic size, $\sim 3 \times 10^4$ km, of a supergranule to the solar radius, it can be inferred that a supergranule subtends an angle of about 2.5° on the photosphere. The scale size of the polar region at the highest latitudes is therefore comparable to the size of several supergranules, and magnetic diffusion cannot be ignored, even on large time scales.

Note from Figure 2.4 in Section 2.3 that the differential rotation speed, V_ω, never exceeds approximately 0.19 km/s, which is less than or comparable with the diffusion speeds resulting from the different diffusion processes. Again, according to Section 3.5, the nearly steady rotation could be the principal transport mechanism on large time scales and therefore could dominate the localised diffusion processes. This applies to regions away from the solar poles and equator where $V_\omega > 0$.

Toward the poles, the behaviour that $V_\omega \to 0$ results from the relatively small distance the plasma travels within a solar rotation period. At the solar equator the photosphere is essentially stationary in the co-rotating frame due to its almost rigid rotation. At the solar poles and equator, random magnetic diffusion therefore dominates in the co-rotating system and a turbulent Parker field, which is exactly the field described in the model of *Giacalone* [1999], becomes a reasonable approximation.

Consider now the PCH boundaries that extend only to a polar angle of $\sim 30°$ on average on the photosphere during minimum solar activity [see, e.g., *Waldmeier*, 1981]. According to Figure 2.4, the differential rotation speed is the largest at this angle and an abrupt transition from a Fisk field inside the PCH to another kind of field outside it is expected, as was assumed by *Fisk et al.* [1999a]. However, the influence of the ragged, non-steady PCH boundaries may not be ignored. Due to these boundaries, rapid, random reconnection is expected to cover several latitudes over the PCH boundary. As the sun rotates, a fixed observer in this latitude band will then observe a mixture of turbulent Fisk- and Parker-type fields.

A key question is whether a Fisk-type field would occur at all, given the fact that the estimated small-scale diffusion speed inside PCHs is actually larger than the differential rotation speed. *Fisk* [2005], however, argues that at large scales a more appropriate value for the diffusion speed is approximately 0.005 km/s (see Section 3.5). It was pointed out in Section 4.10 that there are opposing views for a direct signature in the observed magnetic field. However, an indirect signature in the behaviour of particle intensities may provide a firm answer, and will be considered in Chapter 6.

In what follows, the turbulent nature of the HMF beyond the SS will be neglected.

5.2.2 Footpoint Trajectories on the Source Surface

Based on what happens on the photosphere, the following behaviour of the SS footpoints (when viewed in a system co-rotating with the solar equator) is expected during solar minimum activity conditions. Consider Figures 4.1 and 4.6 for the sake of clarity.

- The region around the $\mathbf{p}$-axis on the SS maps to the polar region on the photosphere, where random convection-related diffusion dominates and the consequent field is expected to be Parker-like.
- Consider a small region around $\mathbf{\Omega}$ on the photosphere in Figure 4.1, say to the second footpoint trajectory that is drawn. Within this region the footpoint speeds are relatively slow and the consequent field is Parker-like. The corresponding footpoint trajectory on the SS encloses $\mathbf{\Omega}$. In the stationary observer's frame, a small region around $\mathbf{\Omega}$ remains covered by this Parker-like region. Since the hybrid field model describes the time-average behaviour of the PCH, it is plausible to assume that the field approaches a Parker field toward $\mathbf{\Omega}$ on the SS. This behaviour can be modelled by forcing the footpoint velocities to become zero at $\mathbf{\Omega}$ on the SS.
- Considering the large-scale diffusion on the photosphere, differential rotation dominates all other diffusion processes well inside the PCH and away from $\mathbf{p}$ and $\mathbf{\Omega}$, and a significant Fisk field results from the approximate coherent footpoint motion on the SS. Here, trajectories are expected to have a significant meridional motion.
- Near the boundary on the inside of the PCH, the reconnective diffusion speed on the photosphere starts to dominate the differential rotation speed. The increasing reconnection rate results from a ragged, time-dependent boundary. On the SS this diffusion results in a mixture of a Fisk and Parker field. Trajectories in this region are expected to show less meridional motion than inside PCHs.

- Near the boundary on the outside of the PCH, the direction of reconnection is still influenced by the flux from the PCH. The randomness of the reconnective diffusion increases with distance from the PCH until it is completely random. Here, the trajectories will again become azimuthal and the field Parker-like. As was stated in the preceding discussion, the turbulent nature of the HMF beyond the SS will be neglected. However, this region represents a kind of 'return region' and will be discussed below.
- Closer to and at the rotational equator, footpoints on the photosphere rotate rigidly with the equator. Therefore, the motion on the SS can only be diffusive and the field Parker-like.

Toward maximum solar activity, PCHs are known to shrink significantly and to become highly variable (see Section 2.5.2). The number of active regions also increases with solar activity and therefore the amount of diffusion is expected to increase, thereby creating larger and more turbulent PCH boundaries. These two properties indicate that diffusion dominates inside PCHs during solar maximum conditions and only a very small or insignificant Fisk effect is expected. In Section 4.6.1 it is noted that the large number of non-polar CHs in the polar regions during solar maximum may result in a somewhat Fisk-like field, but this will probably not be observed due to the highly dynamic field during these conditions.

A fully analytic model to map what is happening on the photosphere to what happens on the SS is beyond the scope of this study. Given the complexity of the actual PCHs, this is a daunting task. The aim of the present study is to construct a velocity field for the footpoints on the SS which *simulates* the effect of whatever occurs on the photosphere, and is subsequently transferred to the SS, thus affecting the structure of the HMF.

5.2.3 Comment on the Divergence-Free Nature of the Footpoint Velocity Field

Given the fact that magnetic field footpoint motion in the 'return region' near the rotational equator is purely diffusive in the current model, the question arises whether the footpoint velocity field can be divergence-free, since the trajectories are not closed over the whole of the SS. The answer is that when a field line leaves the PCH, another one enters at another location such the magnetic flux leaving the PCH is equal to the flux entering it.

The interaction of the different kinds of the footpoint motion (coherent and diffusive) on the SS can be explained by means of the following analogy, illustrated in Figure 5.1. Consider a container filled with water, and a curved pipe in the container through which the water flows by means of some unspecified mechanism. The pipe represents the region of coherent motion due to the PCH and the container represents the region of the SS where diffusive motion dominates. The behaviour of each water droplet is analogous to the behaviour of an individual magnetic footpoint. Throughout the whole container each water droplet is subject to random diffusive motion. Now consider a certain droplet inside the container at a position not far from

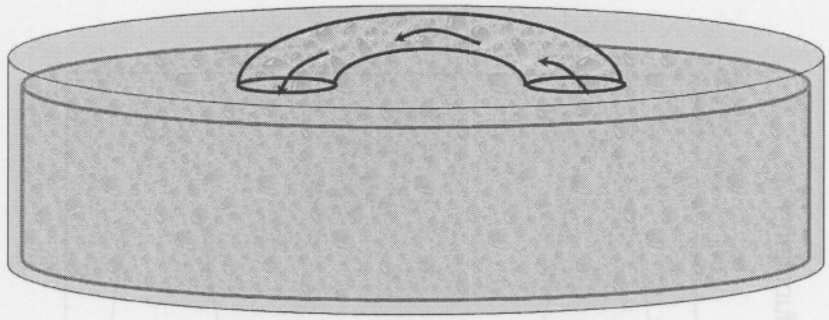

Figure 5.1: A simplistic analogy of the effect of diffusion on the SS footpoints toward the PCH boundaries according to the Fisk-Parker hybrid field.

the point of inflow into the pipe. The droplet diffuses randomly until it is close enough to the pipe to be sucked into it. In the vicinity of this endpoint, conservation of flux results in a stream flowing into the pipe. This flow dominates the random diffusive motion. At the other end of the pipe the opposite process occurs.

Evidently, it is highly improbable that a certain droplet which leaves the pipe will immediately diffuse around the pipe to the exact location of entrance, even if circulation through the container occurs. Conservation of flux does not imply that every droplet traces out a closed trajectory, but only describes the condition that when one droplet leaves the one end of the pipe, another droplet has to enter at the other end.

5.3 The Refined Fisk-Parker Hybrid HMF Equations

The equations that describe an HMF which is frozen into the solar wind follow from the corresponding footpoint velocity field on the SS. In order to obtain a more realistic HMF, the effects of the diffusion have to be included in the velocity field. The expected properties of the velocity field in Section 5.2.2 can be simulated by means of the transition function

$$F_S = \begin{cases} \{\tanh[\delta_p\theta] + \tanh[\delta_p(\theta-\pi)] - \tanh[\delta_e(\theta-\theta'_{rr})]\}^4 & \text{if } \theta \in [0, \theta'_{rr}); \\ 0 & \text{if } \theta \in [\theta'_{rr}, 180^\circ - \theta'_{rr}]; \\ \{\tanh[\delta_p\theta] + \tanh[\delta_p(\theta-\pi)] - \tanh[\delta_e(\theta-\pi/2-\theta'_{rr})]\}^4 & \text{if } \theta \in (180^\circ - \theta'_{rr}, 180^\circ], \end{cases} \tag{5.1}$$

which is illustrated in Figure 5.2. This function is similar to the one used by *Burger and Hitge* [2004], as discussed in Section 4.11.

Physically, the field originating from inside a PCH is Fisk-like, and here $F_S > 0$. Toward the poles and the rotational equator, the field becomes Parker-like and F_S becomes zero. Moreover, since the transition from the dominating mechanism of differential rotation to diffusion being dominant is not abrupt, the transition between the Fisk-like and Parker-like fields occurs gradually. The return region boundary in the Fisk-Parker hybrid field is defined by the

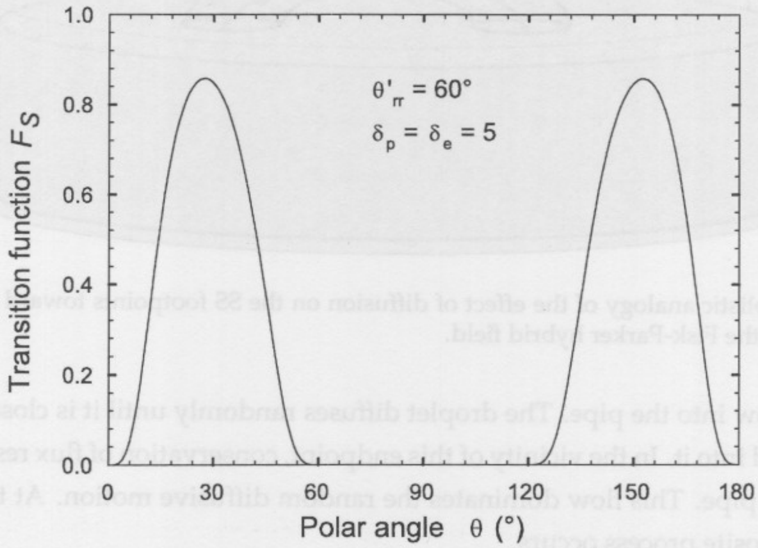

Figure 5.2: The transition function as function of polar angle that is implemented into the velocity field in order to transform the Fisk field to a Parker field at the solar poles and outside the PCH. Here it is assumed that the influence of the Fisk field extends to a polar angle of 60°.

heliographic polar angle θ'_{rr} in Equation (5.1). Beyond this angle, reconnection is completely random and the magnetic field becomes a Parker field.

The PCH boundary on the SS, θ'_b, can be assumed to be the polar angle where $|dF_S/d\theta|$ from within the PCH to the outside is a maximum. Then, from Figure 5.2, $\theta'_b \sim \theta'_{rr} - 10°$ seems a reasonable choice.

The velocity field of *Burger and Hitge* [2004] must be modified in order to reflect the refinements discussed above. For the purpose of the present study it is assumed that the Parker field is unaffected by differential rotation. Therefore both the angle β and the differential rotation rate ω must tend to become zero where the field is Parker-like, or equivalently, in the hybrid field model they must scale with F_S. These parameters are therefore multiplied by F_S to give the effective latitude-dependent functions

$$\begin{aligned} \beta^*(\theta) &= \beta F_S(\theta) \\ \omega^*(\theta) &= \omega F_S(\theta), \end{aligned} \tag{5.2}$$

where β and ω have constant values.

Note that, in order for the velocity field to be divergence-free, the only constraint on F_S once again is that it must only depend on θ. The new divergence-free velocity field for the refined Fisk-Parker hybrid magnetic field in the co-rotating frame is given by

$$\begin{aligned} u_\theta &= r\omega^* \sin\beta^* \sin\phi_\Omega \\ u_\phi &= r\omega^* \sin\beta^* \cos\theta \cos\phi_\Omega + r\omega^* \cos\beta^* \sin\theta \\ &+ r\frac{d\omega^*}{d\theta} \sin\beta^* \sin\theta \cos\phi_\Omega + r\omega^* \frac{d\beta^*}{d\theta} \cos\beta^* \sin\theta \cos\phi_\Omega, \end{aligned} \tag{5.3}$$

and the resulting components of the divergence-free Fisk-Parker hybrid magnetic field in the fixed observer's frame are

$$\begin{aligned}
B_r &= A\left(\frac{r_0}{r}\right)^2 \\
B_\theta &= B_r\frac{r}{V_{sw}}\omega^* \sin\beta^* \sin\phi^* \\
B_\phi &= B_r\frac{r}{V_{sw}}\Big[\omega^* \sin\beta^* \cos\theta \cos\phi^* + \sin\theta(\omega^* \cos\beta^* - \Omega) \\
&\quad + \frac{d\omega^*}{d\theta}\sin\beta^* \sin\theta \cos\phi^* + \omega^*\frac{d\beta^*}{d\theta}\cos\beta^* \sin\theta \cos\phi^*\Big],
\end{aligned} \tag{5.4}$$

where $\phi^* = \phi + \frac{\Omega(r-r_{SS})}{V_{sw}}$.

5.4 Footpoint Velocities in the Fisk-Parker Hybrid Model

Figure 5.3 illustrates the speed distribution of the SS footpoints on a contour graph as function of the heliographic polar angle θ and azimuthal angle ϕ, calculated from Equation (5.3). Parameters are $\delta_e = 4$, $\delta_p = 5$, $\beta = 30°$, and $\theta'_{rr} = 60°$. Similar to Figures 4.4 and 4.5 for the Fisk field, the **p**-axis is located at $(\theta, \phi) = (30°, 180°)$ and a SS radius of $r_{SS} = 10\ r_\odot$ is assumed. This figure differs significantly from the corresponding Figure 4.5 for the Fisk field. At the poles and beyond $\theta = 60°$, the footpoints become stationary due to the scaling of F_S. Toward the **p**-axis, the speeds approach zero due to the connection with the polar region on the photosphere. Two maxima occur, at approximately $(\theta, \phi) = (19°, 0°)$ and $(\theta, \phi) = (46°, 180°)$, and the speed at mid-latitudes varies with the rotation period of the sun.

Figure 5.4 shows the SS footpoint trajectories resulting from the velocity field equations (5.3) for the values used in Figure 5.3. The trajectories are in agreement with what is expected. Near the solar pole the trajectories become distorted due to the influence of diffusion. Similar to Figures 4.6 and 4.9, the direction of the footpoints is clockwise on the left-hand side and anticlockwise on the right-hand side of the figure. The trajectories at $\theta'_{rr} = 60°$ define the boundary of the influence region of the PCH. Beyond this angle, random reconnective diffusion totally dominates and no trajectories are present.

5.5 Resolving Two Restrictions of the Fisk Model

5.5.1 The Return Region

Since random reconnective diffusion takes over outside the PCH, the concept of a 'return region', in which the average reconnection is directed around the PCH, fades. Mathematically, a 'return region' exists in order to obtain the divergence-free trajectories as illustrated in Figures 4.9 and 5.4. However, the physical interpretation is that randomly directed reconnection rather exists in this region and therefore no preferred direction is expected.

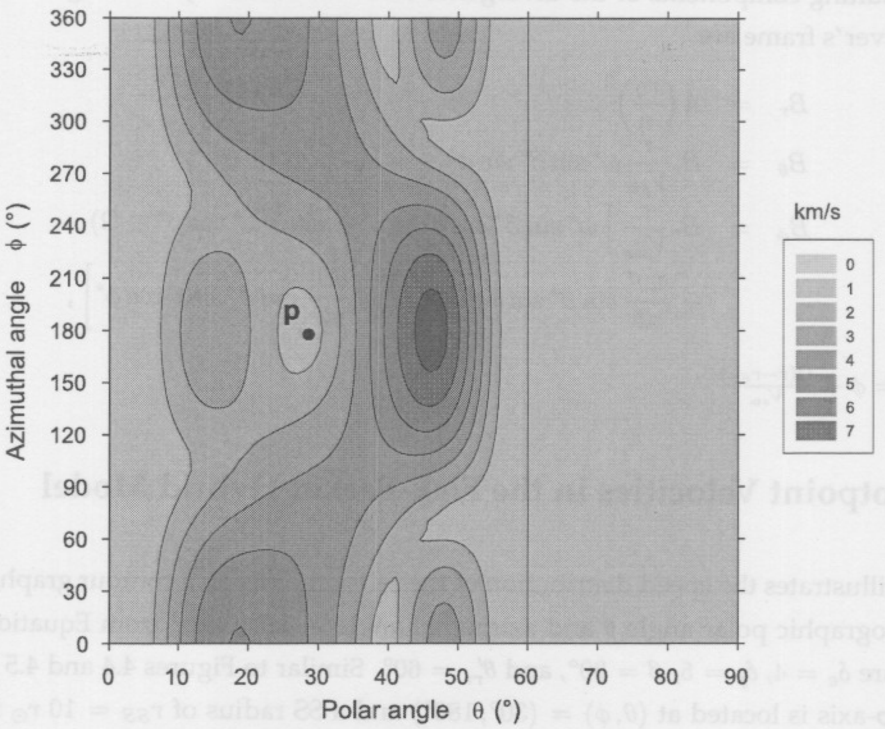

Figure 5.3: A contour graph that represents the footpoint speed distribution in the PCH on the source surface, assumed to be at a radial distance $r_{SS} = 10\, r_\odot$. The p-axis is located at $\theta = \beta = 30°$ and $\phi = 180°$, and a constant heliographic boundary at $\theta'_{rr} = 60°$ is assumed.

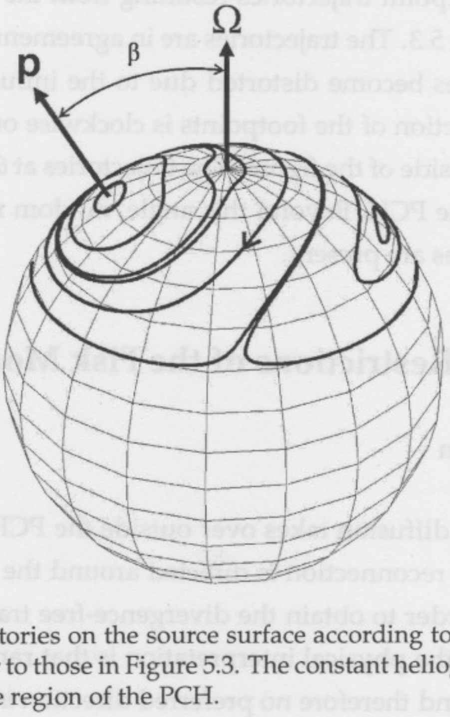

Figure 5.4: The footpoint trajectories on the source surface according to the refined Fisk-Parker hybrid field. The conditions are similar to those in Figure 5.3. The constant heliographic polar angle of $\theta'_{rr} = 60°$ is the boundary of the influence region of the PCH.

5.5.2 PCH Boundaries

The time-dependent behaviour of realistic PCH boundaries, as well as other CH boundaries, can be predicted reasonably accurately by means of numerical MHD models [see, e.g., *Wang and Sheeley*, 1990]. In order to obtain time-dependent models of the Fisk field, connection to these models is needed. However, the Fisk model only describes the average behaviour of the HMF due to the processes beneath the SS. Therefore, the regular, steady boundaries that are used by *Fisk* [1996] is a simplification. However, the hybrid field model is able to simulate the average effect of these uneven, time-dependent boundaries reasonably well by incorporating the transition function F_S into the Fisk HMF (see Section 5.3).

5.6 Toward Modelling a Complete Solar Activity Cycle

In this section the *qualitative* properties of PCH boundaries on the photosphere and SS are investigated in order to construct a simple, zeroth-order model of the long-term behaviour of the PCH size in a quasi-stable, rotating dipole field with two identical polarity periods of 11 years. The resulting PCH boundaries are then transformed to magnetic coordinates in order to calculate β from Equation (4.8). Since β depends on α, as well as on the angles subtended by the PCH boundary on both the photosphere and SS, it changes significantly with solar activity. Furthermore, the transition function, F_S, depends on the SS boundary of the PCH through the angle θ_{rr} [see Eq. (5.1)]. The functions β^* and ω^* in Equation (5.2) therefore depend explicitly on the solar activity. These functions are then substituted in the velocity and magnetic field equations of the Fisk-Parker hybrid field in order to describe a heliospheric magnetic field which depends on solar activity. When the resulting field is used in the numerical modulation model in Chapter 6, the aim will only be to consider periods of minimum to moderate activity.

As a first step, a function is fitted to the tilt angle data of J. T. Hoeksema (see Fig. 2.16) in order to simulate the time-dependence of solar activity.

Solar activity cycles start and end at successive solar minima and cover a period of $\sim 11 \pm 2$ years (see, e.g., Figures 2.6 and 2.7). In this model, an average period of 11 years is assumed. What is also apparent from Figure 2.6, is that the solar activity increases from a minimum to a maximum within $\sim 4 \pm 1$ years and decreases to the following minimum again in the remaining $\sim 7 \pm 1$ years. The averages of 4 and 7 years, respectively, are used in what follows.

Periodic behaviour can usually be described reasonably well with a single or a few sinusoidal functions. Such a function is convenient to use and a single function turns out to be a reasonable approximation for the average behaviour of the tilt angle α (see Fig. 2.16). The data from Hoeksema reveal that the smallest and largest values of α are approximately 10° and $\gtrsim 75°$, respectively, the latter being a lower limit. While the non-zero value of α may suggest that **M** rotates in a plane which is inclined with respect to the meridional plane by an angle of about 10° it will simply be assumed that α varies between 10° and 80°. Therefore, the tilt angle can be modelled by the following sinusoidal function of the time T of the solar cycle, i.e. T years after solar minimum,

$$\alpha = \begin{cases} \frac{\pi}{4} - (\frac{\pi}{4} - \delta)\cos\left[\frac{\pi}{4}T\right] & \text{if } 0 \leqslant T \leqslant 4; \\ \frac{\pi}{4} - (\frac{\pi}{4} - \delta)\cos\left[\frac{\pi}{7}(T-11)\right] & \text{if } 4 < T \leqslant 11, \end{cases} \tag{5.5}$$

where the angles are expressed in radians, and δ is the minimum offset of $\mathbf{M}$ with respect to $\mathbf{\Omega}$. According to Figure 2.16, $\delta = 10°$ seems to be a reasonable choice.

PCH sizes show a reasonably accurate anti-correlation with the sunspot number (see Fig. 2.12 in Section 2.5.2) and therefore also with α. Since the periods and rates of change of these periodic solar phenomena vary significantly from one solar cycle to the next, the model describes only the average behaviour over several solar cycles. Next, a model of θ_b as function of time is constructed.

5.6.1 Model for the Boundary Angle θ_b on the Photosphere

CHs on the photosphere have been studied extensively by observing soft X-ray, EUV (extreme ultraviolet), infrared and radio images of the photosphere, as well as spectral line absorption at the solar limb (i.e. a few kilometers above the photosphere). Semi-empirical methods are often employed by combining these observations with a PFSS model [see, e.g., *Zhao et al.*, 1999; *Wang and Sheeley*, 1992]. No completely objective and quantitative observational method which can locate CH boundaries unambiguously exists. The construction of soft X-ray images of the solar disk is the most adequate method to define CH boundaries sharply, because of the large contrast between CHs and the ambient plasma [*Hudson*, 2002]. However, quantitative results from other methods agree reasonably well with the results from soft X-ray images, and usually provide additional information. Furthermore, results from the different methods are consistent in most of the qualitative properties of CHs.

Several observational properties of PCHs that were obtained by means of different methods are now investigated in order to obtain feasible information about the PCH boundaries on the photosphere.

- *Waldmeier* [1981] studied the PCHs in the four consecutive solar activity cycles 18–21 during the period from 1940 to 1978 by observing the Fe-16 (530.3 nm) corona line.
- *Webb et al.* [1984] investigated the properties of PCHs between 1964 and 1976. His results were mainly obtained from soft X-ray and EUV images, as well as He I (1083 nm) corona lines.
- *Bravo and Stewart* [1994] used data from K-coronagraph observations at 1.5 $r_\odot$ between 1960 and 1993 for Solar Cycles 20–22.
- *Dorotovic* [1996] investigated PCH data of the five consecutive solar cycles 18–22 during the period from 1939 to 1993 that were obtained from Fe-16 (530.3 nm) line absorption of the solar limb.

- *Fox et al.* [1999] studied the polarity reversal of the northern PCH during Solar Cycle 22 by using He I (1083 nm) line spectroheliograms.

- *Dobrzycka et al.* [1999] studied H I (Lyman α at 121.6 nm), as well as O VI at 103.2 nm and 103.7 nm emission lines of the solar limb near the solar minimum of Solar Cycle 22.

- *Harvey and Recely* [2002] provided data from the two solar cycles 21 and 22, obtained by using He I (1083 nm) line absorption in the chromosphere.

The results from these papers indicate that the behaviour of a PCH during a solar cycle can be divided into four phases.

Phase 1

The initial phase starts immediately after polar reversal during solar maximum when the new-polarity PCH is created from CHs in the polar region which merge and cover the pole. In this phase, the asymmetrical PCH rapidly increases in size and moves into a more stable and symmetric position about the pole. Some authors regard this phase only as a transient phase in which a PCH does not exist [see, e.g., *Waldmeier*, 1981; *Harvey and Recely*, 2002]. The PCH disappears completely when this phase starts and suddenly appears again as soon as the hole becomes stable at the pole, announcing the beginning of the next phase. Other authors define the PCH as any CH that completely or partly covers the solar pole, independent of its form and size, [see, e.g., *Dorotovic*, 1996; *Bravo and Stewart*, 1994]. The PCH then gradually grows and becomes stable about Ω within approximately 1 to 2 years. Data from *Dorotovic* [1996] and *Bravo and Stewart* [1994] reveal that the average minimum area constitutes about 1% of the photosphere. This is equivalent to a PCH symmetrical about Ω, with its radius, θ_b, subtending a polar angle of about 8°. The new-polarity CH at the beginning of this phase may even be larger at the time when the hole starts to move over the pole [see, e.g., *Fox et al.*, 1999].

As soon as the stable, axisymmetrical state is reached at the end of this phase, $\theta_b > 20°$ according to *Waldmeier* [1981]. *Harvey and Recely* [2002] obtained even larger values, viz. $\theta_b \approx 22° - 27°$. According to *Dorotovic* [1996], *Bravo and Stewart* [1994] and *Wang and Sheeley* [1990], the PCH covers an area of about 4% – 6% of the photosphere after 2 years, i.e. $\theta_b \approx 20°$. From these results, an average value of $\theta_b = 20°$ seems reasonable. The CHs that have merged at the pole and developed into the more stable PCH are directly connected to this PCH and therefore have similar properties. Even if the combination of these asymmetrical CHs is not defined as a PCH, the global magnetic field from the CHs is qualitatively similar to the field from an axisymmetrical PCH about Ω, extending to $\theta_b \approx 20°$.

The period of the first phase varies between 1.2 to 1.4 years according to *Harvey and Recely* [2002], 0.5 to 1.5 years according to *Webb et al.* [1984] and may even exceed 2 years according to *Waldmeier* [1981] and data from *Dorotovic* [1996]. An average period of 2 years will be used.

Phase 2

When the PCH reaches a stable, axisymmetrical state, the second phase starts. The PCH grows gradually within a period of about 5 to 7 years and reaches a maximum size at solar minimum. *Waldmeier* [1981] observed an average value $\theta_b \approx 30°$ at solar minimum and $\theta_b > 40°$ for more than six consecutive years in both Solar Cycles 20 and 21. *Dorotovic* [1996] and *Bravo and Stewart* [1994] obtained an average maximum photospheric area of approximately 10% and 13%, respectively. This is consistent with an axisymmetrical PCH with $\theta_b \approx 26°$ and $\theta_b \approx 30°$, respectively. *Harvey and Recely* [2002] found that $\theta_b \approx 31° - 32°$, while *Dobrzycka et al.* [1999] observed $\theta_b \lesssim 30°$ with an average value of about 23°. A typical value of $\theta_b = 30°$ at the end of the second phase seems reasonable.

Phase 3

In the third phase the PCH area decreases from a maximum value at solar minimum activity to a minimum value a few months before the polarity reversal at solar maximum. Near the end of the phase, CHs start to fragment from the PCH. A few months prior to polarity reversal the PCH shrinks rapidly. The period of this phase is $\sim$ 4 years.

Phase 4

The final phase is the period before polarity reversal between the fragmentation of the old-polarity PCH and the formation of the new-polarity PCH. During this period, several CHs exist around the solar pole, but none of them covers the pole completely. The new-polarity CH usually only touches the pole [see, e.g., *Fox et al.*, 1999]. At the instant a part of this CH starts to cover the pole, the new polarity PCH is created and the first phase starts. Some authors, e.g. *Webb et al.* [1984], *Fox et al.* [1999] and *Dorotovic* [1996], observed a period of only a few months for the final phase. From Waldmeier's observations, a period of 1 to 2 years can be deduced. Such a period corresponds to the results of *Harvey and Recely* [2002] who observed the holes in the northern (southern) hemisphere to disappear about 1.1 (1.8) years before polarity reversal. A typical period of 1 year for the last phase seems reasonable. Similar to Phase 1, there is not conformity as to whether the CH in this phase should be regarded as a PCH.

Discussion

Before functions for the boundary angles are constructed, a comment about the relationship between the dipolar magnetic field and the observed behaviour of the PCH boundaries needs to be made. The observation that the solar poles are (almost) permanently covered with PCHs and that the polarity reversal is a rapid process which occurs during Phase 4 may seem not to coincide with the theory of a rotating dipolar magnetic field [see, e.g., *Smith*, 2001]. However, the large-scale photospheric field is only a rotating dipole to a first order approximation during the whole solar activity cycle (cf. Section 3.4). Note that it is possible that this approximately dipolar field may rotate such that the rotation plane of **M** is offset from the meridional plane, as mentioned in the discussion preceding Equation (5.5). Furthermore, the higher-order terms become significant during high activity periods as the result of the large toroidal field components (see Section 2.4.3). These perturbations significantly affect the behaviour of the PCHs and is simulated in this model by varying the PCH size. This behaviour of the PCHs is then combined with a dipolar field approximation.

When the CH in Phases 1 and 4 is not regarded as a PCH, the average lifetime of the PCH is the sum of the periods of Phases 2 and 3. *Harvey and Recely* [2002] obtained an average lifetime of 8.3 and 8.7 years for the northern and southern PCHs, respectively, in Solar Cycles 21 and 22. This is consistent with the results of *Waldmeier* [1981], which show a total period of approximately 2 to 3 years in which no PCH exists and thus an average lifetime of about 8 to 9 years. The effect produced by the high-latitude CHs during solar maximum is similar to that of a PCH in Phases 1 and 4. However, when the Fisk field from these CHs is dominated by diffusion, the net effect is still a PCH which vanishes during these two phases.

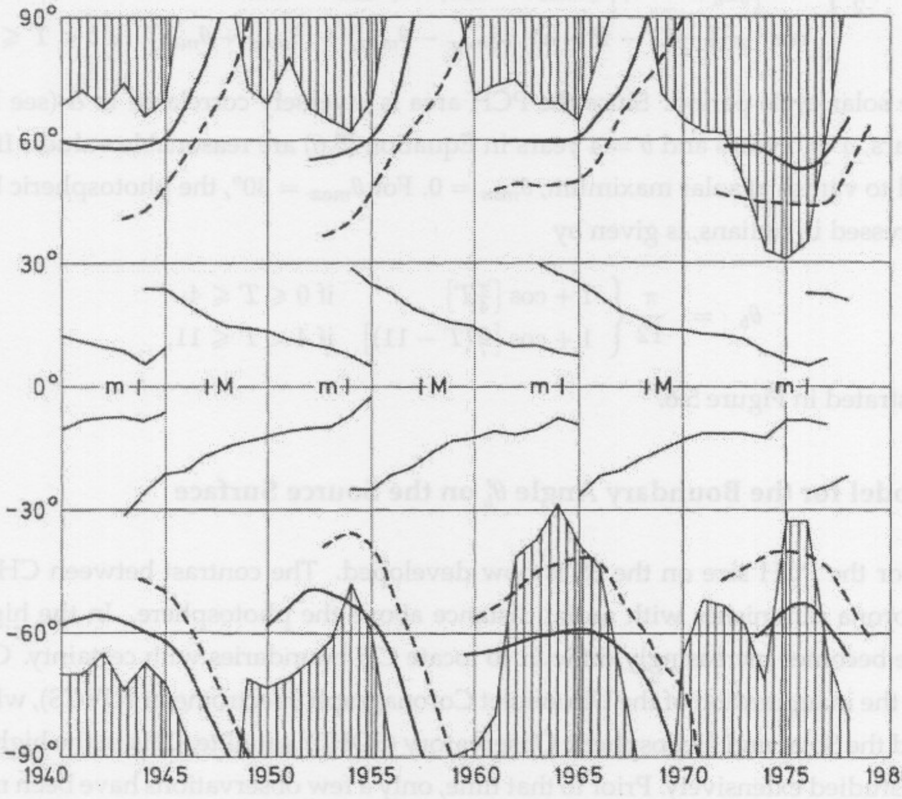

Figure 5.5: The extension of the polar coronal holes from 1940 to 1978. The areas inside the holes are shown by hatching. The maxima (M) and minima (m) of the sunspot numbers are marked by the vertical bars [*Waldmeier*, 1981].

The observed behaviour of the photospheric PCH boundary is illustrated in Figures 5.5 [*Waldmeier*, 1981] and 2.12. Figure 5.5 assumes a PCH that vanishes during Phases 1 and 4, and gives the annual averaged polar angle of both the northern and southern PCH boundary. In Figure 2.12, a non-vanishing PCH during the whole solar cycle is assumed, and the variation of the PCH area is considered.

In this model, the PCH area is assumed to change from solar minimum to maximum and back to minimum by sinusoidal functions. These functions are assumed to be similar to the standard form that was used by *Snodgrass* [1983] to fit the observed rotation rate of the photosphere (see Section 2.3). The angle θ_b can then be described by a sinusoidal function of the time T of the solar cycle to a first-order approximation. *Fisk et al.* [1999a] also expressed the maximum boundary angle on the SS by a sinusoidal function (see Section 4.7). However, the function they used does not vary smoothly through solar minimum, i.e. when γ decreases to zero and increases again (see Fig. 4.7).

Let θ_{max} and θ_{min} denote the maximum and minimum values of θ_b, which are attained at a and b years after solar minimim, respectively. A general sinusoidal function for θ_b is then given by

$$\theta_b = \frac{1}{2}\begin{cases} \cos\left[\frac{\pi}{P-b+a}(T-a)\right](\theta_{max}-\theta_{min})+(\theta_{max}+\theta_{min}) & \text{if } 0 \leqslant T \leqslant a; \\ \cos\left[\frac{\pi}{b-a}(T-a)\right](\theta_{max}-\theta_{min})+(\theta_{max}+\theta_{min}) & \text{if } a < T \leqslant b; \\ \cos\left[\frac{\pi}{P-b+a}(T-P-a)\right](\theta_{max}-\theta_{min})+(\theta_{max}+\theta_{min}) & \text{if } b < T \leqslant P, \end{cases} \quad (5.6)$$

with P the solar cycle period. Since the PCH area is inversely correlated to α (see Fig. 2.12), $P = 11$ years, $a = 0$ years and $b = 4$ years in Equation (5.6) are reasonable values. If the PCH is assumed to vanish at solar maximum, $\theta_{min} = 0$. For $\theta_{max} = 30°$, the photospheric boundary angle, expressed in radians, is given by

$$\theta_b = \frac{\pi}{12}\begin{cases} 1+\cos\left[\frac{\pi}{4}T\right] & \text{if } 0 \leqslant T \leqslant 4; \\ 1+\cos\left[\frac{\pi}{7}(T-11)\right] & \text{if } 4 < T \leqslant 11, \end{cases} \quad (5.7)$$

and is illustrated in Figure 5.6.

5.6.2 Model for the Boundary Angle θ_b' on the Source Surface

A model for the PCH size on the SS is now developed. The contrast between CHs and the ambient corona diminishes with radial distance above the photosphere. In the high corona it therefore becomes increasingly difficult to locate CH boundaries with certainty. Only since 1996, after the inauguration of the Ultraviolet Coronagraph Spectrometer (UVCS), which operates aboard the Solar and Heliospheric Observatory (SOHO) satellite, CHs in the higher corona have been studied extensively. Prior to that time, only a few observations have been made. The first qualitative results of PCH expansion were obtained by theoretical models.

Results from Semi-Empirical Models and Direct Observations

The expansion (or spreading) factor, $f(r)$, was introduced by *Kopp and Holzer* [1976] to describe the superradial expansion of field lines within a PCH. The area of a circle of radius r at a polar angle θ in the geometry of the surface of a sphere is given by $A(r) = 2\pi r^2(1-\cos\theta)$. Let $f(r)$ denote the factor by which the area of an axisymmetrical PCH at radius r is larger than its area on the photosphere, $A(r_\odot)$, due to superradial expansion. Then the ratio of the cross-sectional areas of the axisymmetrical PCH at r and $r_\odot$, respectively, is given by

$$\frac{A(r)}{A(r_\odot)} = \frac{1-\cos[\theta(r)]}{1-\cos[\theta(r_\odot)]}\left(\frac{r}{r_\odot}\right)^2 \tag{5.8}$$

Hence,

$$A(r) = A(r_\odot)\left(\frac{r}{r_\odot}\right)^2 f(r), \tag{5.9}$$

where

$$f(r) = \frac{1-\cos\theta(r)}{1-\cos\theta(r_\odot)} \tag{5.10}$$

for a PCH with a boundary at polar angle $\theta(r)$ at radial distance r.

The factor $f(r)$ increases with height and converges to a maximum value f_{max} when $r \to \infty$. Following the definition of the SS, $f_{max} = f(r_{SS})$ at the SS radius r_{SS}. Since $\theta_b = \theta(r_\odot)$, the corresponding value

$$\theta_b' = \theta(r_{SS}) = \cos^{-1}\left[1 - f_{max}(1-\cos\theta_b)\right] \tag{5.11}$$

can easily be calculated if f_{max} is known.

Polar plumes, which are discussed in Section 2.5.4, serve as useful tracers for CHs. These features can be observed in white light, EUV and soft X-rays [see, e.g., *DeForest et al.*, 1997; *Suess et al.*, 1998]. They grow superradially and rapidly with height, increasing their subtended solid angle by a factor of ~ 10 from the photosphere to $\sim 5\ r_\odot$, and by a total factor of more than 40 at large radial distances from the sun, i.e. $f(r) = 10$ and 40, respectively, at these distances. *Kopp and Holzer* [1976] obtained an almost constant expansion factor of nearly 7.5 beyond 2.5 $r_\odot$ at solar minimum, i.e. $f_{max} \approx 7.5$. However, substituting this value as well as $\theta_b = 30^\circ$ in Equation 5.11 yields the unphysical value $\theta_b' \approx 90.3^\circ$. More realistic theoretical models of coronal field configurations contain a PFSS or a current sheet model, such as those developed by *Wang and Sheeley* [1990], whose results are consistent with observations. Using such a model, *DeForest et al.* [1997] obtained the values $\theta_b \approx 25^\circ$ and $\theta_b' > 75^\circ$ for the PCH near the minimum of Solar Cycle 22. *Suess et al.* [1998] used some empirical constraints provided by polar plumes to develop a detailed theoretical model of the PCH expansion during low solar activity conditions. His results are consistent with those of *DeForest et al.* [1997].

Munro and Jackson [1977] were among the first to obtain reliable quantitative observational results for $f(r)$ from optical coronagraph images. The transition from subsonic to supersonic flow was observed below 3 $r_\odot$, as predicted by *Kopp and Holzer* [1976]. Above $\sim 3\ r_\odot$, the expansion of the field lines became essentially radial with $\theta_b' \approx 65 \pm 5^\circ$.

After processing the UVCS/SOHO standard observational results of both PCHs during the activity minimum of Solar Cycle 22, *Dobrzycka et al.* [1999] derived values for f_{max} ranging from 6.0 to 7.5, with an average value of 6.9. Approximate values of θ_b' range from 60° to 82° with an average value of 63.7° and a typical value of 66°.

A self-consistent, semi-empirical model, which is able to describe several plasma parameters in the extended solar corona above a PCH, was developed by *Cranmer et al.* [1999] by combining the UVCS/SOHO observations with the model of *Kopp and Holzer* [1976]. Using $\theta_b = 28°$, the value $\theta'_b \approx 76° \pm 6°$ is obtained. This indicates that the PCH intersects a large part of the streamer belt (see Section 2.6). They show that their results are consistent with several other papers.

Since CHs are associated with the high-speed solar wind, much information can be obtained by using the wind as a tracer. From the solar wind speed profile at solar minimum (see Fig. 2.19), it is evident that the fast wind fills the whole region from the solar poles to a latitude of about 23° at solar minimum. Following, e.g., *Gosling et al.* [1995] and *McComas et al.* [1998], who assume that all fast wind streams originate from PCHs, and by assuming that the solar wind speed profile is similar to Figure 2.19 at the SS, PCHs are known to cover approximately 61% of the SS, i.e. $\theta'_b \approx 67°$. The ragged boundary of a PCH and extensions thereof to lower latitudes contribute significantly to the fluctuations in the streamer belt. An even larger average PCH boundary can therefore be assumed in order to include this effect.

Interpretation and Remarks

Considering all the above-mentioned results, a plausible range for θ'_b at solar minimum is from about 60° to 80° and a reasonable value to assume is $\sim 70°$. In order to optimise the effect of the Fisk field, the maximum value, viz. $\theta'_b = 80°$, can be used.

Suggestions have been made by, e.g., *Burlaga et al.* [1978] and *Hu et al.* [2003], that the regions outside CHs may also contribute to the fast wind streams in the heliosphere, even as much as 50% during solar minimum conditions. This will result in a much smaller PCH. However, comparing the PCH size with the other observational results, a PCH that covers the whole fast wind region, or even larger, seems reasonable.

Some information about the PCHs can be inferred from observational results and predictions of the fast solar wind behaviour. In Section 2.6 it is noted that the streamer belt broadens significantly with solar activity, implying that the PCH shrinks accordingly. From Figure 2.22 it is evident that the fast solar wind occurs below a latitude of 35° only during solar minimum conditions. Furthermore, during solar maximum conditions, this latitude is entirely covered by the slow wind and θ'_b therefore has to be significantly smaller than 55°.

The largest constraint on θ'_b in the current model is that the PCH is enclosed between Ω and the tilted magnetic equator. This constraint is significant for periods away from solar minimum conditions and is given by

$$\theta'_b + \alpha < 90°. \tag{5.12}$$

An optimal, but realistic Fisk effect can be obtained by assuming that θ'_b develops similar to θ_b and by using the observational results in this section as boundary values for θ'_b. A general function for θ'_b is then given by

$$\theta'_b = \frac{1}{2}\left\{\begin{array}{ll} \cos\left(\frac{\pi}{4}T\right)(\theta'_{max}-\theta'_{min})+(\theta'_{max}+\theta'_{min}) & \text{if } 0 \leqslant T \leqslant 4; \\ \cos\left[\frac{\pi}{7}(T-11)\right](\theta'_{max}-\theta'_{min})+(\theta'_{max}+\theta'_{min}) & \text{if } 4 < T \leqslant 11. \end{array}\right. \quad (5.13)$$

5.6.3 Modelling β for a Complete Solar Cycle

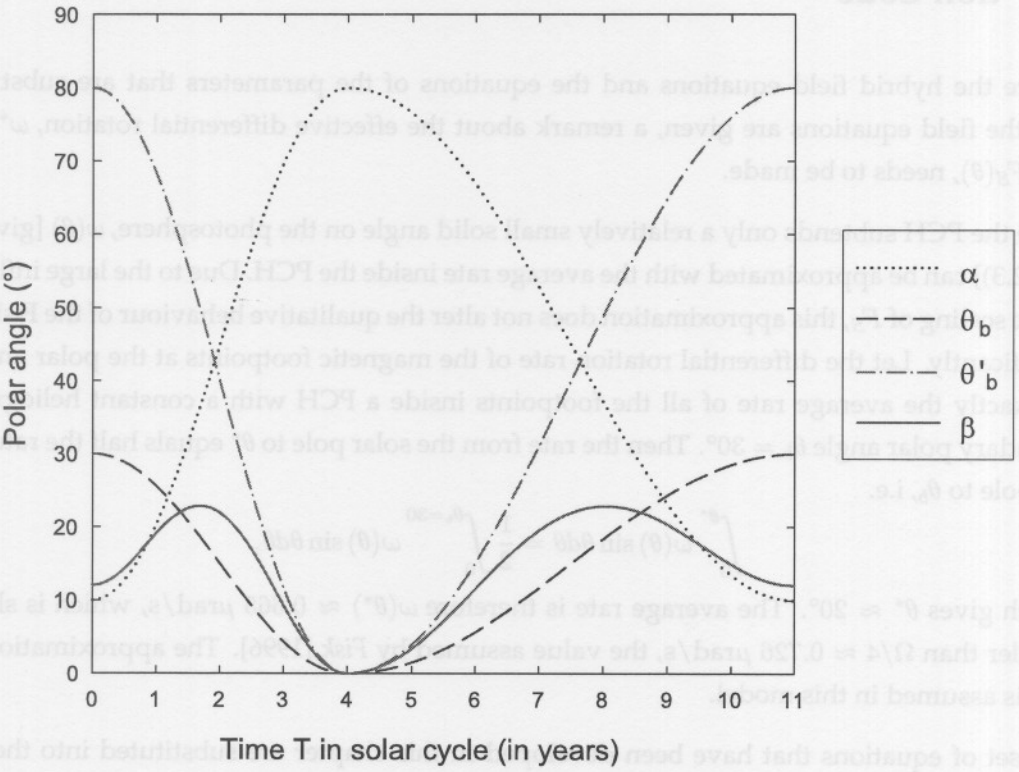

Figure 5.6: A simple model which describes the behaviour of the parameters α, θ_b, θ'_b and β during a complete solar cycle for a PCH in the hybrid model that vanishes at the polarity reversal. A symmetry about Ω on the SS is assumed.

As discussed in Section 5.6.2, an optimal value for θ'_{max} is 80°. A PCH which continually shrinks with solar activity and eventually disappears at solar maximum is assumed. Then $\theta'_{min} = 0°$ and an optimal function for θ'_b is given by

$$\theta'_b \;=\; \frac{2}{9}\pi\left\{\begin{array}{ll} 1+\cos\left[\frac{\pi}{4}T\right] & \text{if } 0 \leqslant T \leqslant 4; \\ 1+\cos\left[\frac{\pi}{7}(T-11)\right] & \text{if } 4 < T \leqslant 11, \end{array}\right. \quad (5.14)$$

and is illustrated in Figure 5.6. This function obeys the constraint of Equation (5.12) at all T, preventing the PCH to cross the magnetic equator. From Equations (5.5), (5.7) and (5.14) for α, θ_b and θ'_b, respectively, β can easily be calculated from Equation (4.8). Figure 5.6 shows the behaviour of the parameters α, θ_b, θ'_b and β, all as function of T, for the whole solar cycle. The angle β increases from 12.0° to 22.9° within 2 years and then decreases to zero at solar maximum, suggesting that the strongest signature of the Fisk field is present during moderate solar activity conditions, and then vanishes toward solar maximum conditions. During the declining phase, the inverse occurs. Note that the boundary values, as well as the value of β when $\alpha = 15°$, do not correspond to the values used by *Fisk* [1996], due to the significant difference in symmetry between the two models.

5.7 The Hybrid Magnetic Field Equations in the Numerical Modulation Code

Before the hybrid field equations and the equations of the parameters that are substituted into the field equations are given, a remark about the effective differential rotation, $\omega^*(\theta) = \omega(\theta)F_S(\theta)$, needs to be made.

Since the PCH subtends only a relatively small solid angle on the photosphere, $\omega(\theta)$ [given by Eq. (2.3)] can be approximated with the average rate inside the PCH. Due to the large influence of the scaling of F_S, this approximation does not alter the qualitative behaviour of the Fisk field significantly. Let the differential rotation rate of the magnetic footpoints at the polar angle θ^* be exactly the average rate of all the footpoints inside a PCH with a constant heliographic boundary polar angle $\theta_b = 30°$. Then the rate from the solar pole to θ^* equals half the rate from the pole to θ_b, i.e.

$$\int_0^{\theta^*} \omega(\theta)\sin\theta d\theta = \frac{1}{2}\int_0^{\theta_b=30} \omega(\theta)\sin\theta d\theta, \tag{5.15}$$

which gives $\theta^* \approx 20°$. The average rate is therefore $\omega(\theta^*) \approx 0.665$ μrad/s, which is slightly smaller than $\Omega/4 \approx 0.726$ μrad/s, the value assumed by *Fisk* [1996]. The approximation $\omega = \Omega/4$ is assumed in this model.

The set of equations that have been developed in this chapter are substituted into the Fisk-Parker hybrid magnetic field equations which are implemented in the numerical modulation model, described in the next chapter. The divergence-free hybrid magnetic HMF is described by

$$\begin{aligned}
B_r &= A\left(\frac{r_0}{r}\right)^2 \\
B_\theta &= B_r \frac{r}{V_{sw}} \omega^* \sin\beta^* \sin\phi^* \\
B_\phi &= B_r \frac{r}{V_{sw}} \Big[\omega^* \sin\beta^* \cos\theta \cos\phi^* + \sin\theta(\omega^* \cos\beta^* - \Omega) \\
&\quad + \frac{d\omega^*}{d\theta} \sin\beta^* \sin\theta \cos\phi^* + \omega^* \frac{d\beta^*}{d\theta} \cos\beta^* \sin\theta \cos\phi^* \Big],
\end{aligned} \tag{5.16}$$

where $\phi^* = \phi + \frac{\Omega(r - r_{SS})}{V_{sw}}$.

The effective latitude-dependent functions β^* and ω^* are given by

$$\begin{aligned}
\beta^*(\theta) &= \beta F_S(\theta) \\
\omega^*(\theta) &= \omega F_S(\theta),
\end{aligned} \tag{5.17}$$

where $\omega = \Omega/4$ is the average differential rotation rate of the photospheric PCH, β is a constant value well inside the PCH at a certain solar activity state and

$$F_S = \begin{cases} \{\tanh[\delta_p\theta] + \tanh[\delta_p(\theta - \pi)] - \tanh[\delta_e(\theta - \theta'_{rr})]\}^4 & \text{if } \theta \in [0, \theta'_{rr}); \\ 0 & \text{if } \theta \in [\theta'_{rr}, 180^\circ - \theta'_{rr}]; \\ \{\tanh[\delta_p\theta] + \tanh[\delta_p(\theta - \pi)] - \tanh[\delta_e(\theta - \pi/2 - \theta'_{rr})]\}^4 & \text{if } \theta \in (180^\circ - \theta'_{rr}, 180^\circ], \end{cases} \tag{5.18}$$

is the transition function, with δ_e and δ_p constants, and θ'_{rr} the largest polar angle on the SS where the Fisk field influences the HMF configuration.

The angles β and θ'_{rr} depend both on the solar activity of the sun. The former is given by

$$\beta = \cos^{-1}\left[1 - (1 - \cos\theta'_{mm})\left(\frac{\sin^2\alpha}{\sin^2\theta_{mm}}\right)\right] - \alpha, \tag{5.19}$$

where $\theta_{mm} = \theta_b + \alpha$ and $\theta'_{mm} = \theta'_b + \alpha$ are the PCH boundary in heliomagnetic coordinates on the photosphere and SS, respectively, with

$$\theta_b = \frac{\pi}{12}\begin{cases} 1 + \cos\left[\frac{\pi}{4}T\right] & \text{if } 0 \leqslant T \leqslant 4; \\ 1 + \cos\left[\frac{\pi}{7}(T - 11)\right] & \text{if } 4 \leqslant T \leqslant 11 \end{cases} \tag{5.20}$$

and

$$\theta'_b = \frac{4}{18}\pi\begin{cases} 1 + \cos\left[\frac{\pi}{4}T\right] & \text{if } 0 \leqslant T \leqslant 4; \\ 1 + \cos\left[\frac{\pi}{7}(T - 11)\right] & \text{if } 4 < T \leqslant 11, \end{cases} \tag{5.21}$$

the heliographic boundary polar angles of the PCH on the photosphere and SS, respectively, at a time T from solar minimum.

The tilt angle is given by

$$\alpha = \frac{\pi}{4} - \left(\frac{\pi}{4} - \delta\right)\begin{cases} \cos\left[\frac{\pi}{4}T\right] & \text{if } 0 \leqslant T \leqslant 4; \\ \cos\left[\frac{\pi}{7}(T - 11)\right] & \text{if } 4 < T \leqslant 11, \end{cases} \tag{5.22}$$

where the angles are expressed in radians, and $\delta = 10^\circ$.

Finally, the value $\theta'_{rr} = \theta'_b + 10^\circ$ is used for F_S.

In the modulation model a heliospheric boundary of 100 AU and a constant solar wind speed $V = V_{sw}$ of 600 km/s at all locations within the model heliosphere are assumed. The magnetic field is normalised to a magnitude of 5 nT at the earth.

5.8 Discussion of the Hybrid Model

In Section 4.6 it is predicted that the Fisk effect depends strongly on latitude and solar activity. The latitude dependence is created by the significant influence of diffusion in and above the photosphere, which dominates outside a PCH, as well as toward the axes Ω and $\mathbf{p}$ and toward the boundary inside a PCH. The effect of diffusion can be described reasonably realistically by the transition function, F_S, as described in Section 5.3. This function scales the Fisk field to a Parker field at the locations where a turbulent magnetic field dominates.

The solar activity dependence is described extensively in Section 5.6. As predicted in Section 4.6, it is found in Section 5.6.3 that the largest Fisk effect occurs during moderate solar activity conditions. During solar minimum, the Fisk field is significantly smaller, but does not vanish when the magnetic axis, $\mathbf{M}$, remains inclined with respect to $\mathbf{\Omega}$. During solar maximum, the presence of quasi-steady non-polar CHs in the polar region may result in a small Fisk field, but within the noise of a turbulent field the Fisk effect is expected not to be observed.

The PCH boundaries on the photosphere and SS are expected to behave qualitatively similarly during the solar activity cycle, being largest during solar minimum and shrinking to either small values or to zero during solar maximum.

The new hybrid model is a first attempt in constructing a model which can simulate the PCH boundaries on the photosphere and SS on average, as well as the net effect of the Fisk field during the whole solar activity cycle. This model constitutes a simple zeroth-order model and is therefore subject to many assumptions and restrictions. The model describes a rotating dipolar magnetic field structure and neglects large perturbations in the field. A realistic field model is much more complicated, since several time-dependent factors need to be considered. In order to derive such a model, a time-dependent model of the CMF is necessary. This can be simulated by constructing a time-dependent transition function that depends on both latitude and longitude at every location on the SS. The contribution of CHs scattered over the whole surface can then be described more realistically. Such a transition function is the next step into a first-order correction of the Fisk-Parker hybrid HMF.

Furthermore, a constant solar wind speed and magnetic field strength is used in the numerical code, as well as the small tilt angle approximation of the HCS in Equation (3.17). In a more realistic model these parameters need to be modified.

5.8.1 Some General Applications of the Hybrid Field

The Probable Field During a Grand Minimum Period

During the four Grand Minima, Oort (1050 AD), Spoerer (1420–1540), Maunder (1645–1715), and Dalton (1810–1820) [see, e.g., *Caballero-Lopez et al.*, 2004], no or only very few sunspots were observed and the solar magnetic field strength remained exceptionally small. This indicates that a very few active regions, and therefore only a very small and negligible toroidal field component, existed during these periods. If regular polarity reversals occurred [see, e.g., *Wang and Sheeley*, 2003] as well as very little magnetic field diffusion due to the low activity level, the result would be an HMF that forms an almost perfect Parker spiral to a pronounced Fisk-type field and back during one cycle. The behaviour of the HMF during such minima is of particular importance for studies that attempt to relate, e.g., ^{10}Be concentration in Antarctic ice [*Moraal et al.*, 2005] to the strength of the field.

The Expected Field in Other Stars

A Fisk-type field is not expected to be generated in all stars. The major factor that determines the type of field is the amount of magnetic field diffusion in and above the photosphere of a star. In stars that are more active than our sun, it is expected that diffusion dominates the differential rotation of the magnetic photospheric footpoints throughout a much longer period of the astro cycle. The expected field configuration from these stars is then rather a turbulent Parker-like field than a Fisk-type field, and may be described by the model of Giacalone [see, e.g., *Giacalone and Jokipii*, 1999; *Giacalone*, 2001; *Giacalone and Jokipii*, 2004].

5.9 Summary

In this chapter a refined Fisk-Parker hybrid magnetic field model was introduced, valid at all latitudes and during all solar activity conditions.

It was shown that a transition function that is implemented in the velocity field of the hybrid HMF simulates the latitude dependence of the Fisk effect. It was found that the total Fisk effect first increases with solar activity, attains a maximum during moderate solar activity periods and then decreases until no effect is expected at solar maximum. During the declining activity phase the Fisk effect increases to the same maximum and then decreases gradually again toward solar minimum.

The Fisk effect can in principle be tested for by investigating both the global and local effect of the hybrid HMF on cosmic rays in the heliosphere. A model which describes the modulation of cosmic rays in the heliosphere is developed in the next chapter and this model is then used to investigate the influence of the hybrid field on cosmic rays.

importance for studies that attempt to relate, e.g., ^{10}Be concentration in Antarctic ice [*Moraal et al.*, 2005] to the strength of the field.

The Expected Field in Other Stars

A Fisk-type field is not expected to be generated in all stars. The major factor that determines the type of field is the amount of magnetic field diffusion in and above the photosphere of a star. In stars that are more active than our sun, it is expected that diffusion dominates the differential rotation of the magnetic photospheric footpoints throughout a much longer period of the astro cycle. The expected field configuration from these stars is then rather a turbulent Parker-like field than a Fisk-type field, and may be described by the model of Giacalone [see, e.g., *Giacalone and Jokipii*, 1999; *Giacalone*, 2001; *Giacalone and Jokipii*, 2004].

5.9 Summary

In this chapter a refined Fisk-Parker hybrid magnetic field model was introduced, valid at all latitudes and during all solar activity conditions.

It was shown that a transition function that is implemented in the velocity field of the hybrid HMF simulates the latitude dependence of the Fisk effect. It was found that the total Fisk effect first increases with solar activity, attains a maximum during moderate solar activity periods and then decreases until no effect is expected at solar maximum. During the declining activity phase the Fisk effect increases to the same maximum and then decreases gradually again toward solar minimum.

The Fisk effect can in principle be tested for by investigating both the global and local effect of the hybrid HMF on cosmic rays in the heliosphere. A model which describes the modulation of cosmic rays in the heliosphere is developed in the next chapter and this model is then used to investigate the influence of the hybrid field on cosmic rays.

Chapter 6

Modulation of Cosmic Rays in the Heliosphere

6.1 Introduction

In Sections 4.1 and 4.10, it is argued that should the Fisk field exist, its signature should be seen directly in magnetic field data or indirectly in the behaviour of cosmic rays (CRs) reacting to it. As discussed in Section 4.10, the interpretation of magnetic field data is ambiguous. Due to the influence of coronal magnetic field diffusion, a clear indication of a Fisk-type field is extremely difficult to observe on relatively short time and distance scales (see Section 5.2). Considering CR behaviour, the existence of a Fisk-type field is much more evident from their local behaviour [*Zhang*, 1997] as illustrated by *Burger and Hitge* [2004]. However, *Zhang* [1997] does not even refer to a Fisk-type field, and *Paizis et al.* [1999] see it only as a *possible* cause of the high-latitude recurrent particle variations. Furthermore, the numerical modelling of *Burger and Hitge* [2004] supports the existence of a Fisk-type field, but they do not claim it as a fact.

This chapter is devoted to investigating the influence of the Fisk-Parker hybrid field on CRs in order to test for the existence of a Fisk-type field. Solar particles that are modulated by corotating interaction regions (CIRs) are not considered, but only galactic CRs that penetrate the inner heliosphere. Since the source surface footpoint velocities of the hybrid field show clear 26-day variations (see Fig. 5.3), the hybrid field structure implicitly contains these variations and accordingly CRs, which are modulated by this field, should show a similar local behaviour.

Firstly, the particles that are known as cosmic rays are briefly described. Then the modulation model, which describes the behaviour of CRs in the heliosphere due to the influence of the solar wind and magnetic field, is introduced. Since the magnetic field is contained in the diffusion tensor, some attention is given to the latter. The importance of drift effects in the heliosphere is described in more detail, specifically in the equatorial region where the HMF is Parker-like. Finally, the hybrid field is implemented in this modulation model to investigate the global and local behaviour of CRs in the inner heliosphere.

6.2 Cosmic Rays

The energetic, mostly fully ionised particles that traverse the heliosphere are known as cosmic rays (CRs). The energy of CRs exceeds ~100 keV, i.e. several orders of magnitude higher than the average particle energy in the heliosphere. CR energies of up to $\sim 3 \times 10^{21}$ eV have been observed. CRs consist of ~ 87% protons, ~ 12% helium nuclei, ~ 1% electrons and traces of heavier nuclei [see, e.g., *Simpson*, 1992].

The energy of a particular CR mainly depends on its origin. CRs with energies above ~ 10 GeV originate primarily from outside the heliosphere. The highest energy CRs are probably extragalactic. Powerful sources, such as radio galaxies and quasars, may generate such high energies. Galactic CRs are generated in our local galaxy mainly in supernova explosions, supernova remnants, binary stars and in the magnetospheres of pulsars. CRs originating inside the heliosphere have energies below ~ 10 GeV and comprise solar, anomalous, interplanetary and planetary CRs. Solar CRs are produced by solar flares and CMEs. Anomalous CRs are formed by atoms that have been ionised in the solar wind and subsequently accelerated at the termination shock. Interplanetary shock waves, such as those from CIRs, may produce interplanetary CRs. The magnetospheres of Jupiter and Saturn are sources of low-energy planetary CRs. The model in this study neglects heliospheric sources and only considers galactic protons. For recent overviews, see, e.g., *Ferreira* [2002] and *Langner* [2004].
It is known that the intensities of relatively low energy CRs have very small anisotropies at the earth [*Cowsik*, 1975]. We may therefore assume an omni-directional distribution of CRs in the heliosphere at regions far enough from CR sources.

6.3 The Transport Equation

Cosmic rays in the heliosphere with energies below ~10 GeV are strongly influenced by the HMF and the solar wind. The resulting physical processes change the intensity and energy of the CRs with position and time, so that only a fraction of galactic CRs reaches the inner heliosphere. This phenomenon is known as the modulation of CRs. Energies above 100 GeV correspond to gyroradii of about the size of the heliosphere and consequently such CRs are hardly affected by heliospheric modulation.

More specifically, modulation of CRs results from convection and adiabatic cooling in the solar wind, as well as diffusion and drift of the CRs in the HMF. The strong outward convection of the CRs is caused by the supersonic radial flow of the solar wind, whereas adiabatic cooling, or deceleration, describes the energy changes due to the expansion of the solar wind. On a macroscopic scale, the HMF has a smooth structure and the large-scale gradients in the field magnitude and curvature of the field lines cause significant drifts of the CRs. Large drifts are caused by abrupt changes, or current sheets, in the HMF, especially at the HCS. On a microscopic scale, the irregularities of the HMF govern the diffusion of the CRs.

The differential intensity with respect to the kinetic energy in the interval $(T, T+dT)$ is denoted by j_T. The strong energy dependence of these intensities is illustrated by an energy spectrum, also called an intensity spectrum. The observed spectrum of galactic CRs at the heliospheric boundary is referred to as the local interstellar spectrum (LIS) or galactic spectrum. As function of the particle rigidity

$$P = \frac{pc}{|q|}, \tag{6.1}$$

with q and p the charge and momentum of a particle, respectively, and c the speed of light in vacuum, the LIS for protons in this study is the one employed by *Bieber et al.* [1999], given by

$$f_{LIS}(P) = \begin{cases} 1.9 \times 10^4 \ln P^{-2.78} & \text{if } P \geq 7\,\text{GV}; \\ \exp(9.472 - 1.999 \ln P - 0.6938 \ln P^2 & \\ \quad +0.2988 \ln P^3 - 0.04714 \ln P^4) & \text{if } P < 7\,\text{GV}. \end{cases} \tag{6.2}$$

The modulation processes are combined in a transport equation (TPE), first derived by Parker (1965). It is more convenient to solve the TPE for the omni-directional distribution of the CRs than for the differential intensities. Such solutions of the TPE then predict the distribution of the CRs as function of their position $\mathbf{r}$ and momentum $\mathbf{p}$ at time t, i.e. $f(\mathbf{r}, \mathbf{p}, t)$. The relation between f and j_T is given by $j_T = p^2 f$, where $p = |\mathbf{p}|$.

In terms of the distribution function, the general form of the TPE is written as

$$\frac{\partial f}{\partial t} - \nabla \cdot (\mathsf{K} \cdot \nabla f) + \mathbf{V} \cdot \nabla f - \frac{1}{3}(\nabla \cdot \mathbf{V}) \frac{\partial f}{\partial \ln p} = Q(\mathbf{r}, \mathbf{p}, t). \tag{6.3}$$

The parameter $\mathbf{V}$ is the solar wind velocity and Q describes possible sources or sinks of CRs inside the heliosphere. The second term on the left describes the diffusion and drift of the particles caused by the HMF, whereas the third and last terms describe the outward particle convection and adiabatic energy changes of the CRs, respectively, due to the expanding solar wind. The diffusion tensor, denoted by K, is the focus of the next section.

6.4 The Diffusion Tensor

The general expression for the diffusion tensor in heliospheric polar coordinates $(\mathbf{r}, \theta, \phi)$ is given by

$$\mathsf{K} = \begin{bmatrix} \kappa_{rr} & \kappa_{r\theta} & \kappa_{r\phi} \\ \kappa_{\theta r} & \kappa_{\theta\theta} & \kappa_{\theta\phi} \\ \kappa_{\phi r} & \kappa_{\phi\theta} & \kappa_{\phi\phi} \end{bmatrix}. \tag{6.4}$$

In a coordinate system with one axis parallel to the average magnetic field, $\mathbf{B}$, and the other two axes perpendicular to it,

$$\mathsf{K} = \begin{bmatrix} \kappa_{\|} & 0 & 0 \\ 0 & \kappa_{\perp,\theta} & \kappa_A \\ 0 & -\kappa_A & \kappa_{\perp,r/\phi} \end{bmatrix}, \tag{6.5}$$

where $\kappa_{\|}$ describes the diffusion parallel to $\mathbf{B}$, $\kappa_{\perp,\theta}$ and $\kappa_{\perp,r/\phi}$ describe diffusion perpendicular to $\mathbf{B}$ in the polar and radial/azimuthal directions, respectively, and κ_A, often also denoted by κ_T, is the drift coefficient.

When the perpendicular diffusion is isotropic, $\kappa_{\perp,\theta} = \kappa_{\perp,r/\phi} = \kappa_{\perp}$ and in spherical coordinates K is given by [*Kobylinski*, 2001]

$$\begin{aligned}
\kappa_{rr} &= (\kappa_{\|}\cos^2\psi + \kappa_{\perp}\sin^2\psi)\cos^2\zeta + \kappa_{\perp}\sin^2\zeta \\
\kappa_{r\theta} &= (\kappa_{\|}\cos^2\psi + \kappa_{\perp}\sin^2\psi - \kappa_{\perp})\sin\zeta\cos\zeta - \kappa_A\sin\psi \\
\kappa_{r\phi} &= (-\kappa_{\|} + \kappa_{\perp})\sin\psi\cos\psi\cos\zeta - \kappa_A\cos\psi\sin\zeta \\
\kappa_{\theta r} &= (\kappa_{\|}\cos^2\psi + \kappa_{\perp}\sin^2\psi - \kappa_{\perp})\sin\zeta\cos\zeta + \kappa_A\sin\psi \\
\kappa_{\theta\theta} &= (\kappa_{\|}\cos^2\psi + \kappa_{\perp}\sin^2\psi)\sin^2\zeta + \kappa_{\perp}\cos^2\zeta \\
\kappa_{\theta\phi} &= (-\kappa_{\|} + \kappa_{\perp})\sin\psi\cos\psi\sin\zeta + \kappa_A\cos\psi\cos\zeta \\
\kappa_{\phi r} &= (-\kappa_{\|} + \kappa_{\perp})\sin\psi\cos\psi\cos\zeta + \kappa_A\cos\psi\sin\zeta \\
\kappa_{\phi\theta} &= (-\kappa_{\|} + \kappa_{\perp})\sin\psi\cos\psi\sin\zeta - \kappa_A\cos\psi\cos\zeta \\
\kappa_{\phi\phi} &= \kappa_{\|}\sin^2\psi + \kappa_{\perp}\cos^2\psi .
\end{aligned} \tag{6.6}$$

Here, the spiral angle, $\psi = \arctan(-B_\phi/B_r)$, is the angle between the field line projection onto the (r,ϕ) plane and the radial direction, i.e., the field direction relative to the radial direction in this plane. In the coordinate system of Equation (6.5), this is the angle between the mean magnetic field and the radial direction (cf. Section 3.3). The deviation angle, $\zeta = \arctan(B_\theta/B_r)$, is the angle between the field line projection onto the meridional plane (r,θ) and the radial direction, in other words, the field direction relative to the radial direction in the meridional plane. When $B_\theta = 0$, $\zeta = 0$ and the diffusion tensor reduces to the usual form used in the Parker model.

Dividing the diffusion tensor into its symmetric and anti-symmetric parts, i.e. $\mathsf{K} = \mathsf{K}^{\mathrm{s}} + \mathsf{K}^{\mathrm{a}}$, the second term in Equation (6.3) can be written as

$$\nabla \cdot (\mathsf{K} \cdot \nabla f) = \nabla \cdot (\mathsf{K}^{\mathrm{s}} \cdot \nabla f) + \nabla \cdot (\mathsf{K}^{\mathrm{a}} \cdot \nabla f) \tag{6.7}$$

Note from Equation (6.5) that the anti-symmetric part of the diffusion tensor, K^{a}, describes the drift of the CRs, whereas the symmetric part, K^{s}, comprises all the diffusion coefficients. The last term of Equation (6.7) can then be written in terms of the (guiding centre) drift velocity vector $\mathbf{v}_d$ [*Hattingh*, 1998],

$$\nabla \cdot (\mathsf{K}^{\mathrm{a}} \cdot \nabla f) = -\nabla \cdot (\mathbf{v}_d f), \tag{6.8}$$

where

$$\mathbf{v}_d = \nabla \times (\kappa_A \mathbf{e}_B), \tag{6.9}$$

with $\mathbf{e}_B$ a unit vector in the direction of the magnetic field.

Since the rotation of any vector has zero divergence, $\nabla \cdot \mathbf{v}_d = 0$. Therefore,

$$\nabla \cdot (\mathsf{K}^{\mathrm{a}} . \nabla f) = -\mathbf{v}_d \cdot \nabla f. \tag{6.10}$$

In this study the steady-state, three-dimensional modulation model of *Burger and Hattingh* [1995], *Hattingh and Burger* [1995] and *Hattingh* [1998], based on the TPE in Equation (6.3), is used. The modulation model is in a frame which co-rotates with the solar equator and therefore a steady-state, or time-independent, TPE can be used [*Kóta and Jokipii*, 1983]. This is a reasonable approximation near solar minimum conditions. In the co-rotating frame the solar wind speed, $\mathbf{V}_{sw}$, is exchanged for $\mathbf{V}^* = \mathbf{V}_{sw} - \mathbf{\Omega} \times \mathbf{r}$, where $\mathbf{\Omega}$ is the solar equatorial rotation rate. Furthermore, the coordinate system of Equation (6.10) is used. Since only galactic CRs are considered, the source term vanishes. The model which describes the behaviour of the CRs in the heliosphere is then given by the TPE

$$\nabla \cdot (\mathsf{K}^{\mathrm{S}} \cdot \nabla f) - (\mathbf{v}_d + \mathbf{V}^*) \cdot \nabla f + \frac{1}{3} (\nabla \cdot \mathbf{V}^*) \frac{\partial f}{\partial \ln p} = 0. \tag{6.11}$$

The diffusion and drift coefficients are similar to those used by *Burger and Hitge* [2004]. The parallel diffusion coefficient is adapted from *Burger et al.* [2000] for a constant model heliospheric boundary at 100 AU. The isotropic perpendicular diffusion coefficient is given by

$$\kappa_\perp = 0.1 \kappa_\parallel \left(\frac{P}{P_0} \right)^\eta , \tag{6.12}$$

where $P_0 = 1$ GV ensures the correct units. The rigidity dependence of the perpendicular diffusion coefficient, with respect to that of the parallel diffusion, is changed via the parameter η. If $\eta > 0$, the perpendicular diffusion coefficient in the polar direction has a flatter rigidity dependence than the parallel diffusion coefficient. In the modulation model, some cross-field diffusion is included by setting $\eta = -1/3$ in Equation (6.12). Furhermore, the drift coeffient

$$\kappa_A = \frac{pv}{3qB} \frac{(P/P_1)^2}{1 + (P/P_1)^2} \tag{6.13}$$

is used, with $P_0 = 1/\sqrt{2}$ GV. A constant solar wind speed of 600 km/s at all latitudes is assumed and the expression for β given by Equation (5.19) is used.

6.5 Drift Effects in the Heliosphere

Since the large-scale motion of CRs is determined by drift effects in the heliosphere, this section deals with these processes. Here the emphasis is on the equatorial region where the HCS is present and where the Fisk-Parker hybrid model is Parker-like.

The net drift velocity is defined in Equation (6.9), with

$$\mathbf{e}_B = \left[1 - 2H(\theta - \theta') \right] \mathbf{e}'_B . \tag{6.14}$$

The coefficient $1-2H(\theta-\theta')$ uses the Heaviside step function [Equation (3.19)] to describe the alternating polarities of the magnetic field across the HCS. A unit vector in the field direction is given by

$$\mathbf{e}'_B = \frac{\mathbf{e}_r - \Gamma \mathbf{e}_\phi}{\sqrt{1+\Gamma^2}}, \tag{6.15}$$

where the abbreviation

$$\Gamma \equiv \frac{\Omega\,(\mathrm{r}-\mathrm{r_S})}{V_{sw}} \sin\theta = \tan\psi \tag{6.16}$$

is used.

Substitution of Equation (6.14) into Equation (6.9) yields

$$\begin{aligned}
\mathbf{v}_d &= \nabla \times (\kappa_A \mathbf{e}_B) \\
&= \left[\nabla \times (\kappa_A \mathbf{e}'_B)\right]\left[1 - 2H(\theta-\theta')\right] + 2\delta(\theta-\theta')\kappa_A \mathbf{e}'_B \times \nabla(\theta-\theta') \\
&\equiv \mathbf{v}_{d,m}\left[1-2H(\theta-\theta')\right] + \mathbf{v}_{ns}\delta(\theta-\theta'),
\end{aligned} \tag{6.17}$$

where the derivative of $H(\theta-\theta')$ is the Dirac-delta function

$$\delta(\theta-\theta') = \begin{cases} \infty, & \theta=\theta'; \\ 0, & \theta\neq\theta'. \end{cases} \tag{6.18}$$

In Equation (6.17), the drift velocity is decomposed into $\mathbf{v}_{d,m}$ and $\mathbf{v}_{ns}$, denoting the drift due to gradients and curvature in the large-scale magnetic field and the drift along the HCS, respectively. In order to implement Equation (6.17) in numerical codes, the Heaviside and Dirac-delta functions need to be described. The first is approximated by a hyperbolic tangent function. The effect of the Dirac-delta function can be described by taking the derivative of $\tanh(\theta-\theta')$, viz. $\mathrm{sech}^2(\theta-\theta')$, to model a moderate transition across the HCS. Such a transition function actually simulates the finite width of the HCS.

A particle in an external magnetic field **B** gyrates in a plane perpendicular to the field direction. The radius of gyration, known as the gyroradius or Larmor radius, is defined as

$$r_L \equiv v/\omega_c = mv/(|q|B), \tag{6.19}$$

where $\omega_c = |q|B/m$ is the cyclotron frequency, v is the speed of the particle in a plane perpendicular to the field vector $\mathbf{B}$, m and q are the mass and charge of the particle, respectively, and B is the average field strength.

A particle is only affected by the HCS when it is located within two gyroradii from it. In order to separate the effect of the HCS drift from other drift effects at a certain latitude, it is necessary to define the region swept out by particles drifting along the HCS in one solar rotation. This region is known as the HCS region and is defined by the latitude θ such that

$$\frac{\pi}{2} - \alpha - \theta_{ns} < \theta < \frac{\theta}{2} + \alpha + \theta_{ns}, \tag{6.20}$$

where θ_{ns} is the angle spanned by two gyroradii of a particle at a radial distance r from the sun, i.e. $\theta_{ns} = \sin^{-1}(r_L/r)$, or $\theta_{ns} = 2r_L/r$ when $r_L \ll r$. The HCS region is illustrated in Figure 6.1

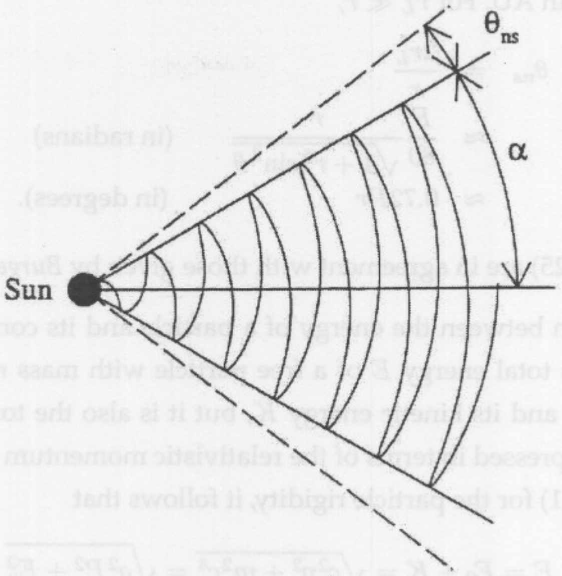

Figure 6.1: A schematic of the HCS region [adapted from *Hattingh*, 1993].

for a tilt angle of 30° [adapted from *Hattingh*, 1993]. The angle θ_{ns} depends significantly on the energy of a particular CR. In order to determine the influence region of the neutral sheet on CRs with a certain energy, the relation between r_L, θ_{ns}, the rigidity P and the energy E is derived next.

In terms of the rigidity, the gyroradius can be expressed as

$$r_L = \frac{P}{Bc}. \tag{6.21}$$

Since $\Omega/V \sim \mathrm{AU}^{-1}$ for the sun, the average field strength of the Parker field in units of AU is

$$\begin{aligned} B &= \sqrt{B_r^2 + B_\phi^2} \\ &= A\left(\frac{r_e}{r}\right)^2 \sqrt{1 + \left(\frac{\Omega r}{V}\sin\theta\right)^2} \\ &\approx \frac{A}{r^2}\sqrt{1 + r^2\sin^2\theta} \qquad (r \text{ in AU}). \end{aligned} \tag{6.22}$$

By normalising the field at the earth, where $r = 1$ AU, $\theta = 90°$ and $B \approx 5$ nT, the constant $A \approx 5/\sqrt{2}$ nT·AU is obtained. Furthermore, the large CR rigidities are usually expressed in terms of GV. Then, to be consistent, both B and c should be expressed in terms of GV and AU:

$$\begin{aligned} 1\ \mathrm{T} &= 1\ \mathrm{V{\cdot}s{\cdot}m^{-2}} = 10^{-9}\ \ \mathrm{GV{\cdot}s{\cdot}m^{-2}} = 2.25\times10^{13}\ \ \mathrm{G{\cdot}V{\cdot}s{\cdot}AU^{-2}} \\ \Longrightarrow 1\ \mathrm{nT} &= 2.25\times10^{4}\ \ \mathrm{GV{\cdot}s{\cdot}AU^{-2}} \\ \Longrightarrow \quad B &= 7.95\times10^{4}\ \ r^2\sqrt{1+r^2\sin^2\theta}\ \ \mathrm{GV{\cdot}s{\cdot}AU^{-2}}. \end{aligned} \tag{6.23}$$

Noticing that $c = 3.00\times10^{8}$ m/s $= 1.98\times10^{-3}$ AU/s, it follows from Equation (6.21) that

$$2r_L \approx \frac{P}{80}\frac{r^2}{\sqrt{1+r^2\sin^2\theta}}, \tag{6.24}$$

where P is in GV and r in AU. For $r_L \ll r$,

$$\begin{aligned}\theta_{ns} &= \frac{2r_L}{r} \\ &\approx \frac{P}{80}\frac{r}{\sqrt{1+r^2\sin^2\theta}} && \text{(in radians)} \\ &\approx 0.72Pr && \text{(in degrees).} \qquad (6.25)\end{aligned}$$

Equations (6.24) and (6.25) are in agreement with those given by *Burger* [1987].

As an aside, the relation between the energy of a particle and its corresponding rigidity can easily be deduced. The total energy E of a free particle with mass m is the sum of its rest-mass energy $E_0 = mc^2$ and its kinetic energy K, but it is also the total relativistic energy of the particle, which is expressed in terms of the relativistic momentum p as $E = \sqrt{c^2p^2 + m^2c^4}$. Employing Equation (6.1) for the particle rigidity, it follows that

$$\begin{aligned} E = E_0 + K = \sqrt{c^2p^2 + m^2c^4} &= \sqrt{q^2P^2 + E_0^2} \\ \Longrightarrow K &= \sqrt{(qP)^2 + E_0^2} - E_0. \qquad (6.26)\end{aligned}$$

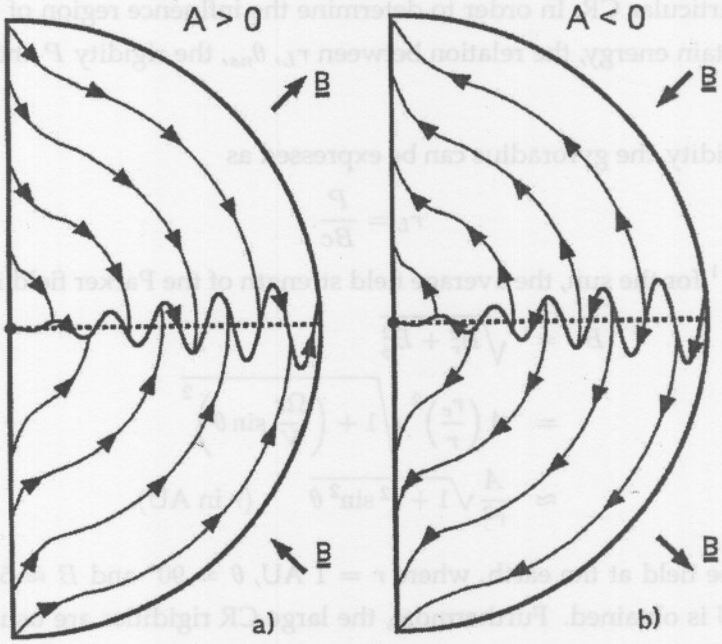

Figure 6.2: The projection of the drift directions onto the meridional plane for positively-charged CRs in a Parker HMF during an a) $A > 0$ and an b) $A < 0$ epoch. The effect of the HCS, as well as the gradient and curvature drifts, is evident [*Jokipii and Thomas*, 1981].

The meridional projection of the drift trajectories in a Parker HMF for positively-charged CRs, such as the protons that are used in this study, is shown in Figure 6.2 [*Jokipii and Thomas*, 1981]. On the polar axis, the polar angle $\theta = 0°$, so that the magnetic field has only a radial component. The CRs drift relatively easily along the polar axis in this HMF. The radial and azimuthal components of the magnetic field decrease with r^2 and r, respectively. At large radial distances from the sun, the particle drift is primarily in the θ-direction. During the $A > 0$ epoch, the particles drift inward along the solar poles and in the meridional direction toward the HCS, where drift along the HCS then dominates and direct the particles outward. For $A < 0$, the drift directions switch.

6.6 The Global Behaviour of Cosmic Rays in a Fisk-Type Field

In the next two sections, the influence of a Fisk-type field on galactic CRs in the inner heliosphere is investigated from numerical modulation results in order to test for the existence of such a magnetic field. These results were obtained by implementing the Fisk-Parker hybrid field model, which is fully developed in Chapter 5, in the TPE (6.3) through the drift velocity and the diffusion coefficients. Firstly, the effect of the Fisk-Parker hybrid field on the global behaviour of protons in the heliosphere is investigated and compared with the corresponding results obtained by *Burger and Hitge* [2004]. Thereafter, the local proton recurrent variations are studied more extensively and compared with the observational results of *Zhang* [1997] and *Paizis et al.* [1999].

The latitudinal gradient of particles between the polar angles θ_1 and θ_2 at a radial distance r is defined as

$$G_\theta(r) = \frac{1}{\theta_1 - \theta_2} \ln \left[\frac{j_T(r, \theta_2)}{j_T(r, \theta_1)} \right] \times 100\%. \tag{6.27}$$

Similar to *Burger and Hitge* [2004], the values $\theta_1 = 90°$ and $\theta_2 = 20°$ are assumed in order to study the global effects. Since *Ulysses* traverses a maximum latitude of about 80°, *Zhang* [1997] employs the values $\theta_1 = 80°$ and $\theta_2 = 10°$. The same values are therefore assumed to compare the numerical results with the measurements of 26-day variations.

Figure 6.3 compares the effect of the Fisk-Parker hybrid field on the proton intensities in both the polar region at 1 AU and at the earth with that of a pure Parker field. The upper two panels show the energy spectra representing each of the two latitude regions and the bottom panel shows the intensity difference between the two latitudes in both field models.

The topmost line denotes the local interstellar spectrum which is used as the initial intensity. A constant differential rotation of $\omega = \Omega/4$ is assumed for both the Parker and hybrid fields at all latitudes. The hybrid field (dashed lines) reduces the proton intensities slightly more than the Parker field during the $A > 0$ epoch. This result is qualitatively similar to what *Burger and Hitge* [2004] found and is consistent with what is expected for a Fisk-type field. During the $A > 0$ polarity cycle, the protons drift mainly from the polar regions toward the equatorial region (see Fig. 6.2) and are influenced more by a Fisk-type field than by the simpler structure of the standard Parker spiral (see, e.g., Fig. 4.3). For the alternate polarity cycle, the intensities of the protons in the two fields do not differ significantly. This result is also expected, because

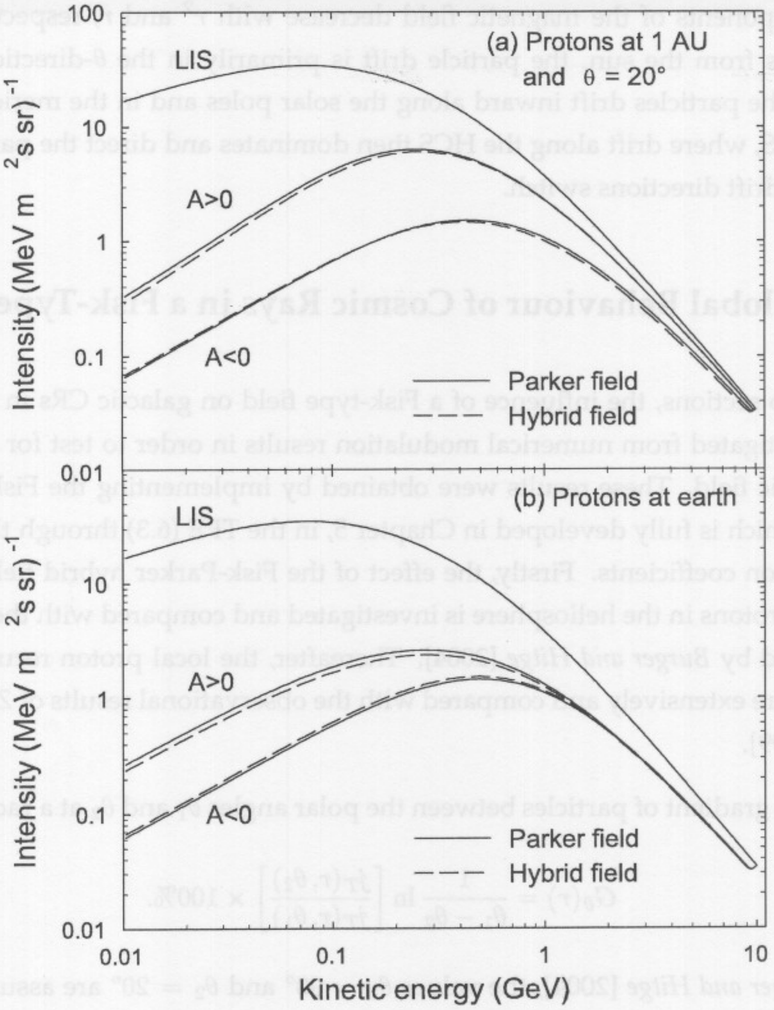

Figure 6.3: Proton energy spectra (a) at a polar angle 20° at 1 AU and (b) at the earth for a Parker field (solid lines) and the hybrid field (dashed lines). The results represent low solar activity conditions for the tilt angle $\alpha = 10°$. The boundary intensity is the local interstellar spectrum, denoted by LIS. The upper two lines show the results for an $A > 0$ polarity epoch, while the lower two lines for $A < 0$ almost coincide.

the protons drift primarily along the HCS toward the inner heliosphere during this cycle and in the equatorial region the HMF is assumed to be a Parker field in both field models.

Figure 6.4 indicates that during the positive polarity epoch, fewer protons reach the equatorial region from higher latitudes in the hybrid field than in the Parker field, consistent with what is expected from the effect of a Fisk-type field on particles that propagate inward from the outer heliosphere. This result is contrary to what is expected for CIR particles, which propagate along the field lines of a Fisk-type field toward higher latitudes and therefore will have a larger intensity at higher latitudes than in the equatorial region. During the alternate polarity epoch the change is small, consistent with Panels (a) and (b) of Figure 6.3.

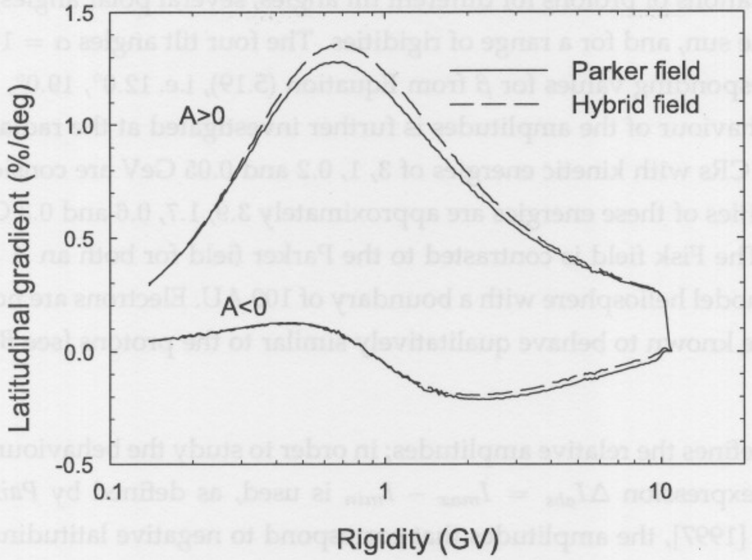

Figure 6.4: The proton intensity gradients at 1 AU between the two co-latitudes in Figure 6.3 as function of the particle rigidity for a Parker field (solid lines) and the hybrid field (dashed lines). Here again, $\alpha = 10°$.

6.7 The Local Behaviour of Cosmic Rays in a Fisk-Type Field

Zhang [1997] investigated the recurrent variations as observed by *Ulysses* within the period from the Jupiter encounter in February 1992 to the northern polar pass in August 1995 (see Fig. 2.17). The daily averaged intensity measurements were first detrended by subtracting the average over one solar rotation from the corresponding data and then the result was normalised by using the same averages. The amplitude is then defined as the normalised difference between the average maximum and minimum values within one solar rotation and expressed as a percentage, given by

$$\Delta I = \frac{I_{max} - I_{min}}{\langle I \rangle} \times 100\,\%, \tag{6.28}$$

where I_{max} and I_{min} are the maximum and minimum values of the original daily averaged intensities within a period of 26 days, and $\langle I \rangle$ is the average intensity in this period. This definition differs slightly from the relative amplitude defined by *Burger and Hitge* [2004], but nevertheless gives qualitatively similar results.

Zhang [1997] mainly analysed the proton behaviour within the energy range ~ 0.1 GeV to $\gtrsim 1$ GeV. The results of some heavier nuclei are also considered. Most of the flux variations of low-energy particles show an anti-correlation with the variations of higher energy particles. These variations are defined to have negative amplitudes. *Zhang* [1997] remarks that it is not certain whether these low-energy particles exhibit recurrent variations at all. However, only relatively few of these particles were observed and their contribution to the average results is often insignificant [*Zhang*, 1997].

The hybrid and Parker HMF models are used to investigate the behaviour of the amplitudes of the recurrent variations of protons for different tilt angles, several polar angles, at a few radial distances from the sun, and for a range of rigidities. The four tilt angles $\alpha = 10°, 20°, 30°$ and $40°$ and the corresponding values for β from Equation (5.19), i.e. 12.0°, 19.0°, 22.3° and 22.7° are used. The behaviour of the amplitudes is further investigated at the radial distances 1, 2, 5, 25 and 50 AU. CRs with kinetic energies of 3, 1, 0.2 and 0.05 GeV are considered. The corresponding rigidities of these energies are approximately 3.9, 1.7, 0.6 and 0.3 GV, respectively [see Eq. (6.26)]. The Fisk field is contrasted to the Parker field for both an $A > 0$ and $A < 0$ epoch, and in a model heliosphere with a boundary of 100 AU. Electrons are not considered in this study, but are known to behave qualitatively similar to the protons [see *Burger and Hitge*, 2004].

Equation (6.28) defines the relative amplitudes; in order to study the behaviour of the absolute amplitudes, the expression $\Delta I_{abs} = I_{max} - I_{min}$ is used, as defined by *Paizis et al.* [1999]. Following *Zhang* [1997], the amplitudes that correspond to negative latitudinal gradients are defined to be negative in order to correlate with the other data. These amplitudes are typically obtained for the $A < 0$ polarity epochs.

6.7.1 Properties of the Modelled Relative Amplitude

Figure 6.5 illustrates the relationship between ΔI and G_θ for protons at 2 AU at (a) small and (b) large polar angles. A clear linear relationship in and near the polar region is shown in the top panel. Moreover, the behaviour at a polar angle of 30° agrees well with that obtained by *Burger and Hitge* [2004], who used a much smaller model heliosphere with a radius of 50 AU. The top panel shows that the slope of the linear regression increases significantly with polar angle at small and mid-latitudes. The bottom panel indicates that the linear relationship becomes less significant toward the solar equatorial region where the HCS drift dominates. Although not shown, it is found that no simple relationship exists between G_θ and the absolute amplitude ΔI_{abs}. This is probably the reason why *Paizis et al.* [1999], who investigated such amplitudes, did not illustrate or mention any relationship.

The influence of the tilt angle on the relative amplitudes at 1 AU is illustrated by the contour diagram in Figure 6.6 for 1 GeV protons in both (a) the hybrid and (b) the Parker field. The effect of the HCS region is evident for both field models, increasing the relative amplitude significantly with both polar angle and tilt angle. In the Parker field (bottom panel) the amplitudes decrease to zero outside the HCS region, as expected. At this radial distance these 1 GeV protons have a rigidity of 1.7 GV [see Eq. 6.26] and therefore θ_{ns} is only approximately 1.2° [see Eq. 6.25]. The feature that the HCS influences the relative amplitude of the particles beyond the HCS region is also evident from the results of *Kóta and Jokipii* [1983]. In the hybrid field, the rate of decrease to smaller amplitudes toward the pole is slower than in the Parker field. As expected, the amplitudes vanish at the solar pole.

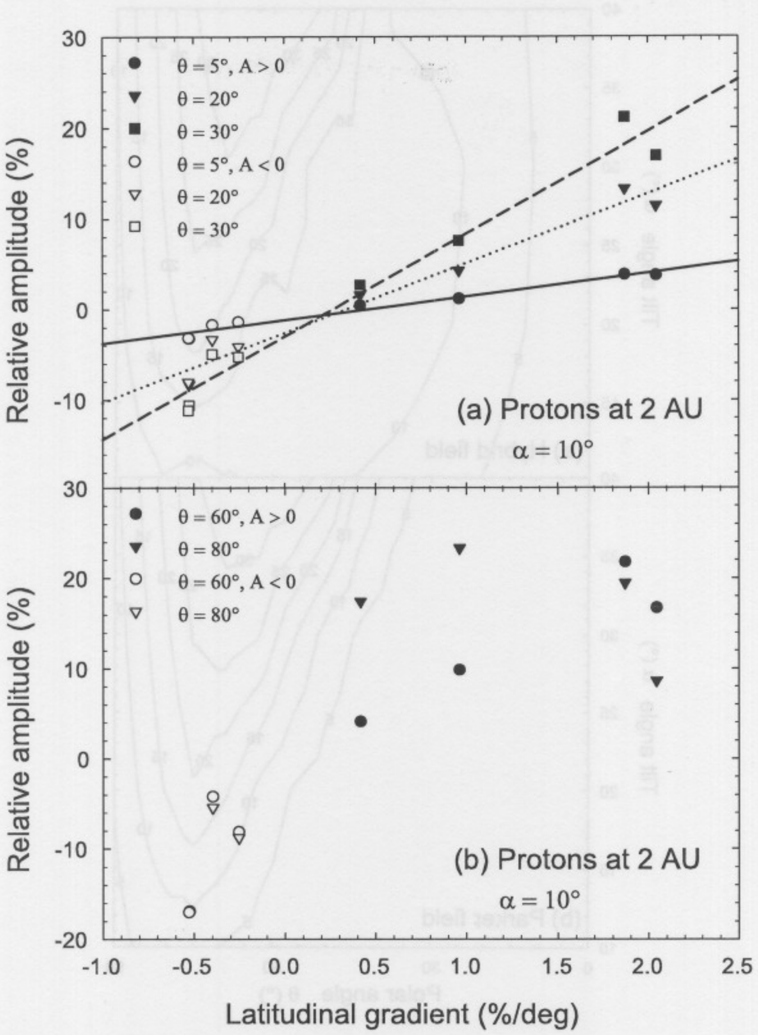

Figure 6.5: The relationship between the latitudinal gradient and the relative amplitudes of the recurrent variation of protons at (a) small and (b) large polar angles, or equivalently, in (a) the polar region and (b) the equatorial region. The results for the $A > 0$ polarity epoch are denoted by filled symbols; open symbols are used for the $A < 0$ epoch. A radial distance of 2 AU from the sun and the solar activity state at $\alpha = 10°$ were used.

According to the PCH model that is shown in Figure 5.6, β attains a maximum value at $\alpha = 40°$. It is remarked in Chapter 5 that the Fisk effect depends primarily on β. Following the 10 % contour line in Figure 6.6(a), it may be suggested that the maximum Fisk effect occurs for $\alpha \approx 30°$. Although not shown, similar results are obtained at larger radial distances and for different energies, as well as for the absolute amplitudes.

Figure 6.7 shows the radial dependence of the relative amplitude of 0.2 GeV protons at three representative polar angles during the (a) $A > 0$ and (b) $A < 0$ polarity cycles. Evidently, the effect of the Fisk field vanishes completely beyond ~ 50 AU during both polarity epochs. Although not shown, the absolute amplitudes show a similar behaviour with the radial distance. In the inner heliosphere, the relative amplitude increases significantly with polar angle and

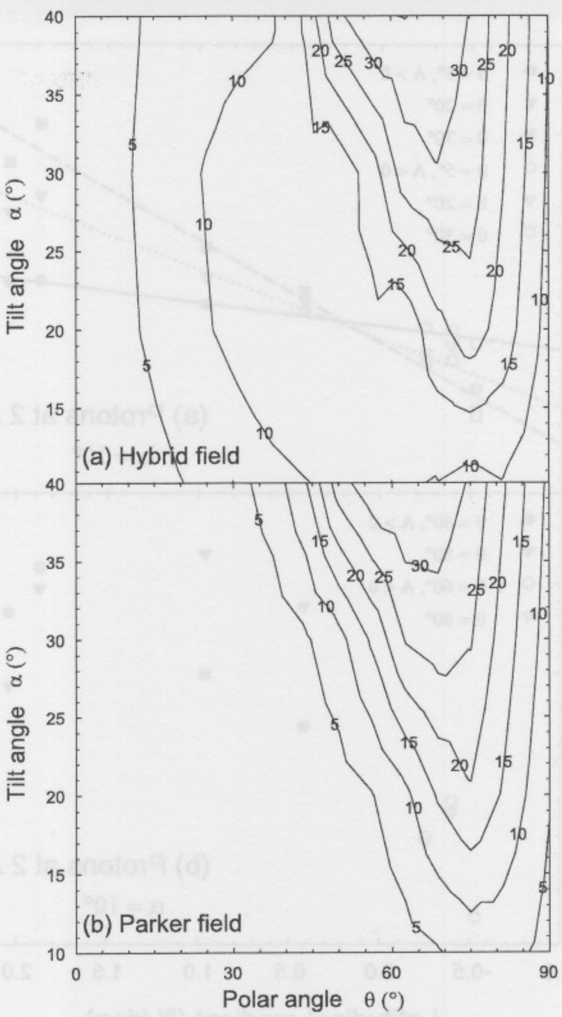

Figure 6.6: A comparison between the relative amplitudes, expressed as percentages, as function of the tilt angle and polar angle for (a) the hybrid field and (b) the standard Parker field. The results are shown for 1 GeV protons at 1 AU during a positive solar cycle.

attains a maximum at $\theta \sim 50°$. The amplitude first increases with radial distance and then decreases. In both polarity epochs the decrease occurs rapidly at large polar angles and more gradually toward the solar poles. During $A < 0$, the amplitude increases significantly up to ~ 25 AU and then fades out. According to this figure, the largest Fisk effect is expected at mid-latitudes and between the radial distances $\sim 2 - 5$ AU.

6.7.2 Relative Amplitude and Latitudinal Gradients

Zhang [1997] illustrates the linear relationship between ΔI and G_θ for each of six representative regions in the inner heliosphere which *Ulysses* traversed (see Fig. 6.8). He states that this result indicates that CR intensity variations are independent of the local conditions of the solar wind in the inner heliosphere. Evidently, the slope of the regression line first increases slightly from Panel (A) to Panel (B), decreases by nearly 50% to Panel (C) and then decreases more gradually

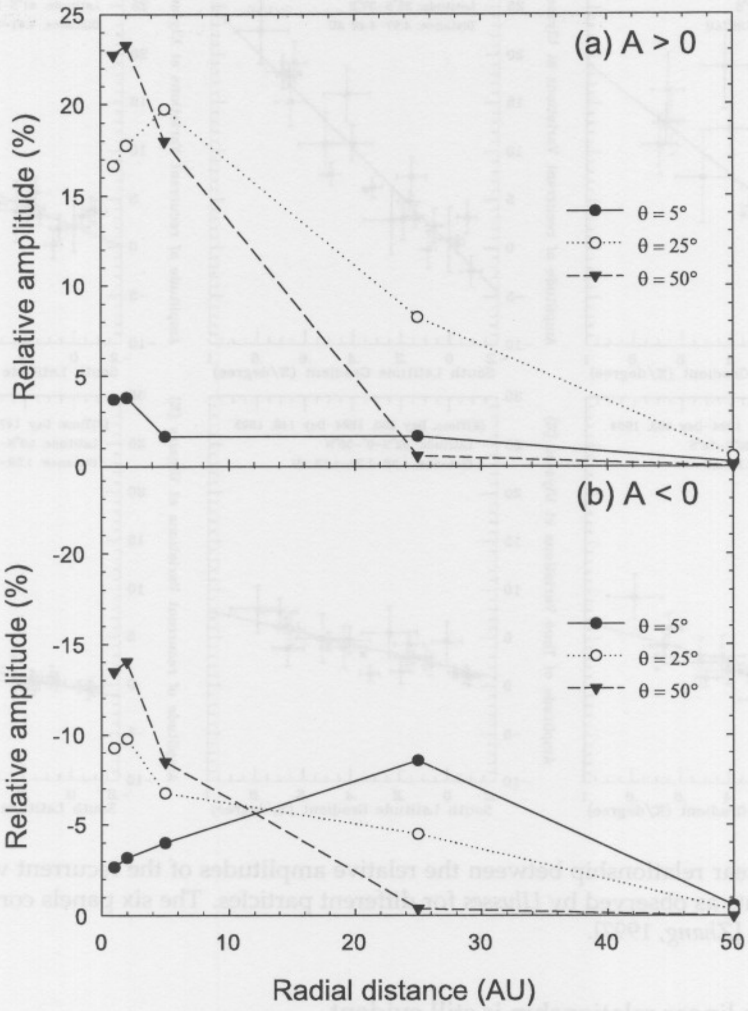

Figure 6.7: The relative amplitudes of the recurrent 0.2 GeV proton intensity variations as function of radial distance at three different polar angles, as produced by the hybrid field. The top panel shows the behaviour for the $A > 0$ polarity cycle and the bottom panel for $A < 0$. All results are for $\alpha = 10°$.

to the last panel. Considering the different latitudinal bands, this means that at a given G_θ, ΔI increases with latitude, and then decreases toward the polar region. Note that not all regression lines cross the origin exactly, that only a few data points corresponding to negative latitudinal gradients are present and that some of these amplitudes do not correlate with the other data.

The *Ulysses* measurements which *Zhang* [1997] used, were obtained during the declining phase of Solar Cycle 22. The approximate values of the tilt angles during each period shown in Figure 6.8 can be deduced from Figure 2.16, giving $\alpha \sim 40°$ for the first panel, which decreases in decrements of about 5° to the last panel. Clearly then, *Ulysses* was completely submerged in the HCS region during the period in Panel (A) and partially submerged during the period indicated by Panel (B). Inside the HCS region, the magnetic field is more irregular due to the presence of CIRs. This explains why the data points are more scattered in these two panels.

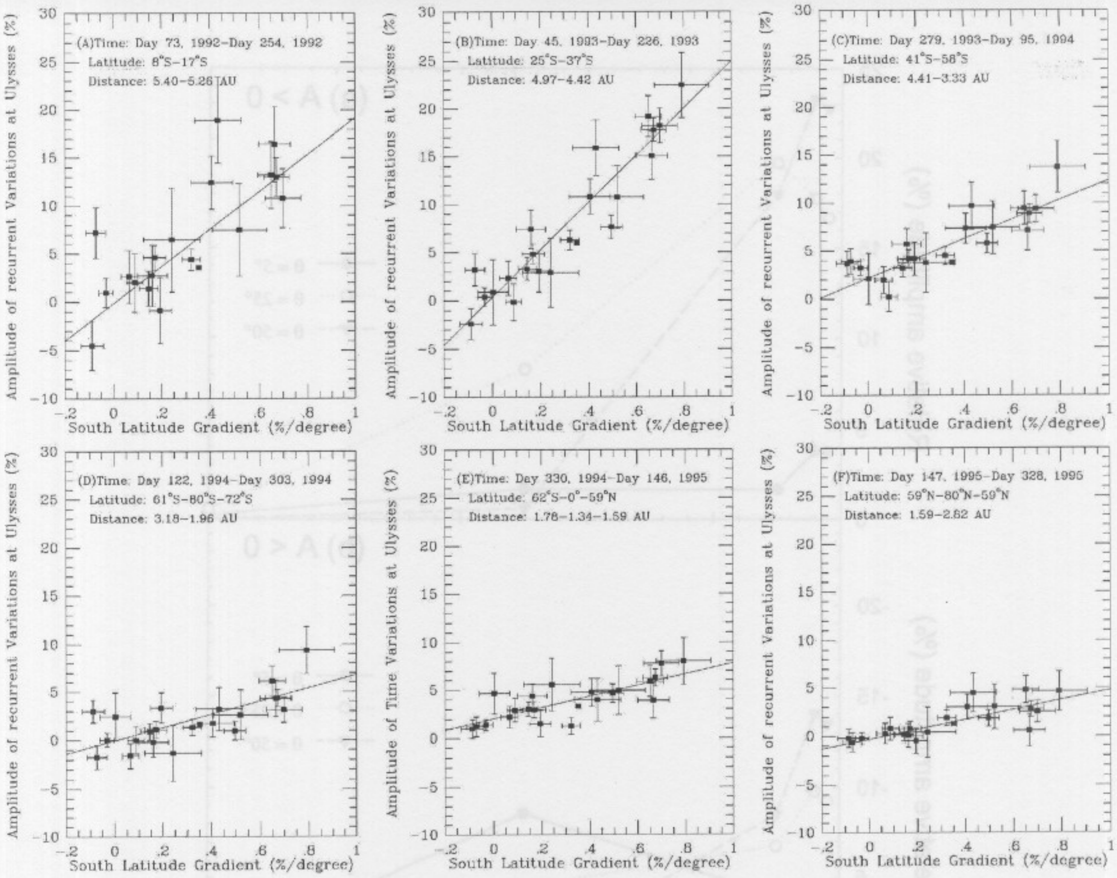

Figure 6.8: The linear relationship between the relative amplitudes of the recurrent variations and the latitudinal gradients as observed by *Ulysses* for different particles. The six panels correspond to representative locations [*Zhang*, 1997].

Nevertheless, the linear relationship is still evident.

Figure 6.8 is now reproduced for both the Parker and hybrid fields in the numerical modulation model. The results corresponding to the conditions within or closest to the ranges shown in Figure 6.8 are used for this purpose. Note that Figure 6.8 uses latitudes, whereas polar angles are used in the modulation model.

The conditions of the six panels in Figure 6.8 are simulated for the Parker field in the corresponding six panels in Figure 6.9, respectively. Evidently, the slope of a regression curve through the data points in Panels (a) and (b) decreases with G_θ, and no linear relationship exists. Since the latitude ranges of these two panels are respectively completely and mostly *inside* the HCS region, the behaviour of ΔI is mainly due to HCS effects. The large amplitude variation in Panel (b) results from the strong latitude dependence of the amplitudes in the HCS region. However, the latitude ranges of Panels (c) to (f) are mostly *outside* the HCS region (see Fig. 6.6). These panels indicate that ΔI rapidly becomes zero toward the solar poles during the $A > 0$ polarity cycle. Evidently, no linear relationship between ΔI and G_θ is obtained in the Parker field. During the $A < 0$ polarity epoch, the protons drift primarily inward along

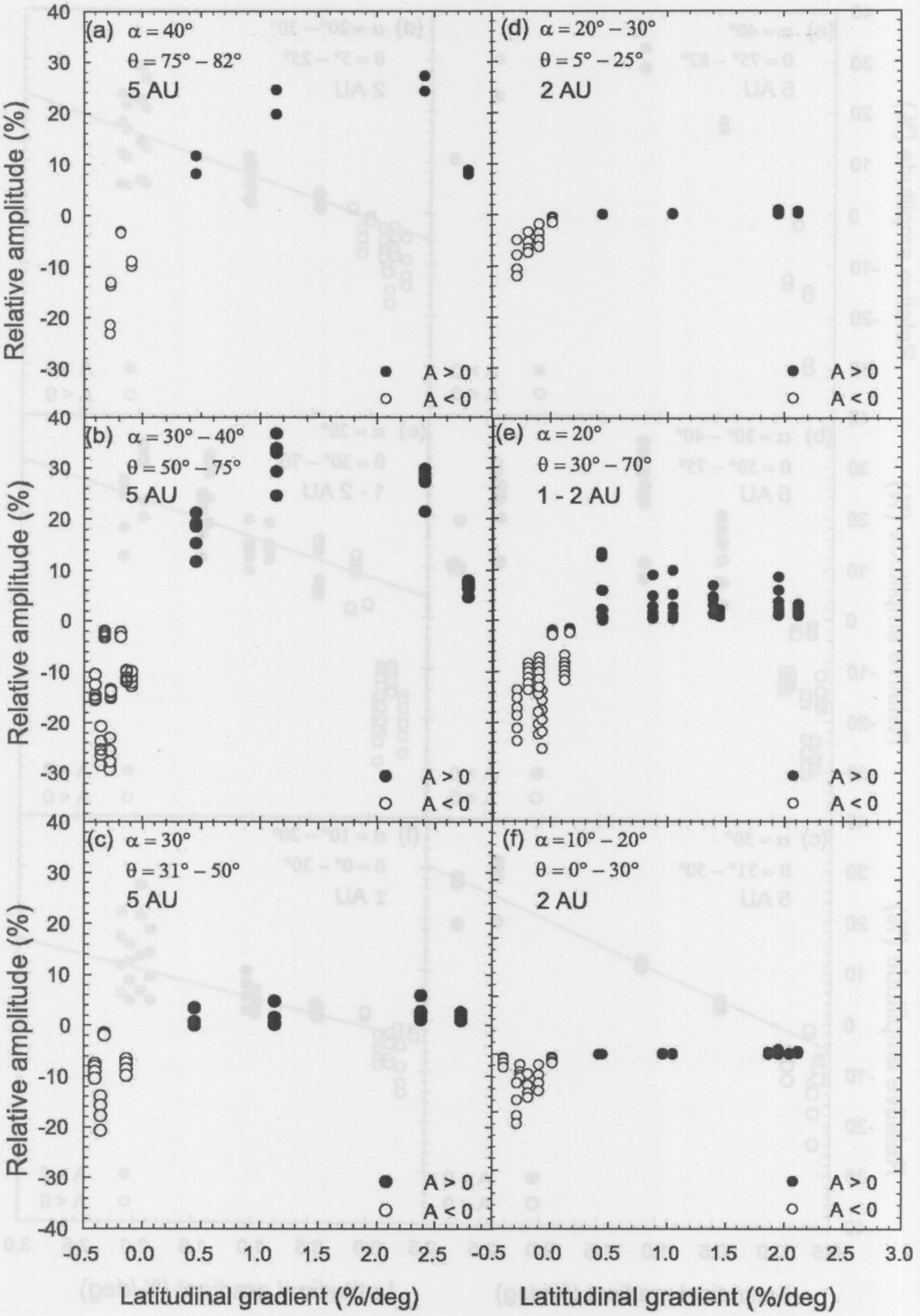

Figure 6.9: The numerical results for the proton latitudinal gradient dependence of the relative amplitudes as produced by the standard Parker field. The conditions for Panels (a) to (f) correspond to the conditions for Panels (A) to (F) in Figure 6.8, respectively. Note that polar angles are used here, whereas Figure 6.8 uses latitudes.

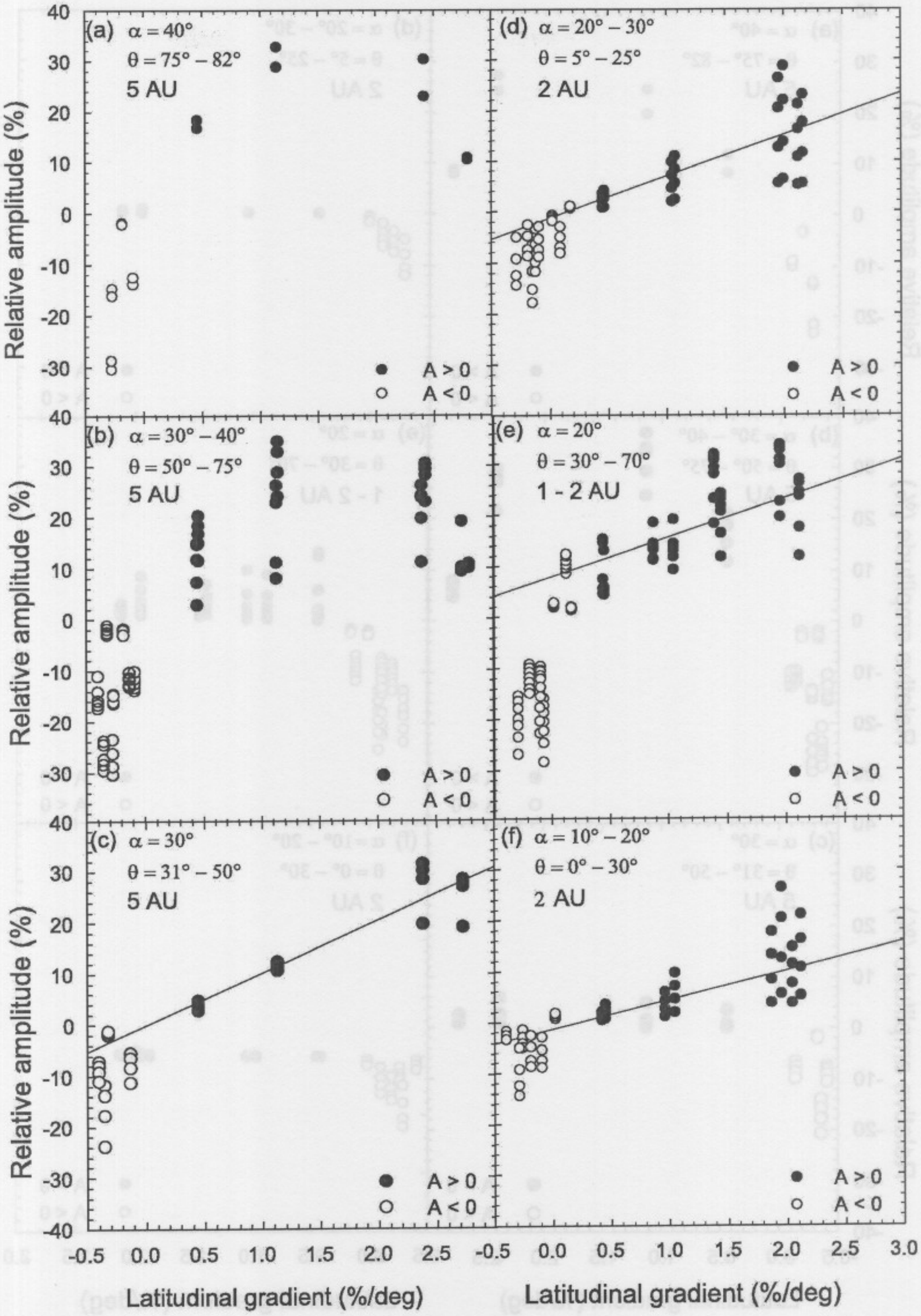

Figure 6.10: Simulation of the six panels in Figure 6.8, produced by the effect of the hybrid field on galactic protons. Panels (a) to (f) should be compared with Panels (A) to (F) of Figure 6.8, respectively. Note that all data for negative latitudinal gradients are excluded from the best fit.

the HCS and then to higher latitudes. The large amplitudes shown in Figure 6.9 are therefore produced by the HCS.

Figure 6.10 reproduces all six panels of Figure 6.8 for the Fisk-Parker hybrid HMF. The conditions for Panels (a) to (f) correspond to Panels (A) to (F) of Figure 6.8, respectively. The results in Panels (a) and (b) are qualitatively similar to the corresponding results in Figure 6.9 for the Parker field, indicating that this behaviour is caused by the presence of the HCS and not by the hybrid field. These results do not agree with Figure 6.8(A) and (B) where the linear relationship still holds, even though the protons are inside the HCS region. This suggests that a significant Fisk effect may exist inside the HCS region, as indicated by Figure 6.8, but that this effect is dominated by the effect of the HCS on the protons in the modulation code. However, note that when the data points with large latitudinal gradients in Figure 6.10(a) and (b) are neglected, the slope of a linear regression through the remaining data points is qualitatively similar to the corresponding slopes in Figure 6.8.

Since Figure 6.9 suggests that the negative latitudinal gradients are HCS effects, the corresponding data points in Panels (c) to (f) of Figure 6.10 are excluded from the linear regressions. This can be motivated by observing that Figure 6.8 contains only a few data points with negative latitudinal gradients and that these data are usually more scattered than the rest. Furthermore, *Burger and Hitge* [2004] remark that it is not certain whether the data for negative latitudinal gradients can be included. Excluding these data from the fit, the linear regressions then show that the relationship between ΔI and G_θ in Panels (c) to (f) are in good quantitative agreement with the corresponding panels of Figure 6.8. The exception is Panel (e), but note that here ΔI is positive at $G_\theta = 0$, in agreement with Figure 6.8. This result also provides a strong support for the presence of a Fisk-type field. Moreover, the maximum Fisk effect is expected near $\alpha = 30°$ at mid-latitudes (see Figs. 6.6 and 5.3). This is supported by the behaviour of the slope of the regression line, which attains a maximum in Panel (c).

6.7.3 Latitudinal Dependence of the Absolute Amplitude

Paizis et al. [1999] preferred to use the absolute amplitudes of the recurrent variations in order to avoid the problems they obtained with trend removal. Figure 6.11 [*Paizis et al.*, 1999] shows the latitudinal behaviour of the daily averaged absolute amplitudes of 0.25 – 0.2 GeV protons, as measured by *Ulysses* from 1992 to 1994. The top axis shows the corresponding time, with the first two digits denoting the year and the remaining three digits the day of the year. Also shown is the radial distance of the locations where the measurements were performed. Using again the tilt angle values of Figure 2.16, it follows that α changes from $\sim 40°$ for the first measurements to $\sim 20°$ for the last. Figure 6.11 shows a rapid increase from the equator to $\sim 25°$ and then a more gradual decrease toward the southern pole. They attribute this increase and decrease to two different causes: the increase results from the presence of CIR particles, whereas the decrease is caused by transport mechanisms such as those in the Fisk field. From

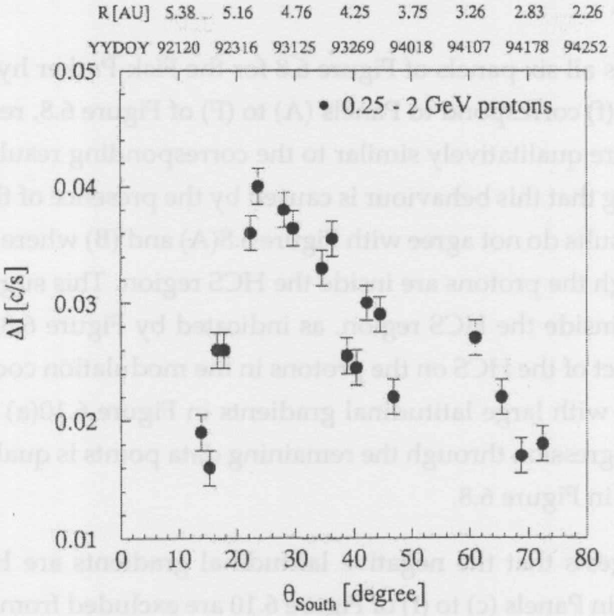

Figure 6.11: The latitude dependence of the daily averaged absolute amplitudes of the recurrent variations of 250 to 2000 MeV protons observed by *Ulysses* [*Paizis et al.*, 1999].

this figure it is unclear whether ΔI_{abs} has a local minimum between latitudes of 30° and 60°. *Paizis et al.* [1999] do not comment on this possibility.

Figures 6.12 and 6.13 clearly illustrate how Figure 6.11 may be interpreted. The effect of the HCS is evident from Figure 6.12 where a standard Parker field in the modulation code is used. The conditions used to construct Panels (a) and (b) correspond to the conditions of Figure 6.11 at high and low latitudes, respectively. This means that Panel (a) should be compared with the left-hand side of Figure 6.11 and Panel (b) with the right-hand side. For ease of comparison, the polar angle, θ, in Figure 6.12 decreases from left to right. Results for 0.2 GeV and 1 GeV protons are shown in order to indicate the effect of the proton energy. Evidently, the value of ΔI_{abs} increases significantly with both the tilt angle, α, and latitude, due to the HCS. The maximum amplitude at $\alpha \approx 40°$ is attained at $\theta \approx 65°$ and $\theta \approx 50°$ for 0.2 GeV and 1 GeV protons, respectively. This corresponds to a slightly or significantly larger latitude than where the maximum in Figure 6.11 is attained. On average, the calculated values of ΔI_{abs} are a factor of $2 - 3$ larger than the observational values.

Figure 6.13 adds the effect of the hybrid field, resulting in an extra increase and decrease in ΔI_{abs} at moderate and high latitudes (i.e. moderate and small polar angles). The combination of the two panels of Figure 6.13 agrees qualitatively with the observational results in Figure 6.11. It is therefore clear that the HCS governs the proton behaviour not only from the solar equator to a maximum latitude of $\sim 25°$ in Figure 6.11, as *Paizis et al.* [1999] interpret it, but to a lattitude of $\sim 45°$. Between 40° and 60° latitudes in Figure 6.11, the proton behaviour makes

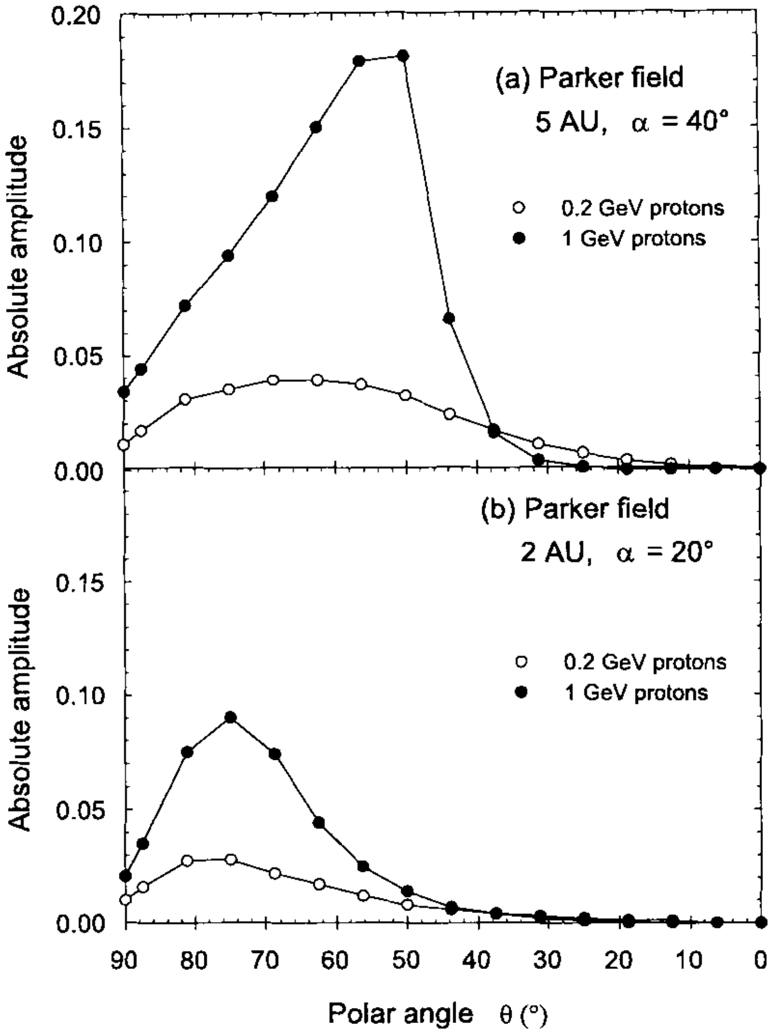

Figure 6.12: The absolute amplitudes of the recurrent variations of galactic protons as function of polar angle in a Parker field. The top panel corresponds to conditions at the left-hand side of Figure 6.11 and the bottom panel simulates the results for the right-hand side of Figure 6.11. In both panels the filled circles denote 1 GeV protons, while the open circles are the results for 0.2 GeV energies.

a transition between the effect of the HCS and the Fisk field. On average, the calculated values of ΔI_{abs} are a factor of $2-4$ larger than the observational results. This suggests that the Fisk effect in the hybrid field is possibly still an overestimation. However, a different choice for the diffusion tensor may alter this conclusion.

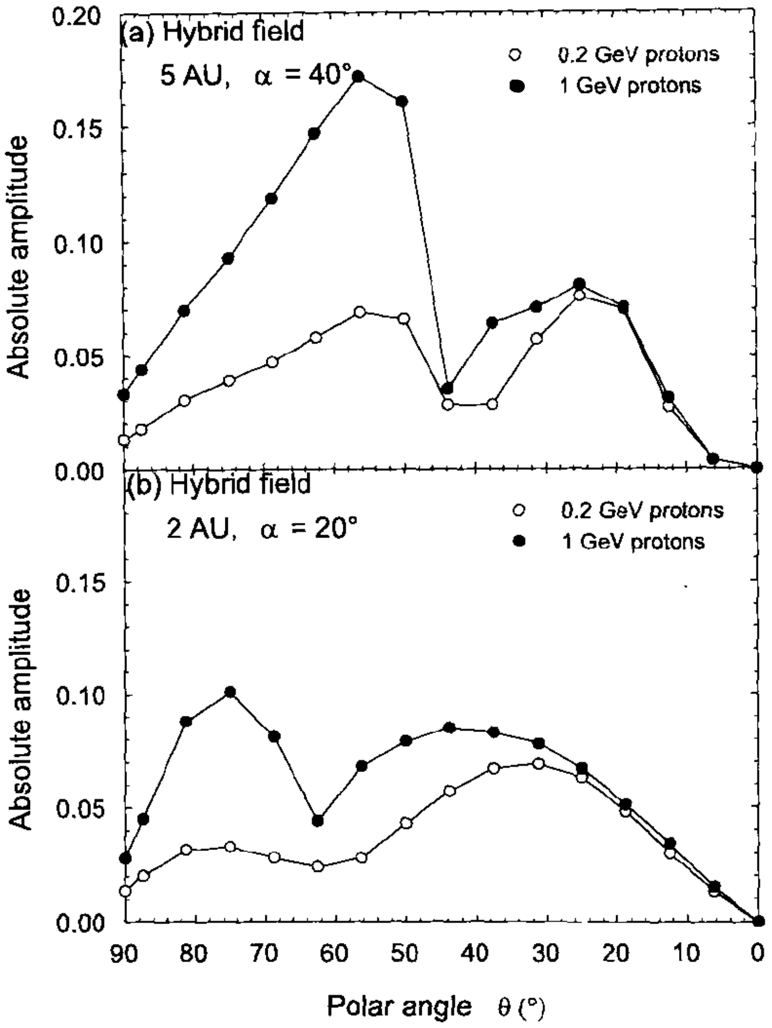

Figure 6.13: The same as Figure 6.12, but for results from the Fisk-Parker hybrid field.

6.8 Summary

In Section 5.2 it is shown that the effect of magnetic field diffusion suppresses the signature of the Fisk field. It was also found by, e.g., *Forsyth et al.* [2002] that magnetic field data did not clearly indicate the presence of a Fisk-type field. However, in this chapter it is shown that when the behaviour of protons in the inner heliosphere is simulated by means of a realistic numerical modulation code, the results agree qualitatively and sometimes almost quantitatively with observational results. This is strong evidence for the existence of a Fisk-type field in the inner heliosphere.

It is found that the global modulation of the protons in the inner heliosphere due to the presence of the hybrid field is similar to that for a pure Parker field, when energy spectra and latitudinal gradients are considered.

The linear relationship between the relative amplitudes of recurrent variations and the latitudinal gradients is in general consistent with the results from previous numerical and observational studies. However, in the model it is found that the HCS distorts the expected linear relationship in the equatorial region. This suggests that a (small) Fisk effect may be needed in this region to explain the observed linear relationship. The property that the behaviour of the protons with small or negative latitudinal gradients deviates from the linear relationship is consistent with a previous numerical study.

The Fisk-Parker hybrid model results in a maximum Fisk effect at a tilt angle of $\sim 30°$ at mid-latitudes in the innermost heliosphere. The Fisk effect is significant in the inner heliosphere during $A > 0$ polarity epochs and vanishes completely beyond ~ 50 AU in the model 100 AU heliosphere.

The hybrid field in the numerical modulation model clearly separates the effect of the HCS on the protons from the Fisk-type behaviour. There is a hint in the data that the transition from a more Fisk-like to a more Parker-like HMF is actually observed.

At this time there is no obvious reason why model results agree quite well quantitatively with calculations of the observed relative amplitude [*Zhang*, 1997], but only qualitatively with calculations of the observed absolute amplitude [*Paizis et al.*, 1999].

Chapter 7

Summary and Conclusions

The main object of this study was to test for the existence of a Fisk-type heliospheric magnetic field. Since the solar magnetic field originates in the solar interior, it was necessary to investigate all relevant physical processes from beneath the solar surface to large distances away from the sun and, especially, the magnetic field behaviour on the solar wind source surface.

It was briefly described how the solar magnetic field is generated inside the sun, probably by means of the plasma dynamo effect in the region just below the convection zone, known as the tachocline. The consequent field oscillates periodically and features above the photosphere as a dynamic network of open field lines and coronal loops.

Significant deviation from the standard Parker heliospheric magnetic field (HMF) is expected to occur over the solar poles. The traditional view of HMF models was challenged by *Fisk* [1996]. His model is the first attempt to connect the behaviour of the magnetic field at large radial distances away from the sun to processes in and above the photosphere. The Fisk field originates from the varying non-radial expansion of the magnetic field lines inside polar coronal holes, resulting from the varying magnetic location of their differentially rotating photospheric footpoints. The corresponding field line footpoints on the solar wind source surface simultaneously wind up the radially directed field lines about two axes. It was found that all three basic assumptions of the Fisk model are necessary and that only the influence of the field diffusion in and above the photosphere is debatable. When the photospheric footpoint behaviour is considered over large time and distance scales, it is found that the presence of a Fisk-type field is unavoidable during the largest fraction of the solar cycle. However, the signature of such a field is extremely difficult to identify from direct magnetic field measurements.

It was found that the strong influence of magnetic field diffusion in and above the photosphere significantly modifies the Fisk field at the solar pole and toward the polar coronal hole boundary. The presence of ragged and time-dependent boundaries adds to the random behaviour of the reconnective diffusion. The randomness of the reconnective diffusion increases with distance from the boundary on the outside of the polar coronal hole, indicating that the concept of the so-called 'return region' of the source surface footpoints fades.

The consequent latitudinal dependence of the solar magnetic field can be simulated by including a transition function in the velocity field of the Fisk HMF, which leads to a Fisk-Parker hybrid HMF, similar to the field proposed by *Burger and Hitge* [2004]. This modified field configuration may be a better representation of the actual magnetic field. The solar activity dependence of the magnetic field behaviour at the photosphere and source surface was investigated and, given some basic assumptions, the hybrid HMF model was constructed in such a way that it remains valid during the whole solar cycle. It was found that the net effect of a Fisk-type field in the heliosphere first increases with solar activity and then decreases until solar maximum.

An indirect but strong signature of a Fisk-type field in the inner heliosphere was found in the local behaviour of galactic protons. The simulated 26-day periodic cosmic-ray behaviour agrees qualitatively and at some instances almost quantitatively with the observational behaviour as shown by *Zhang* [1997] and *Paizis et al.* [1999].

The global effect of the hybrid field on cosmic rays in the inner heliosphere, compared with the standard Parker spiral, was rather insignificant. However, the observed linear relationship between the positive latitudinal gradients and the relative amplitudes of the recurrent variations was confirmed, as well as the property that the protons with small or negative latitudinal gradients deviate from this linear relationship, probably as the result of the influence of the heliospheric current sheet. A key new result is that the latitudinal dependence of the absolute amplitude of 26-day cosmic-ray variations was found to be qualitatively similar to observations reported by *Paizis et al.* [1999].

The effect of the Fisk-Parker hybrid field was found to be the largest at a tilt angle of $\sim 30^\circ$ at mid-latitudes in the innermost heliosphere during $A > 0$ polarity cycles, and to vanish completely beyond $\sim$ 50 AU. In addition, the effect of both the hybrid field and the heliospheric current sheet that were employed in the modulation model may be an overestimation and needs further investigation.

Finally, it can be concluded that, although studies of magnetic field data do not unambiguously support the existence of a Fisk-type field [see, e.g., *Forsyth et al.*, 2002], this study does.

Given the nature of the present study, it was neither meant to investigate all properties of Fisk-type fields in the heliosphere, nor to do an extensive study of the effect of such a field on cosmic-ray modulation. It is hoped that this work will stimulate further research in some of the following areas:

- The simple, zeroth-order model of the solar cycle dependence of the Fisk-Parker hybrid field was only a first attempt to construct such a model and many conditions are neglected. A more realistic model will acquire a detailed study of a large variety of time-dependent phenomena.
- Another challenge is to improve the stability of the three-dimensional code that is used,

especially over the solar poles. The current version can only handle hybrid fields that are Parker-like in the solar polar regions, and this restriction needs to be relaxed in order to use a wider range of Fisk-type fields.

- In further studies, electrons and heavier nuclei can be investigated and more attention can be given to particles with small, negative latitudinal gradients, as well as the effect of a Fisk-type field on the behaviour of particles during the negative polarity activity cycle.
- A more realistic effect of a Fisk-type field on cosmic-ray modulation can be attained by including a solar activity dependent magnetic field strength, a latitudinal dependent solar wind speed and more realistic diffusion coefficients in the modulation model.
- Finally, an interesting study will be the inclusion of a Jovian source in the modulation model. The effect of a Fisk-type field on the transport of Jovian electrons may in principle cause the electrons to be readily transported from their origin in the ecliptic region to high solar latitudes.

Acknowledgements

The heavens declare the glory of God! [Psalm 19:1, NKJV]

All praise, honour and glory belongs to the Almighty God and infinite loving Father, the Creator of the majestic heavenly bodies which we may study. May this work only magnify His Name!

The author wishes to express his gratitude to several persons and institutions:

- Prof. R. A. Burger, my supervisor, for his expert guidance, motivation and optimism throughout the whole period of study, and for keeping me on the right track between the many interesting off-spins. I greatly appreciate the sacrificial support near the end of the project.
- Dr. M. Hitge, my assistant supervisor, for letting me use her numerical modulation code and for her assistance and insight on various occasions.
- The Unit for Space Research at the Potchefstroom Campus of the North-West University for the use of their computer facilities and the opportunity to study here.
- The National Research Foundation, the South African National Antarctic Programme and the Unit for Space Research for financial support.
- The Marshall Space Flight Center for providing sunspot and other magnetic field data, the Wilcox Solar Observatory for providing tilt angle data and the NASA–Goddard Space Flight Center for providing solar wind speed data.
- Chrissie Botha for evaluating the grammar and spelling of this work.
- Family and close friends for their love and support and especially to my parents for the opportunity to obtain an education.

Psalm 8:3,4,9 [NKJV]

When I consider Your heavens, the work of Your fingers, the moon and the stars, which You have ordained, what is man that You are mindful of him, and the son of man that You visit him?

O LORD, our Lord, How excellent is Your name in all the earth!

Bibliography

Altschuler, M. D., D. E. Trotter, and F. Q. Orrall, Coronal holes, *Solar Physics, 26,* 354–365, 1972.

Babcock, H. W., The topology of the sun's magnetic field and the 22-year cycle, *Astrophys. J., 133,* 572–587, 1961.

Balogh, A., E. J. Smith, B. T. Tsurutani, D. J. Southwood, R. J. Forsyth, and T. S. Horbury, The heliospheric magnetic field over the south polar region of the sun, *Science, 268,* 1007–1010, 1995.

Balogh, A., et al., The solar origin of corotating interaction regions and their formation in the inner heliosphere, *Space Sci. Rev., 89,* 141–178, 1999.

Belenko, I. A., Coronal hole evolution during 1996-1999, *Solar Physics, 199,* 23–35, 2001.

Bieber, J. W., R. A. Burger, R. Engel, T. K. Gaisser, S. Roesler, and T. Stanev, Antiprotons at solar maximum, *Phys. Rev. Lett., 83,* 674–677, 1999.

Bilenko, I. A., Coronal holes and the solar polar field reversal, *Astron. Astrophys., 396,* 657–666, 2002.

Bilenko, I. A., Longitudinal distribution of coronal holes during 1976-2002, *Solar Physics, 221,* 261–282, 2004.

Bird, M. K., and P. Edenhofer, *Physics of the Inner Heliosphere I, edited by R. Schwenn and E. Marsch,* Springer-Verlag, Berlin, 1990.

Bravo, S., and G. Stewart, Evolution of polar coronal holes and sunspots during cycles 21 and 22, *Solar Physics, 154,* 377–384, 1994.

Burger, R. A., On the Theory and Application of Drift Motion of Charged Particles in Inhomogeneous Magnetic Fields, Ph.D. thesis, Potchefstroomse Universiteit vir Christelike Hoër Onderwys, R.S.A., 1987.

Burger, R. A., Cosmic-ray modulation and the heliospheric magnetic field, *Adv. Space Res., 35*(1), 636–642, 2005.

Burger, R. A., and M. Hattingh, Steady-state drift-dominated modulation models for galactic cosmic rays, *Astrophys. Space Sci., 230,* 375–382, 1995.

Burger, R. A., and M. Hitge, The effect of a Fisk-type heliospheric magnetic field on cosmic-ray modulation, *Astrophys. J.*, *617*(1), L73–L76, 2004.

Burger, R. A., M. S. Potgieter, and B. Heber, Rigidity dependence of cosmic ray proton latitudinal gradients measured by the Ulysses spacecraft: Implications for the diffusion tensor, *J. Geophys. Res.*, *105*(A12), 27,447–27,455, 2000.

Burlaga, L. F., K. W. Behannon, S. F. Hansen, G. W. Pneuman, and W. C. Feldman, Sources of magnetic fields in recurrent interplanetary streams, *J. Geophys. Res.*, *83*, 4177–4185, 1978.

Caballero-Lopez, R. A., H. Moraal, K. G. McCracken, and F. B. McDonald, The heliospheric magnetic field from 850 to 2000 AD inferred from ^{10}Be records, *J. Geophys. Res.*, *109*(A12102), doi:10.1029/2004JA010633, 2004.

Choudhuri, A. R., *The physics of fluids and plasmas*, 342–350 pp., Cambridge University Press, Cambridge, 1998.

Choudhuri, A. R., The current status of kinematic solar dynamo models, *J. Astrophys. and Astron.*, *21*, 373–377, 2000.

Cowsik, R., Cosmic ray sources, in *Proc. Int. Conf. Cosmic Ray 14th*, München, Germany, vol. 11, p. 3758, 1975.

Cranmer, S. R., et al., An empirical model of a polar coronal hole at solar minimum, *Astrophys. J.*, *511*(1), 481–501, 1999.

Crooker, N. U., G. L. Siscoe, S. Shodhan, D. F. Webb, J. T. Gosling, and E. J. Smith, Multiple heliospheric current sheets and coronal streamer belt dynamics, *J. Geophys. Res.*, *98*(A5), 9371–9381, 1993.

De Pontieu, B., R. J. Erdélyi, and S. P., Solar chromospheric spicules from the leakage of photospheric oscillations and flows, *Nature*, *430*, 536–539, 2004.

DeForest, C. E., J. T. Hoeksema, J. B. Gurman, B. J. Thompson, S. P. Plunkett, R. Howard, R. C. Harrison, and D. M. Hassler, Polar plume anatomy: Results of a coordinated observation, *Solar Physics*, *175*, 393–410, 1997.

Dobrzycka, D., S. R. Cranmer, A. V. Panasyuk, L. Strachan, and J. L. Kohl, Study of the latitudinal dependence of H I Lyman α and O VI emission in the solar corona: Evidence for the superradial geometry of the outflow in the polar coronal holes, *J. Geophys. Res.*, *104*(A5), 9791–9799, 1999.

Dorotovic, I., Area of polar coronal holes and sunspot activity: years 1939-1993, *Solar Physics*, *167*, 419–426, 1996.

Dryer, M., *Solar wind and heliosphere, in The Solar wind and the Earth, edited by S.-I. Akasofu and Y. Kamide*, 21-35 pp., Terra Scientific Publishing Company, Tokyo, 1987.

Erdös, G., and A. Balogh, *In situ* observations of magnetic field fluctuations, *Adv. Space Res.*, *35*(4), 625–635, 2005.

Feldman, U., K. G. Widing, and H. P. Warren, Morphology of the quiet solar upper atmosphere in the $4 \times 10^4 < t_e < 1.4 \times 10^6$ K temperature regime, *Astrophys. J.*, *522*(2), 1133–1147, 1999.

Ferreira, S. E. S., The Heliospheric Transport of Galactic Cosmic Rays and Jovian Electrons, Ph.D. thesis, Potchefstroomse Universiteit vir Christelike Hoër Onderwys, R.S.A., 2002.

Fisk, L. A., Motion of the footpoints of heliospheric magnetic field lines at the Sun: Implications for recurrent energetic particle events at high heliographic latitudes, *J. Geophys. Res.*, *101*, 15,547–15,553, 1996.

Fisk, L. A., The open magnetic flux of the sun. I. Transport by reconnections with coronal loops, *Astrophys. J.*, *626*(1), 563–573, 2005.

Fisk, L. A., and N. A. Schwadron, The behavior of the open magnetic field of the sun, *Astrophys. J. Lett.*, *560*(2), L425–L438, 2001.

Fisk, L. A., T. H. Zurbuchen, and N. A. Schwadron, On the coronal magnetic field: consequences of large-scale motions, *Astrophys. J.*, *521*(2), 868–877, 1999a.

Fisk, L. A., N. A. Schwadron, and T. H. Zurbuchen, Acceleration of the fast solar wind by the emergence of new magnetic flux, *J. Geophys. Res.*, *104*(A9), 19,765–19,772, 1999b.

Fisk, L. A., T. H. Zurbuchen, and N. A. Schwadron, Coronal hole boundaries and their interaction with adjacent regions, *Space Sci. Rev.*, *87*, 43–54, 1999c.

Forsyth, R. J., A. Balogh, E. J. Smith, N. Murphy, and D. J. McComas, The underlying magnetic field direction in Ulysses observations of the southern polar heliosphere, *Geophys. Res. Lett.*, *22*(23), 3321–3324, 1995.

Forsyth, R. J., A. Balogh, E. J. Smith, G. Erdös, and D. J. McComas, The underlying Parker spiral structure in the Ulysses magnetic field observations, 1990-1994, *J. Geophys. Res.*, *101*(A1), 395–404, 1996.

Forsyth, R. J., A. Balogh, and E. J. Smith, The underlying direction of the heliospheric magnetic field through the Ulysses first orbit, *J. Geophys. Res.*, *107*(A11), dOI:10.1029/2001JA005056, 2002.

Fox, P., P. McIntosh, and P. R. Wilson, Coronal holes and the polar field reversals, *Solar Physics*, *177*, 375–393, 1999.

Gary, G. A., Plasma beta above a solar active region: Rethinking the paradigm, *Solar Physics*, *203*, 71–86, 2001.

Gazis, P. R., A. Barnes, J. D. Mihalov, and A. J. Lazarus, Solar wind velocity and temperature in the outer heliosphere, *J. Geophys. Res.*, *99*(A4), 6561–6573, 1994.

Giacalone, J., Particle transport and acceleration at corotating interaction regions, *Adv. Space Res.*, *23*(3), 581–590, 1999.

Giacalone, J., The latitudinal transport of energetic particles associated with corotating interaction regions, *J. Geophys. Res.*, *106*(A8), 15,881–15,888, 2001.

Giacalone, J., and J. R. Jokipii, The transport of cosmic rays across a turbulent magnetic field, *Astrophys. J.*, *520*(1), 204–214, 1999.

Giacalone, J., and J. R. Jokipii, Magnetic footpoint diffusion at the sun and its relation to the heliospheric magnetic field, *Astrophys. J.*, *616*(2), 573–577, 2004.

Gizon, L., T. L. Duvall, and J. Schou, Wave-like properties of solar supergranulation, *Nature*, *421*, 43–33, 2003.

Goldstein, B. E., M. Neugebauer, J. T. Gosling, S. J. Bame, J. L. Phillips, D. J. McComas, and A. Balogh, ULYSSES observations of solar wind plasma parameters in the ecliptic from 1.4 to 5.4 AU and out of the ecliptic, *Space Sci. Rev.*, *72*, 113–116, 1995.

Gombosi, T. I., *Physics of the Space Environment*, 211–254 pp., Cambridge University Press, Cambridge, 1998.

Gosling, J. T., and V. J. Pizzo, Formation and evolution of corotating interaction regions and their three dimensional structure, *Space Sci. Rev.*, *89*, 21–52, 1999.

Gosling, J. T., S. J. Bame, W. C. Feldman, D. J. McComas, P. Riley, B. E. Goldstein, and M. Neugebauer, The northern edge of the band of solar wind variability: Ulysses at $\sim$ 4.5 AU, *Geophys. Res. Lett.*, *24*(3), 309–312, 1997.

Gosling, J. T., et al., The band of solar wind variability at low heliographic latitudes near solar activity minimum: Plasma results from the Ulysses rapid latitude scan, *Geophys. Res. Lett.*, *22*(23), 3329–3332, 1995.

Gurnett, D., and N. Dangelo, The 22-year solar cycle – A heliospheric oscillation, *Planet. Space Sci.*, *30*, 307–312, 1982.

Hale, G. E., On the probable existence of a magnetic field in sun-spots, *Astrophys. J.*, *28*, 315, 1908.

Hale, G. E., F. Ellerman, S. B. Nicholson, and A. H. Joy, The magnetic polarity of sun-spots, *Astrophys. J.*, *49*, 153, 1919.

Handy, . N., and . J. Schrijver, On the evolution of the solar photospheric and coronal magnetic field, *Astrophys. J.*, *547*(2), 1100–1108, 2001.

Harra, L. K., and L. K. Mason, *Space Science*, 197, 292 pp., Imperial College Press, London, 2004.

Harvey, K. L., Large scale patterns of magnetic activity and the solar cycle, in *Amer. Astron. Soc., 188th Meeting*, vol. 28, p. 867, 1996.

Harvey, K. L., and F. Recely, Polar coronal holes during cycles 22 and 23, *Solar Physics*, *211*, 31–52, 2002.

Hattingh, M., Dryf van Kosmiese Strale by 'n Golwende Neutrale Vlak in die Heliosfeer, Master's thesis, Potchefstroomse Universiteit vir Christelike Hoër Onderwys, R.S.A., 1993.

Hattingh, M., The Modulation of Galactic Cosmic Rays in a Three-Dimensional Heliosphere, Ph.D. thesis, Potchefstroomse Universiteit vir Christelike Hoër Onderwys, R.S.A., 1998.

Hattingh, M., and R. A. Burger, A new simulated wavy neutral sheet drift model, *Adv. Space Res.*, *16*(9), 213–216, 1995.

Hoeksema, J. T., The large-scale structure of the heliospheric current sheet during the ulysses epoch, *Space Sci. Rev.*, *72*, 137–148, 1995.

Hoeksema, J. T., X. P. Zhao, and P. H. Scherrer, Predictions of coronal and interplanetary magnetic fields: The promise of SOI-MDI on SOHO, in *AIP Conf. Proc., 8th Intern. Sol. Wind Conf.*, vol. 382, pp. 76–79, 1996.

Horbury, T., J. Kóta, and E. C. Roelof, *Difference between heliospheric magnetic field models, in Cosmic rays in the heliosphere, edited by L. A. Fisk, J. R. Jokipii, G. M. Simnett, R. von Steiger and K.-P. Wentzel*, 221–225 pp., Kluwer Academic Publishers, Dordtrecht, 1998.

Hu, Y. Q., S. R. Habbal, Y. Chen, and X. Li, Are coronal holes the only source of fast solar wind at solar minimum?, *J. Geophys. Res.*, *108*(A101377), doi:10.1029/2002JA009776, 2003.

Hudson, H. S., Coronal holes as seen in soft X-rays by Yohkoh, in *Proc. SOHO Symposium*, Davos, Switzerland, 2002, vol. 11, pp. 341–349, 2002.

Jokipii, J. R., The physics of cosmic-ray modulation, *Adv. Space Res.*, *9*, 105–119, 1989.

Jokipii, J. R., and J. Kóta, The polar heliospheric magnetic field, *Geophys. Res. Lett.*, *16*, 1–4, 1989.

Jokipii, J. R., and J. Kóta, Three-dimensional cosmic-ray simulations: heliographic latitude and current-sheet tilt, *Space Sci. Rev.*, *72*, 379–384, 1995.

Jokipii, J. R., and B. Thomas, Effects of drift on the transport of cosmic rays. IV - Modulation by a wavy interplanetary current sheet, *Astrophys. J.*, *243*(1), 1115–1122, 1981.

Kivelson, M. G., and C. T. Russel, *Introduction to Space Physics, second edition*, 5–6 pp., Cambridge University Press, Cambridge, 1996.

Kobylinski, Z., Comparison of the Fisk magnetic field with the standard Parker IMF: Consequences for diffusion coefficients, *Adv. Space Res.*, *27*(3), 541–546, 2001.

Kopp, R. A., and T. E. Holzer, Dynamics of coronal hole regions. I – Steady polytropic flows with multiple critical points, *Solar Physics*, *49*, 43–56, 1976.

Kosovichev, A., *Helioseismic observations of plasma motions in the solar convection zone, in Turbulence, waves and instabilities in solar plasma, edited by R. Erdélyi et al.*, 57-63 pp., Kluwer Academic Publishers, Dordrecht, 2003.

Kóta, J., and J. R. Jokipii, Effects of drift on the transport of cosmic rays. VI - A three-dimensional model including diffusion, *Astrophys. J.*, *265*(1), 73–581, 1983.

Kóta, J., and J. R. Jokipii, Corotating variations of cosmic rays near the south heliospheric pole, *Science*, *268*, 1024–1025, 1995.

Kóta, J., and J. R. Jokipii, 3-D modeling of cosmic-ray transport in the heliosphere: toward solar maximum, *Adv. Space Res.*, *27*(3), 529–534, 2001a.

Kóta, J., and J. R. Jokipii, Cosmic ray transport in a heliospheric magnetic field with non-polar coronal holes, *Space Sci. Rev.*, *98*, 327–330, 2001b.

Langner, U. W., Effects of termination shock acceleration on cosmic rays in the heliosphere, Ph.D. thesis, Potchefstroomse Universiteit vir Christelike Hoër Onderwys, R.S.A., 2004.

Layzer, D., R. Rosner, and H. T. Doyle, On the origin of solar magnetic fields, *Astrophys. J.*, *229*(1), 1126–1137, 1979.

Leighton, R. B., Transport of magnetic fields on the sun, *Astrophys. J.*, *140*, 1547, 1964.

Leighton, R. B., A magneto-kinematic model of the solar cycle, *Astrophys. J.*, *156*, 1–26, 1969.

Maunder, E. W., Note on the distribution of sun-spots in heliographic latitude, 1874-1902, *Mon. Not. Roy. Astron. Soc.*, *64*, 747, 1904.

McComas, D. J., et al., Understanding the evolution of the sun's open magnetic flux, *Geophys. Res. Lett.*, *25*(1), 1–4, 1998.

McKibben, R. B., J. J. Connell, C. Lopate, J. A. Simpson, and M. Zhang, Observations of galactic cosmic rays and the anomalous helium during ULYSSES passage from the south to the north solar pole, *Astron. Astrophys.*, *316*, 547–554, 1996.

Moraal, H., Proton modulation near solar minimim periods in consecutive solar cycles, in *Proc. Int. Conf. Cosmic Ray 21th*, Adelaide, vol. 6, pp. 140–143, 1990.

Moraal, H., R. Muscheler, L. du Plessis, J. Beer, K. G. McCracken, and F. B. McDonald, ^{10}Be concentration in the ice shelf of Queen Maud Land, Antarctica, *South African Journal of Science*, *101*, 299–301, 2005.

Munro, R. H., and B. V. Jackson, Physical properties of a polar coronal hole from 2 to 5 $R_\odot$, *Astrophys. J.*, *213*(3), 874–886, 1977.

Murphy, N., E. J. Smith, and N. A. Schwadron, Strongly underwound magnetic fields in co-rotating rarefaction regions: Observations and implications, *Geophys. Res. Lett.*, *29*(22), 23–1–23–4, 2002.

Ness, N. F., and L. F. Burlaga, Spacecraft studies of the interplanetary magnetic field, *Astrophys. J.*, *106*(A8), 15,803–15,817, 2001.

Newkirk, G., Structure of the solar corona, *Astron. Astrophys.*, *5*, 213–266, 1967.

Nolte, J. T., A. S. Krieger, A. F. Timothy, R. E. Gold, E. C. Roelof, G. Vaiana, A. J. Lazarus, J. D. Sullivan, and P. S. McIntosh, Coronal holes as sources of solar wind, *Solar Physics*, *46*, 303–322, 1976.

Paizis, ., et al., Amplitude evolution and rigidity dependence of the 26-day recurrent cosmic ray decreases: COSPIN/KET results, *J. Geophys. Res.*, *104*(A12), 28,241–28,247, 1999.

Parhi, S., J. W. Bieber, W. H. Matthaeus, R. A. Burger, and J. Minnie, Self consistent modeling of turbulence transport with implications for cosmic ray transport and modulation, in *Eos Trans. AGU*, *84*(46), Fall Meet. Suppl., Abstract SH11C-13, 2003.

Parker, E. N., The formation of sunspots from the solar toroidal field, *Astrophys. J.*, *121*, 491–507, 1955a.

Parker, E. N., Hydromagnetic dynamo models, *Astrophys. J.*, *122*, 293–314, 1955b.

Parker, E. N., Dynamics of the interplanetary gas and magnetic fields, *Astrophys. J.*, *128*, 664–676, 1958.

Pneuman, G. W., and R. A. Kopp, Gas-magnetic field interactions, *Solar Physics*, *18*, 258–270, 1969.

Roelof, E. C., G. M. Simnett, R. B. Decker, L. J. Lanzerotti, C. G. Maclennan, T. P. Armstrong, and R. E. Gold, Reappearance of recurrent low-energy particle events at Ulysses/HI-SCALE in the northern hemisphere, *J. Geophys. Res.*, *102*(A6), 11,251–11,262, 1997.

Rust, D., Measurements of the magnetic fields in quiescent solar prominences, Ph.D. thesis, University of Colorado at Boulder, 1966.

Scharmer, G. B., B. V. Gudiksen, D. Kiselman, M. G. Löfdahl, and L. H. M. Rouppe van der Voort, Dark cores in sunspot penumbral filaments, *Nature*, *420*, 151–153, 2002.

Schatten, K. H., Current sheet magnetic model for the solar corona, *Cosmic Electrodyn.*, *2*, 232–245, 1971.

Schatten, K. H., Coronal and interplanetary magnetic field geometry: Streak lines, *J. Geophys. Res.*, *106*(A8), 15,833–15,840, 2001.

Schatten, K. H., J. M. Wilcox, and N. F. Ness, A model of interplanetary and coronal magnetic fields, *Solar Physics*, *6*, 442–455, 1969.

Schou, ., et al., Helioseismic studies of differential rotation in the solar envelope by the solar oscillations investigation using the Michelson Doppler Imager, *Astrophys. J.*, *505*(1), 390–417, 1998.

Schrijver, C. J., A. M. Title, K. L. Harvey, N. R. Sheeley, Y. M. Wang, G. H. J. van den Oord, R. A. D. Shine, T. Tarbell, and N. E. Hurlburt, Large-scale coronal heating by the small-scale magnetic field of the sun, *Nature, 394*, 152, 1998.

Schwadron, N. A., An explanation for strongly underwound magnetic field in co-rotating rarefaction regions and its relationship to footpoint motion on the the sun, *Geophys. Res. Lett., 29*(8), 8–1–8–4, 2002.

Schwadron, N. A., L. A. Fisk, and T. H. Zurbuchen, Elemental fractionation in the slow solar wind, *Astrophys. J., 521*(2), 859–867, 1999.

Simpson, J. A., *Cosmic radiation: Particle astrophysics in the heliosphere, in* Frontiers in cosmic physics: Symposium in memory of Serge Korff, *edited by R. B. Mendell and A. J. Mincer*, 97 pp., New York Academy of Sciences, New York, 1992.

Simpson, J. A., M. Zhang, and S. Bame, A solar polar north-south asymmetry for cosmic-ray propagation in the heliosphere: The ULYSSES pole-to-pole rapid transit, *Astrophys. J. Lett., 465*, L69–L72, 1996.

Simpson, J. A., et al., Cosmic ray and solar particle investigations over the south polar regions of the sun, *Science, 268*, 1019–1029, 1995.

Smith, C. W., and J. W. Bieber, Solar cycle variation of the interplanetary magnetic field spiral, *Astrophys. J., 370*(1), 435–441, 1991.

Smith, E., The heliospheric current sheet, *J. Geophys. Res., 106*(A8), 15,819–15,832, 2001.

Smith, E. J., The sun, solar wind, and magnetic field. I, in *Course CXLII*, edited by A. Ferrari and E. Sindoni, in *Proc. Int. Sch. of Phys. "Enrico Fermi"*, Amsterdam, The Netherlands, 2000.

Smith, E. J., M. Neugebauer, A. Balogh, S. J. Bame, R. P. Lepping, and B. T. Tsurutani, ULYSSES observations of latitude gradients in the heliospheric magnetic field: Radial component and variances, *Space Sci. Rev., 72*, 167–170, 1995.

Smith, E. J., et al., The sun and heliosphere at solar maximum, *Science, 302*, 1165–1169, 2003.

Snodgrass, H. B., Magnetic rotation of the solar photosphere, *Astrophys. J., 270*(1), 288–299, 1983.

Stone, E. C., A. C. Cummings, F. B. McDonald, B. C. Heikkila, N. Lal, and W. R. Webber, Voyager 1 explores the termination shock region and the heliosheath beyond, *Science, 309*, 2017–2020, 2005.

Suess, S. T., G. A. Gary, and S. F. Nerney, Beta in streamers, in *AIP Conf. Proc., Intern. Sol. Wind Conf.*, vol. 471, 1996.

Suess, S. T., G. Poletto, A.-H. Wang, S. T. Wu, and I. Cuseri, The geometric spreading of coronal plumes and coronal holes, *Solar Physics, 180*, 231–246, 1998.

Van Niekerk, Y., An investigation into the causes and consequences of north-south asymmetries in the heliosphere, Master's thesis, Potchefstroomse Universiteit vir Christelike Hoër Onderwys, R.S.A., 2000.

Waldmeier, M., Cyclic variations of the polar coronal hole, *Solar Physics*, *70*, 251–258, 1981.

Wang, Y.-M., and N. R. Sheeley, Solar wind speed and coronal flux-tube expansion, *Astrophys. J.*, *355*(1), 726–732, 1990.

Wang, Y.-M., and N. R. Sheeley, On potential field models of the solar corona, *Astrophys. J.*, *392*(1), 310–319, 1992.

Wang, Y.-M., and N. R. Sheeley, Understanding the rotation of coronal holes, *Astrophys. J.*, *414*(2), 916–927, 1993.

Wang, Y.-M., and N. R. Sheeley, Modeling the sun's large-scale magnetic field during the Maunder Minimum, *Astrophys. J.*, *591*(2), 1248–1256, 2003.

Wang, Y.-M., A. G. Nash, and N. R. Sheeley, Magnetic flux transport on the sun, *Science*, *245*, 712–718, 1989.

Wang, Y.-M., J. Sheeley, N. R., and A. G. Nash, A new solar cycle model including meridional circulation, *Astrophys. J.*, *383*(1), 431–442, 1991.

Wang, Y.-M., N. R. Sheeley, and J. Lean, Understanding the evolution of the sun's open magnetic flux, *Geophys. Res. Lett.*, *27*(5), 621, 2000.

Webb, D. F., J. M. Davis, and P. S. McIntosh, Observations of the reappearance of polar coronal holes and the reversal of the polar magnetic field, *Solar Physics*, *92*, 109–132, 1984.

Whang, Y. C., L. F. Burlaga, Y.-M. Wang, and N. R. Sheeley, Solar wind speed and temperature outside 10 AU and the termination shock, *Astrophys. J.*, *589*(1), 635–643, 2003.

Wiegelmann, T., and S. K. Solanki, Why are coronal holes indistinguishable from the quiet sun in transition region radiation?, in *Proc. SOHO Symposium*, St. Andrews, Scotland, 2004, vol. 15, p. 35, 2004.

Zhang, M., A linear relationship between the latitude gradient and 26 day recurrent variation in the fluxes of galactic cosmic rays and anomalous nuclear components. I. Observations, *Astrophys. J.*, *488*(2), 841–853, 1997.

Zhao, X. P., J. T. Hoeksema, and P. H. Scherrer, Changes in the boot-shaped coronal hole boundary during Whole Sun Month near sunspot minimum, *J. Geophys. Res.*, *104*(A5), 9735–9751, 1999.

Zhou, X., E. J. Smith, D. Winterhalter, D. J. McComas, R. M. Skoug, B. E. Goldstein, and C. W. Smith, Thickness of heliospheric current and plasma sheets: Dependence on distance, in *Eos Trans. AGU, Spring Meet. Suppl., Abstract SH41A-01*, 2005.

Zurbuchen, T. H., N. A. Schwadron, and L. A. Fisk, Direct observational evidence for a heliospheric magnetic field with large excursions in latitude, *J. Geophys. Res.*, *102*(A11), 24,175–24,181, 1997.